

TR33375

STELLINGEN

behorende bij het proefschrift

Longshore current dynamics

van

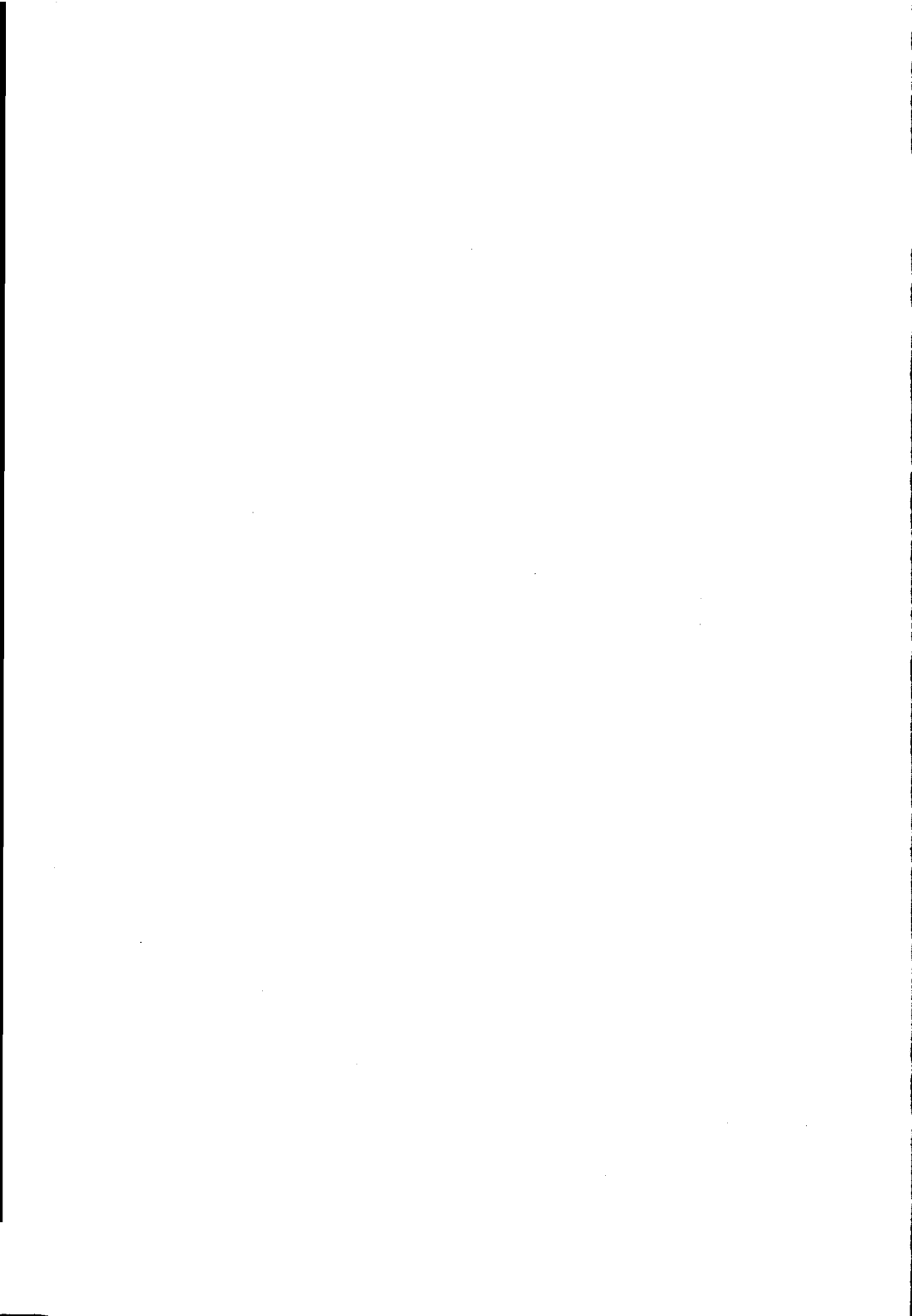
Ad Reniers

Delft, 21 mei 1999

1. In afwezigheid van een drukgradiënt in kustlangsrichting bevindt de maximale langstroomsnelheid van de brandingsstroom zich in de directe nabijheid van de locaties waar golfenergie-dissipatie het sterkst is, d.w.z. nabij de top van de bank en/of de waterlijn.
2. De positie van het snelheidsmaximum van de brandingsstroom, zoals waargenomen tijdens de DELILAH meet-campagne, is het resultaat van een door bodemvariaties geïnduceerde drukgradiënt in kustlangsrichting.
3. Hoewel instabiliteiten in de golfgedreven langstroom en randgolven zich in hetzelfde frequentiebereik kunnen bevinden stelt een laboratoriumonderzoek naar randgolven veel hogere eisen aan de te gebruiken fysische faciliteit.
4. Indien het bassin dat in het onderzoek voor dit proefschrift is gebruikt 5 meter langer was geweest had het langstroomsnelheidsprofiel in de nabijheid van de uitstroomopening er beduidend anders uitgezien.
5. De voortschrijdende complexiteit van morfodynamische modellen zal er toe leiden dat het gebruik van deze modellen voor de gemiddelde gebruiker als een black box benadering werkt.
6. De huidige inspanningen met betrekking tot de beschrijving van kwaliteit van processen en functioneren in het kader van ISO9001 en BTO zullen niet tot de gewenste verbeteringen leiden.

7. Het toepassen van relatief eenvoudige modellen in complexe situaties leidt vaak tot meer inzicht dan het gebruik van de daartoe geëigende complexe modellen.
8. Het gebruik van een spectraal golfmodel in combinatie met HF-radar voor het meten van richtingsspreidingsspectra maakt het gebruik van een (dure) tweede HF-radar opstelling overbodig (De Valk e.a., 1999).

De Valk, C., A. Reniers, J. Atanga, A. Vizinho and J. Vogelzang, 1999: Monitoring surface waves in coastal waters by integrating HF radar measurement and modelling. To appear in J. Coastal Eng.
9. De combinatie van numeriek, laboratorium en veldonderzoek is essentieel voor het verkrijgen van inzicht in de fysische processen beschreven in dit proefschrift.
10. De verificatie van complexe numerieke modellen stelt eisen waar de huidige meetmethodieken en bijbehorende analyses steeds vaker niet aan (kunnen) voldoen.
11. Hoewel de grenzen tussen netwerken en vriendjespolitiek vaag zijn, zijn de mogelijke consequenties duidelijk anders, zoals proefondervindelijk vastgesteld door voormalig EU-commissaris Cresson.
12. Kleren maken de man niet tot wat hij is, noch tot wat hij kan.



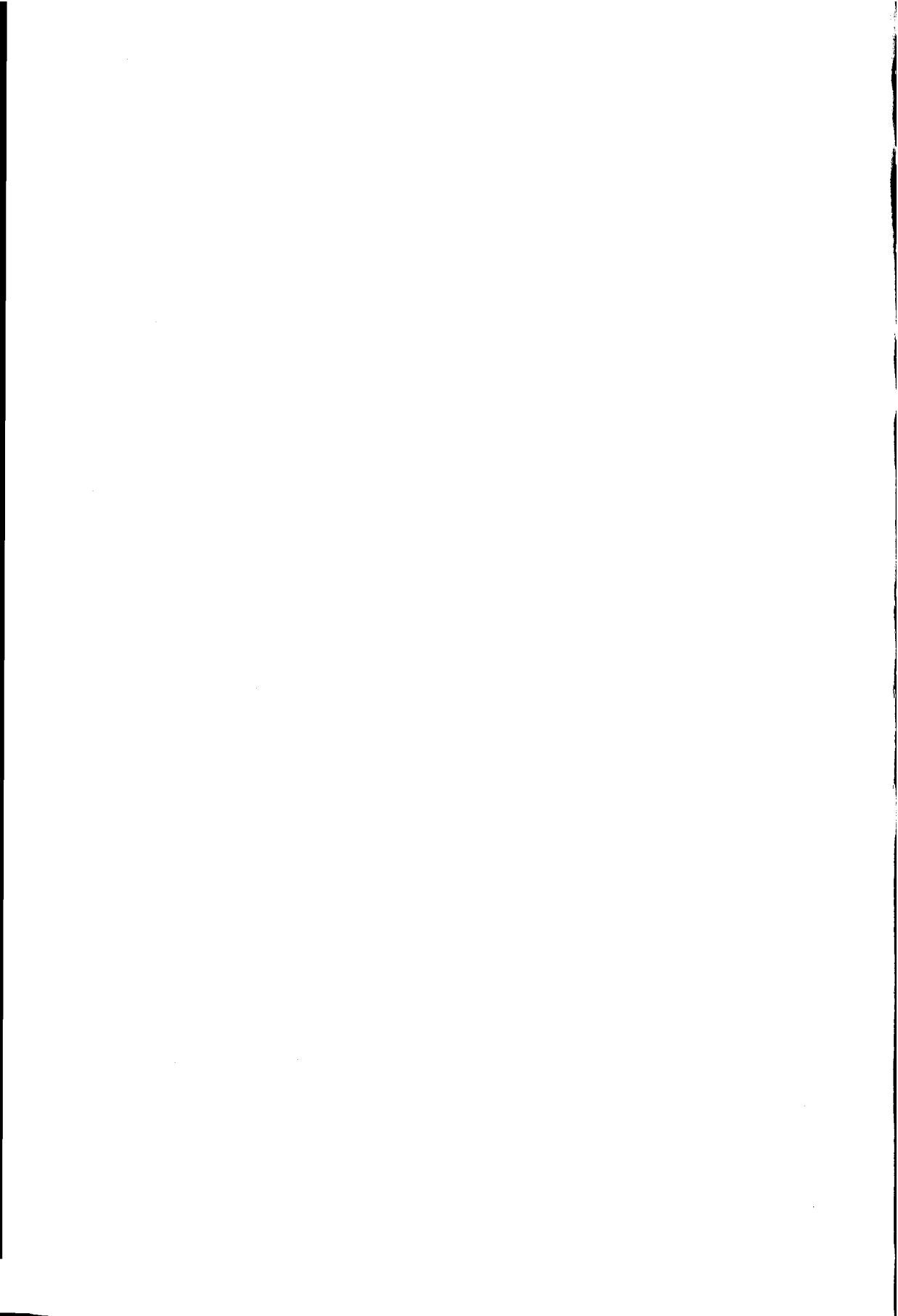
72/117 3337

3039112

TR 3337

**Longshore current dynamics**

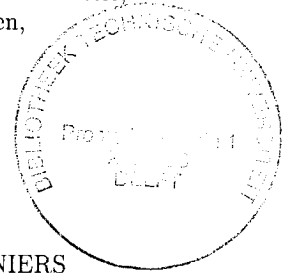
*Dynamica van golfgedreven langsstromen*



# Longshore current dynamics

PROEFSCHRIFT

ter verkrijging van de graad van doctor  
aan de Technische Universiteit Delft,  
op gezag van de Rector Magnificus prof.ir. K.F. Wakker,  
in het openbaar te verdedigen ten overstaan van een commissie,  
door het College voor Promoties aangewezen,  
op vrijdag 21 mei 1999 te 10.30 uur



door Adrianus Johannes Hermanus Maria RENIERS  
civiel ingenieur  
geboren te Rucphen

Dit proefschrift is goedgekeurd door de promotor:

Prof.dr.ir. J.A. Battjes

Samenstelling promotiecommissie:

Rector Magnificus	, voorzitter
Prof.dr.ir. J.A. Battjes	, Technische Universiteit Delft, promotor
Prof.dr. A. Falqués	, Universitat Politecnica Catalunya (Spanje)
Prof.dr. D.A. Huntley	, University of Plymouth (Groot Britannië)
Prof.dr.ir. M.J.F. Stive	, Technische Universiteit Delft
Prof.dr.ir. H.J. de Vriend	, Technische Universiteit Delft
Dr.ir. J.A. Roelvink	, WL Delft Hydraulics
Dr. H.E. de Swart	, Universiteit Utrecht

This thesis has benefitted from substantial support from various institutes: The European Community within the framework of the Large Installations Plan (LIP), project 19 M to perform the laboratory experiments in the large multidirectional wave flume at WL | Delft Hydraulics. The J.M. Burgers Centre for the analysis of the laboratory experiments. The Naval Postgraduate School (NPS) for participating in the field experiments at Duck in 1994 and a seven months visit in 1995. The National Institute for Coastal and Marine Management (RIKZ) through the Netherlands Centre for Coastal Research (NCK) for additional analysis and dissemination. The European Community through the project on Surf and Swash Zone Mechanics (SASME) under contract no. MAS3-CT97-0081.

Front cover: Beach dynamics  
photos by Stella Harm en Ad Reniers

Copyright © 1999 by Ad Reniers  
Reproduced by PrintPartners Ipskamp B.V., from camera-ready copy supplied by the author.

ISBN 90-9012742-9

This thesis is also published in the series 'Communications on Hydraulic and Geotechnical Engineering' of the Faculty of Civil Engineering and Geosciences as Report No. 99-2, ISSN 0169-6548.





*At the beach*

*Waves coming in at Stille Strand where  
Stella stares expectantly at the horizon*



## **Abstract**

Laboratory experiments have been performed to examine the shear instability of longshore currents. Minimizing the recirculation resulted in minimal alongshore set-up gradients, indicating that the measured current velocity profiles corresponded to purely wave-driven currents only.

Based on the experiments we conclude that, for purely wave-driven longshore currents, the maximum longshore current velocities occur where breaking is most intense, i.e. on the bar and near the shoreline. Lateral mixing smoothes the current profile, but does not significantly affect the position of the maximum current velocity, which in the case of a barred beach clearly remains near the crest. This holds for the cases of short waves, long waves and random waves on barred beaches.

Next we have used the mean wave-and flow data for verification and validation of a numerical model for uniform alongshore conditions using existing model equations. Comparison of computational results with measurements showed good agreement for wave transformation, set-up and longshore current velocity profiles. Lateral mixing was required to obtain a good match with the data, also in the case of random waves on a barred beach. The transition effect, caused by the surface roller, was essential in the correct prediction of the location of maximum wave forcing and improved the correspondence with the measured longshore current velocity in the trough.

The thus verified numerical longshore current model has been extended with an additional forcing of the longshore current due to the presence of a steady alongshore pressure gradient. Next the model was applied to examine longshore current measurement data obtained during the DELILAH field experiment. The analysis showed that bathymetry induced alongshore pressure gradients were present during DELILAH experiment. A relatively small alongshore pressure gradient over the trough, acting in the same direction as the wave forcing, has a significant effect on the longshore current velocity distribution. If this alongshore pressure gradient varies weakly in the alongshore direction, the current velocity can be obtained from the local force balance. With increased modulation, the inertia effect gains importance and the local approach is no longer valid. In the cases of opposed forcing, the computed longshore current velocity profiles matched the measured longshore currents, with velocity maxima over the bar, analogous to the laboratory data.

Summarising, the preceding conclusions imply that in absence of an alongshore pressure gradient the maximum longshore current velocity occurs near the areas of most intense breaking, and that the occurrence of velocity maxima in the trough, as often observed in the field, can be ascribed to the presence of an alongshore pressure gradient (excluding wind effects).

Using a spectral analysis technique based on the Maximum Entropy Method the longshore current dynamics during the laboratory experiment could be analysed in detail. Using the zero-mode edge-wave dispersion as a reference, this analysis clearly showed the generation of alongshore exponentially growing shear instabilities. The dispersion curves thus obtained were almost linear, with a phase speed of order of 70 % of the maximum longshore current velocity. The downstream shear instability conditions for the various tests differed considerably, indicating that the growth is a delicate balance of forcing and damping. The results also showed that there is a significant influence of the beach profile on the occurrence of shear instabilities. They did occur on a barred beach but were not observed on a non-barred beach though the back shear was of similar magnitude. This was explained by the fact that the position of the maximum longshore current velocity in the case of a planar beach is closer to shore, rendering a more stable longshore current.

A comparison between measurements of the longshore current dynamics and computational results obtained from linear and non-linear modelling has been performed. In general the correspondence between computations and measurements is good. This is especially so for the frequency-alongshore wave number signatures of the shear instabilities, implicating a good match of the computed and measured phase speeds. Still, uncertainties in the prediction of the initial growth rate exist if a linear stability analysis is used. Both in the measurements and in the non-linear model computations, the observed shear instabilities were very robust all along the beach. As a case of interest the bottom friction was reduced, no longer requiring a good match with the measured longshore current velocity profile, resulting in more energetic vorticity motions.

The interaction of the shear instabilities with the longshore currents has been examined. A detailed analysis of the measured cross-shore momentum flux showed an alongshore increasing cross-shore flux, becoming of comparable order as the mixing associated with breaking wave induced turbulence. However, no significant downstream changes in the mean longshore current velocity profile were detected. The same behaviour was observed in the numerical computations over the domain of the laboratory basin. This is explained by the fact that the shear instabilities take only effect near the downstream end, showing a strong increase over a short distance making inertia effects important, whereas the wave forcing is present all along the beach.

The computations with an extended numerical basin indicate that equilibrium for the shear instabilities was not yet reached during the experiment. The cross-shore component of the shear instability velocity reaches an equilibrium at approximately 35 m from the inflow opening (whereas the available length of the basin was 32 m including outflow effects), as does the mean longshore current profile. The latter does now exhibit the anticipated smoothing of the velocity

profile, overcoming the earlier mentioned inertia effects.

The changes in the longshore current due to the presence of shear instabilities are significant and therefore important to any related quantities such as the transport of sediment. Using the results obtained from a linear stability analysis in an iterative procedure, the shear instability momentum transfer can be incorporated in the computation of longshore currents on an alongshore uniform beach.



## Samenvatting

Laboratorium experimenten zijn uitgevoerd om de instabiliteit van golfgedreven langsstromen te onderzoeken. Door de recirculatie in het basin te minimaliseren werd een nagenoeg uniform in langsrichting golfgedreven stroming verkregen.

Op basis van de experimenten concluderen we dat voor een puur golfgedreven stroming de positie van het maximum van de langsstroom overeenkomt met de positie van het meest intense breken, dat wil zeggen op de bank en nabij de waterlijn. De laterale menging die plaatsvindt zorgt voor een gladder stroom profiel maar heeft relatief weinig invloed op de positie van de maximum langsstroomsnelheid. Dit is het geval voor stroming aangedreven door korte, lange danwel onregelmatige golven.

De geanalyseerde meetdata voor golven en tijdsgemiddelde stroming zijn vervolgens gebruikt voor de verificatie en validatie van een numeriek model voor golfgedreven langsstroming, met in langsrichting uniforme condities, gebaseerd op reeds bestaande vergelijkingen. De vergelijking tussen berekeningen en metingen laat zien dat een goede overeenkomst aanwezig is voor golfhoogte, set-up en golfgedreven langsstroming. De toevoeging van laterale menging geïnduceerd door het breken van golven is daarbij belangrijk. Verder is de landwaartse verschuiving van de golfkrachten door het gebruik van een rollermodel essentieel voor een betere voorspelling van de gemeten golfgedreven langsstroomsnelheden in de trog.

Het aldus geverifieerde model voor de golfgedreven langsstroom is daarna voorzien van een extra term die een constante drukgradient in langsrichting weergeeft. Dit teneinde het effect van bodem-geïnduceerde set-up gradiënten op de golfgedreven langsstroom te onderzoeken in relatie tot de gemeten langsstroming in het veld tijdens de DELILAH meetcampagne in Duck, North Carolina. Deze analyse laat zien dat tijdens die metingen er een niet te verwaarlozen drukgradiënt in langsrichting aanwezig was. Het geval van een relatief kleine drukgradiënt opererend in dezelfde richting als de golfkrachten laten een significante toename van de langsstroomsnelheid zien in de trog. De lokale krachtenbalans om de langsstroom te berekenen kan gebruikt worden in het geval de drukgradiënt langzaam varieert in de ruimte. Bij een toenemende variatie kunnen traagheids-effecten niet langer verwaarloosd worden en dient een meer complexe modellering toegepast te worden. In het geval dat de relatief kleine drukgradiënt in tegenovergestelde richting van de golfkrachten werkt zijn de effecten op de langsstroom klein.

Samenvattend stellen we vast dat in het geval er geen drukgradiënt in langsrichting aanwezig is, het maximum van de golfgedreven langsstroming zich bevindt in de nabijheid van de lokaties waar golven breken, dus nabij de top van de bank en de waterlijn. Het feit dat de DELILAH-veldmetingen een maximum

langsstroom in de trog laten zien kan aldus toegeschreven worden aan de aanwezigheid van een drukgradiënt in langsrichting (waarbij de effecten van wind niet in beschouwing zijn genomen).

Door gebruik te maken van een spectrale analyse techniekgebaseerd op de Maximum Entropy Methode is de dynamica van de golfgedreven langsstroming tijdens de laboratorium experimenten in detail geanalyseerd. Deze analyse demonstreert het ontstaan en de verdere exponentiële groei van instabiliteiten op een overtuigende manier. De aldus verkregen dispersiekrommen zijn nagenoeg lineair met een bijbehorende fasesnelheid in de orde van 70 % van de maximum langsstroomsnelheid. De intensiteit van de instabiliteiten benedenstrooms varieert aanzienlijk daarmee duidend op het feit dat de groei een delicate balans is tussen aandrijving en dissipatie. De resultaten laten overigens ook duidelijk de invloed van het onderliggende bodemprofiel zien. Zonder de aanwezigheid van een brekerbank treden de instabiliteiten niet op. Dit heeft te maken met de positie van het maximum van de golfgedreven stroming. Indien dit zich dichterbij de waterlijn bevindt, zoals in het geval zonder brekerbank, zal de stroming stabielere zijn.

Vervolgens is een vergelijking uitgevoerd tussen gemeten en berekende instabiliteiten in de golfgedreven langsstroming verkregen middels een lineaire en niet-lineaire stabiliteitsanalyses. Dit laat over het algemeen een goede overeenkomst zien. Dit is met name voor de voorspelde frequentie-golfgetal bandbreedte. Echter de voorspelling van de initiële groei is minder goed in het geval gebruik wordt gemaakt van de lineaire stabiliteitsanalyse. Zowel de metingen als de niet-lineaire berekeningen lieten coherente instabiliteiten zien. In de berekening is vervolgens een gevoeligheidstest gedaan met een veel kleinere bodemwrijving wat resulteerde in beduidend sterkere instabiliteiten.

De interactie tussen de instabiliteiten en de golfgedreven langsstroom is in detail onderzocht. De gemeten laterale menging tengevolge van de aanwezigheid van instabiliteiten in de langsstroming is vastgelegd middels een uitgebreide analyse. Dit liet een in langsrichting groeiende invloed van de laterale menging zien. Echter in de golfgedreven langsstroming is die invloed niet zichtbaar met slechts minimale veranderingen in het snelheidsprofiel. Hetzelfde beeld was te zien in de numerieke resultaten. Dit is verklaard vanuit de optiek dat de instabiliteiten pas effectief worden in het benedenstroomse gedeelte, met een sterke toename over een korte afstand zodat traagheidseffecten belangrijk zijn, in tegenstelling tot de golfkrachten die in het hele domein aanwezig zijn.

Door vervolgens in de numerieke berekeningen uit te gaan van een langer basin kon vastgesteld worden dat tijdens de proeven het evenwicht nog niet bereikt was. Met name de dwarscomponent van de instabiliteitssnelheden bereikt zijn evenwicht op zo'n 35 m vanaf de instroom (tijdens de proeven was de beschikbare lengte 32 m), evenals de golfgedreven langsstroom. De laatste laat nu



inderdaad de verwachte aanpassingen zien, i.e. een gladder stroomprofiel, nu traagheidseffecten niet meer van belang zijn.

De aanpassingen van de golfgedreven langsstroming in de aanwezigheid van instabiliteiten zijn substantieel en daarmee van belang voor enig gerelateerde grootheden zoals het transport van sediment. Door de resultaten van de lineaire stabiliteitsanalyse in een iteratieve procedure te gebruiken kan de invloed van de instabiliteiten op de golfgedreven langstroming op een relatief eenvoudige wijze in de berekening worden meegenomen.



# List of symbols

## Roman symbols

$A$	roller area
$B$	breaking coefficient
$C_d$	drag coefficient
$D_r$	roller energy dissipation
$D_w$	wave energy dissipation
$E_r$	roller energy
$E_w$	wave energy
$F_i$	wave forcing operating in $i$ -direction
$H$	wave height
$H_i$	incident wave height
$H_{max}$	maximum wave height
$H_{rms}$	root mean square wave height
$L$	wave length
$L_p$	wave length at peak period
$L_r$	roller length
$L_x$	cross-shore length scale
$L_y$	alongshore length scale
$Q$	fraction of breaking waves
$R$	mixing due to shear instabilities
$R_c$	wave reflection coefficient
$R_{vt}$	mixing associated with wave breaking
$S$	spectral density
$S_{ij}$	wave radiation stresses
$T$	wave period
$U$	depth-averaged mean cross-shore current velocity
$U_l$	Ursell number
$U_w$	wind speed
$V$	depth-averaged mean alongshore-shore current velocity
$V_{max}$	maximum longshore current velocity

$X_b$	cross-shore position of $V_{max}$
$c$	phase velocity
$c_f$	friction coefficient
$c_g$	group velocity
$d$	still water depth
$e$	basis of natural logarithm
$e_w$	wave asymmetry
$f$	frequency
$f_p$	peak frequency
$f_s$	longshore current back shear
$g$	gravitational acceleration
$h$	mean water depth (including set-up)
$h_b$	water depth at breaking
$h_t$	water depth in trough
$i$	$= \sqrt{-1}$ , imaginary unit
$k$	wave number
$k_N$	Nikuradse bottom roughness
$k_i$	imaginary part of wave number
$k_r$	real part of wave number
$k_y$	alongshore wave number
$m$	bottom slope
$q$	cost function
$r$	spatial lag
$t$	time
$u$	short-wave and depth averaged cross-shore velocity
$\tilde{u}$	near-bed wave orbital velocity
$v$	short-wave and depth averaged alongshore velocity
$x$	horizontal cross-shore coordinate
$y$	horizontal alongshore coordinate
$z$	vertical coordinate
$z_b$	bottom level with respect to offshore depth

## Greek symbols

$\alpha$	wave breaking parameter
$\beta$	angle of wave front
$\gamma$	wave breaking parameter
$\delta$	modulation parameter
$\Delta t$	time step

$\epsilon$	modulation parameter
$\zeta$	short wave averaged free-surface elevation
$\bar{\eta}$	set-up/set-down of mean water level
$\theta$	wave incidence angle
$\theta_b$	wave incidence angle at breaking
$\theta_w$	wind direction
$\kappa$	von Karman constant
$\mu$	lagrangian multiplier
$\nu_t$	eddy viscosity associated with wave breaking
$\xi$	surf similarity parameter
$\rho$	fluid density
$\tau_{ij}$	bottom shear stress tensor
$\tau_t$	shear stress at trough level
$\phi$	cross-spectral values
$\omega$	wave frequency
$\omega_i$	imaginary part of wave frequency
$\omega_r$	real part of wave frequency
$\Omega$	potential vorticity

## Superscripts

*	complex conjugate
---	-------------------

## Subscripts

$i, j$	indices being $x$ or $y$
$x, y$	indices corresponding to cross-shore and alongshore direction
0	reference point

## Additional symbols

$\mathcal{E}$	entropy
Im	imaginary part
Re	real part



# Contents

<b>Abstract</b>	<b>vii</b>
<b>Samenvatting</b>	<b>xi</b>
<b>List of symbols</b>	<b>xv</b>
<b>1 Introduction</b>	<b>15</b>
1.1 General . . . . .	15
1.2 Longshore current dynamics . . . . .	17
1.2.1 Shear instabilities . . . . .	17
1.2.2 Alongshore inhomogeneity . . . . .	18
1.3 Outline of thesis . . . . .	19
<b>2 Laboratory Experiment: Mean wave and flow properties</b>	<b>21</b>
2.1 Introduction . . . . .	21
2.2 Experimental set-up . . . . .	21
2.3 Test Conditions . . . . .	23
2.4 Instruments . . . . .	25
2.5 Recirculation . . . . .	26
2.6 Barred beach conditions . . . . .	28
2.7 Non-barred beach conditions . . . . .	36
2.8 Conclusions . . . . .	38
<b>3 Laboratory Experiment: Dynamic flow properties</b>	<b>39</b>
3.1 Introduction . . . . .	39
3.2 Spectral Analysis . . . . .	40
3.3 Results . . . . .	43
3.3.1 Frequency Domain . . . . .	43
3.3.2 Wavenumber Domain . . . . .	47
3.4 Conclusions . . . . .	53

<b>4</b>	<b>Modelling of longshore currents</b>	<b>55</b>
4.1	Introduction . . . . .	55
4.2	Modelling . . . . .	57
4.2.1	Wave transformation . . . . .	57
4.2.2	Current velocity . . . . .	58
4.3	Comparison with laboratory data . . . . .	60
4.3.1	Reduction of equations . . . . .	60
4.3.2	Results . . . . .	62
4.4	Comparison with field data . . . . .	65
4.4.1	Description of experiment . . . . .	65
4.4.2	Reduction of equations . . . . .	67
4.4.3	Comparison . . . . .	69
4.4.4	Weak alongshore variation . . . . .	70
4.4.5	Strong alongshore variation . . . . .	74
4.4.6	Alongshore uniformity . . . . .	77
4.5	Discussion . . . . .	79
4.6	Conclusions . . . . .	80
<b>5</b>	<b>Longshore current instability</b>	<b>83</b>
5.1	Introduction . . . . .	83
5.2	Linear stability analysis . . . . .	85
5.2.1	Model description . . . . .	85
5.2.2	Results . . . . .	87
5.3	Non-linear modelling . . . . .	91
5.4	Discussion . . . . .	100
5.5	Conclusions . . . . .	101
<b>6</b>	<b>Effects of instabilities on the longshore current</b>	<b>103</b>
6.1	Introduction . . . . .	103
6.2	Spatial structure . . . . .	104
6.3	Cross-shore momentum flux . . . . .	107
6.4	Importance in longshore current modelling . . . . .	108
6.5	Equilibrium conditions . . . . .	111
6.6	Conclusions . . . . .	113
<b>7</b>	<b>Discussion</b>	<b>117</b>
7.1	Introduction . . . . .	117
7.2	Planar beach conditions . . . . .	117
7.3	Vortex shedding . . . . .	118
7.4	Shear instabilities and longshore current modelling . . . . .	120
	<b>Acknowledgements</b>	<b>124</b>



<i>CONTENTS</i>	3
<b>References</b>	<b>126</b>
<b>Appendix A</b>	<b>131</b>
<b>Curriculum Vitae</b>	<b>133</b>



# List of Figures

1.1	Definition sketch . . . . .	16
2.1	Layout of experimental set-up, position of current meters in alongshore array denoted by markers. . . . .	23
2.2	Upper panel: Instruments attached to the mobile carriage during the experiments. Lower panel: Bottom profile used throughout the experiments with mean water level for barred (dashed) and non-barred (dotted) beach profiles. . . . .	26
2.3	Measurements test SA243. Upper left panel: Wave height distribution. Upper right panel: Set-up of mean water level. Lower panel: Longshore current velocity profile. . . . .	28
2.4	Dispersion of dye for test SA243 showing a bimodal longshore current velocity structure. ( Dye experiment performed by Pieter Pasterkamp, Piet Rorije and the author all present on the mobile carriage.) . . . . .	29
2.5	Measurements test SA337. Upper left panel: Wave height distribution. Upper right panel: Set-up of mean water level. Lower panel: Longshore current velocity profile . . . . .	30
2.6	Measurements test SA432. Upper left panel: Wave height distribution. Upper right panel: Set-up of mean water level. Lower panel: Longshore current velocity profile . . . . .	32
2.7	Measurements test SA635. Upper left panel: Wave height distribution. Upper right panel: Set-up of mean water level. Lower panel: Longshore current velocity profile . . . . .	33
2.8	Measurements test SA537. Upper left panel: Wave height distribution. Upper right panel: Set-up of mean water level. Lower panel: Longshore current velocity profile . . . . .	34
2.9	Measurements test SO014. Upper left panel: Wave height distribution. Upper right panel: Set-up of mean water level. Lower panel: Longshore current velocity profile . . . . .	35

2.10	Measurements test SC219. Upper left panel: Wave height distribution. Upper right panel: Set-up of mean water level. Lower panel: Longshore current velocity profile . . . . .	36
2.11	Measurements test SC315. Upper left panel: Wave height distribution. Upper right panel: Set-up of mean water level. Lower panel: Longshore current velocity profile . . . . .	37
3.1	Left panel: Co-and quad values, $\phi(r)$ , used in spectral estimates expressed in $m^2/Hz$ . The values at lags 4 and 6 have been omitted in the case Lagrangian multipliers are used. Right panel: Spectral estimates based on eq. 3.7 (dashed) and using Lagrangian multipliers (dotted) eq. 3.12 vs. target spectrum (solid) . . . . .	43
3.2	Alongshore velocity spectra obtained from EMF 01 in the upper left hand corner to EMF 12 in the lower right hand corner, showing the energy density, $S$ , in $(m/s)^2/Hz$ as function of frequency in Hz for test SA243 . . . . .	44
3.3	Snap shots with an interval of approximately 4 seconds (starting in the upper left corner going from left to right) of the experimental set-up and wave field during test SA243. . . . .	45
3.4	Low-frequency alongshore (dash-dotted) and cross-shore (solid) velocity spectra obtained from EMF 01 in the upper left hand corner to EMF 12 in the lower right hand corner, showing the energy density, $S$ , in $(m/s)^2/Hz$ as function of frequency in Hz for test SA243 . . . . .	46
3.5	Upper panels: Co (drawn) and quad (dashed) values in $(m/s)^2/(Hz)$ of alongshore velocity at the downstream array for $f = 0.0244$ Hz (left) and $0.0407$ Hz (right) for test SA243. Lower panels: Corresponding wave number spectra in $(m/s)^2/(m^{-1}Hz)$ . . . . .	47
3.6	Test SA243: $f - k_y$ -spectrum for alongshore velocity obtained from the upstream (left panels) and downstream array (right panels) displayed as a surface plot (upper panels) and contourplot (lower panels) with contours at .1 .2 .5 1 2 5 10 20 50 $(m/s)^2/(m^{-1}Hz)$ . The zero-mode edge wave dispersion curves for a plane beach indicated by dashed lines. . . . .	48
3.7	Alongshore growth of total variance in 0 to 0.1 Hz frequency band for alongshore velocities (left panel) and cross-shore velocities (right panel) during test SA243. . . . .	49
3.8	$f - k_y$ -spectrum for alongshore velocity obtained from downstream array for Tests SA337 (left upper panel), SA432 (upper right), SA635 (lower left) and SA537 (lower right). Spectral energy density expressed in $(m/s)^2/(m^{-1}Hz)$ . . . . .	50

- 3.9  $f-k_y$ -spectrum for alongshore velocity obtained from downstream array for Test SO014. Spectral energy density expressed in  $(\text{m/s})^2/(\text{m}^{-1}\text{Hz})$ . The zero-mode edge wave dispersion curves for a plane beach indicated by dashed lines. . . . . 52
- 4.1 Left panel: Wave height transformation, comparison between computational results (solid line) and measurements. Right panel: Set-up of mean water level computed with (solid line) and without (dashed line) the roller contribution, compared with measurements. 62
- 4.2 Computed longshore current velocities. Upper left panel: Using linear,  $c_f = 0.015$  (dashed line) and non-linear,  $c_f = 0.007$  (solid line) bottom shear stress. Upper right panel: Without mixing. Lower left panel: Without a roller. Lower right panel: Without a roller and without mixing. Measurements at  $y = 21.50 \text{ m}$  ( $x$ ) and bottom profile (dotted line, not to scale) are given as a reference. 63
- 4.3 Left panel: Plan view of Field Research Facility at Duck, North Carolina. Offshore pier direction coincides with east. Right panel: Part of minigridd with bathymetry of 10 Oct. Position of velocity meters and colocated pressure transducers denoted by x's. . . . . 66
- 4.4 Time lapse video exposures of the nearshore on 10 (upper left), 12 (upper right), 15 (lower left) and 19 (lower right) October. . . . . 67
- 4.5 Left panel: Bathymetry for computational domain obtained for 10 Oct. Middle and neighbouring transects indicated by vertical lines; corresponding profiles shown in right panel. . . . . 70
- 4.6 Left panel: Computed transformation of  $H_{rms}$  at the measurement transect (solid line) compared with measurements (+). Right panel: Fraction of breaking waves for Oct. 10, measurements (o) and model results obtained for  $e_w = 0.5$  (dash-dotted line),  $e_w = 0.7$  (solid line) and  $e_w = 0.9$  (dashed line). . . . . 72
- 4.7 Conditions on Oct 10. Upper left panel:  $H_{rms}$  at the measurement transect computed (solid) and measured ('+',), the southerly (dashed) and northerly transect (dash-dotted) respectively. Upper right panel: corresponding computed set-up. Lower left panel: Wave forcing (solid) and local alongshore pressure gradient (dashed). Lower right panel: Longshore current velocities using  $c_f = 0.0035$  with (dashed) and without (solid) the local pressure gradient. Bottom profile (dashed) is given as a reference (not to scale). 73

- 4.8 Conditions on Oct 12. Upper left panel: Bathymetry. Upper right: Corresponding bottom profiles. Lower left panel: Computed wave forcing (solid) and local alongshore pressure gradient (dashed). Lower right panel: Computed longshore current velocities (solid line), without pressure gradient (dashed line) and without mixing (dash-dotted line) with  $c_f = 0.006$ . Measurements denoted with 'x'. 74
- 4.9 Conditions on Oct 12. Left panel: Synoptic view of the set-up of the mean water level in m. Right panel: Estimated forcing along the beach over the trough due to the presence of an alongshore pressure gradient. Lower panel: Corresponding longshore current velocity in the trough with (solid) and without inertia terms (dashed). . . . . 76
- 4.10 Conditions Oct 19. Upper left: Bathymetry. Upper right: corresponding bottom profiles. Lower left: Forcing due to wave breaking (solid) and local alongshore pressure gradient (dashed). Lower right: Corresponding longshore current velocities with local pressure gradient (solid line) and without (dashed line) for  $c_f = 0.0035$ . Measurements denoted by 'x'. . . . . 78
- 4.11 Conditions on Oct 18. Left panel: Wave (solid) and pressure forcing (dashed) and corresponding longshore current velocities (right panel) with the local pressure gradient (solid line) and without (dashed line) using  $c_f = 0.0035$ . Measurements denoted by 'x'. . . . . 80
- 5.1 Left panel: Instability curves for test SA243. Without damping (dashed line), with bottom friction (dash-dotted) and eddy viscosity plus bottom friction (solid line). Right panel: Instability curves for tests SA243 (solid), SA337 (dashed) and SO014 (dash-dotted) with bottom friction and eddy viscosity. . . . . 88
- 5.2 Left panels: Comparison of measured and computed (denoted by '+' signs) dispersion curves at the upstream (left) and downstream end (right) for tests SA243 (upper panels), SA337 (middle panels) and SO014 (lower panels). Zero mode edge wave dispersion curve depicted as a reference (dashed). . . . . 89
- 5.3 Alongshore increase of shear instability variance of alongshore velocity in frequency band from 0 to 0.1 Hz (circles) for Test SA243. Computational results (solid line) obtained from linear stability analysis with full damping. Similar results for tests SA337 (right) and SO014 (lower panel) . . . . . 90
- 5.4 Model definition and bathymetry . . . . . 92

5.5 Upper left panel: Comparison of computed wave transformation with measurements, test SA243. Computational results obtained for  $\alpha = 1$ ,  $\gamma = .55$  and  $n = 10$ . Upper right panel: Comparison of computed wave set-up for  $\beta = .1$  and measurements, test SA243. Similar for test SA337 (lower panels). . . . . 94

5.6 Mean longshore current velocity profiles obtained for a bottom roughness of  $k_N = 0.005$  m (upper left),  $k_N = 0.004$  m (upper right),  $k_N = 0.003$  m (lower left) and  $k_N = 0.002$  m (lower right) at various transects. . . . . 95

5.7 Comparison of mean longshore current profiles. Computations at 8.75 m (solid), 15.05 (dashed), 21.35 m (dash-dotted) and 26.95 m (dotted line) obtained with  $k_N = 0.0035$  m for tests SA243 (left panel) and SA337 (right panel). Bottom profile shown as reference (lower dashed line) . . . . . 96

5.8 Upper panel: Snapshot of alongshore development of computed potential vorticity for test SA243. Similar for test SA337 (lower panel). Potential vorticity  $\Omega$  expressed in  $(\text{ms})^{-1}$ . . . . . 98

5.9 Measured (upper panels) and computed (lower panels) dispersion curves based on linear stability analysis (indicated by '+' ) and non-linear modelling for tests SA243 (left) and SA337 (right). Zero-mode edge wave dispersion lines indicated by dashed lines. . . . . 99

5.10 Alongshore development of integrated spectral density based on the alongshore shear instability velocities for test SA243 (left) and test SA337 (right). Computed results, obtained with  $k_N = 0.0035$  m, indicated by crosses vs. measurements indicated by circles. . . . . 100

6.1 Left panel: Energy density of  $u$  (dashed line) and  $v$  (solid line). Left panel:  $x = 4.5$  m and  $y = 27.25$  m. Right panel:  $x = 3.0$  m and  $y = 27.25$  m. . . . . 104

6.2 Left panels: Contours of variance of  $v$  (upper) and  $u$  (lower) developing along the beach in the band  $f = 0.0407$  Hz  $\pm 0.00205$  Hz. Right panels: Cross-sections of this variance at  $y = 11.25$  m (dashed),  $y = 24.75$  m (solid) and  $y = 31.25$  m (dotted) respectively. Measurements indicated by the markers. Test SA243. . . . . 105

6.3 Left panels: Contours of variance of  $v$  developing along the beach in the bands  $f = 0.028$  Hz  $\pm 0.00205$  Hz (upper) and  $f = 0.048$  Hz  $\pm 0.00205$  Hz (lower panel). Right panels: Corresponding cross-sections of this variance at  $y = 11.25$  m (dashed),  $y = 24.75$  m (solid) and  $y = 31.25$  m (dotted) respectively. Test SA243. . . . . 106

- 6.4 Left panel: Frequency distribution of shear instability momentum flux,  $R'$ , at 27.25 m from the inflow opening expressed in  $\frac{m^3}{s^2}/\text{Hz}$ . Right panel: Frequency integrated momentum flux at same position. 107
- 6.5 Alongshore development of integrated momentum transfer induced by shear instabilities (left panel) and corresponding forcing (right panel). Distance to the inflow opening given by  $y$ . Measurements (markers) connected by a spline. Estimated lateral mixing (left panel) and wave forcing (right panel) given as a reference (dashed line). . . . . 109
- 6.6 Upper panel: Synoptic view of computed shear instability cross-shore momentum transfer expressed in  $(m^3/s^2)$  for  $k_N = 0.0035$  m. Lower panels: Comparison of measured (left) and computed (right) momentum transfer at various cross-sections. Measurements (markers) connected by a spline. Estimated lateral mixing (left panel, dashed line) added as a reference. . . . . 112
- 6.7 Alongshore development of integrated spectral density based on the alongshore (left panel) and cross-shore (right panel) shear instability velocities for the extended basin. Computed results, obtained with  $k_N = 0.0035$  m, indicated by circles vs. measurements indicated by crosses. . . . . 113
- 6.8 Snapshot of potential vorticity contours between  $y = 0$  m and  $y = 40$  m (upper panel) and between  $y = 40$  m and  $y = 80$  m (middle panel) for the extended basin. Lower panel: Mean longshore current velocity profiles obtained for  $k_N = 0.0035$  m at transects located at 15.05 m (solid), 27.25 m (dashed), 35.00 m (dash-dotted) and 51.80 m (dotted) from the inflow. Bottom profile (lower dashed line, not to scale) and measurements (markers) shown as a reference. . . . . 114
- 7.1 Contours of negative (dashed) and positive (solid) potential vorticity in the extended basin for  $k_N = 0.0035$  m (upper) and  $k_N = 0.0005$  m (lower panel) . . . . . 119
- 7.2 Alongshore development of computed mean longshore current velocity profiles in the extended basin for  $k_N = 0.0035$  m (left) and  $k_N = 0.0005$  m (right panel). Measurements indicated by the markers given as a reference. . . . . 121



- 7.3 Upper left panel: Forcing of shear instabilities estimated from linear stability analysis (solid line) and wave forcing (dashed line). Upper right panel Corresponding longshore current profile with (dashed) and without (solid) shear instability momentum transfer. Lower panels: Similar results obtained for the case without damping. Measurements indicated by the markers given as a reference. . . . . 122



# List of Tables

2.1	Conditions used throughout the experiment, $H$ represents the wave height at the wave maker and $T$ the corresponding wave period, except for the case of random waves where $H$ represents the root mean square wave height and $T$ the peak period. . . . .	25
2.2	Distance of electromagnetic current velocity meters (EMF) and wave height meters (WHM) from the beach. . . . .	27
3.1	Distance of electromagnetic current velocity meters (EMF) from the inflow opening . . . . .	39
3.2	Summary of results obtained from the experiment. $c$ : phase speed, $V_{max}$ : maximum longshore current velocity, FGM: $k_y$ : position FGM along the $k_y$ -axis, FGM: $f$ : similar but along the frequency axis. . . . .	53
4.1	Test Conditions, $\delta h$ : tidal elevation relative to mean sea level, $H_{rms}$ , $T_p$ and $\theta$ all at 8 m water depth. $h_b$ : depth at breaking, $V_{max}$ : maximum longshore current velocity, $U_w$ : wind speed and $\theta_w$ : wind direction with respect to the coast normal. . . . .	70
5.1	Relative intensity of instabilities with respect to the incident waves, expressed in root mean square velocity ratio $U' = U_{rms,lo}/U_{rms,hi}$ , as a function of normalised alongshore distance, $y' = y/L_p$ , where $L_p$ represents the instability peak-wave length of 7.5 m; the pass frequency was set at 0.5 Hz and $U_{rms,hi}$ is $O(.25)$ m/s. . . . .	101



# Chapter 1

## Introduction

### 1.1 General

The longshore current: defined by a relatively narrow strip of the beach with a strong transport of water parallel to the shore line. The driving force for the longshore current is predominantly governed by the obliquely incident breaking waves. Out at sea the wind-generated waves radiate away from the center of depression, thereby transporting energy, mass and momentum. As the waves propagate toward more shallow waters they start 'feeling' the bottom and their propagation speed slows down with decreasing depth. In the case of obliquely incident waves this results in wave refraction due to the difference in propagation speed along the wave crests. At further decreasing water depths shoaling becomes evident up to a point where the waves become unstable and breaking occurs. A broken wave can be easily recognised by the aerated water at the front, known as a roller, which results from the inclusion of air-bubbles by the overtopping wave crest.

Several processes can be distinguished in the area where waves are breaking. The roller is advected with the phase speed of the wave, thereby exerting a shear stress at the slower moving underlying water mass. On a small scale this roller energy is transformed into turbulent kinetic energy (e.g. Roelvink and Stive, 1989, Nairn et al., 1989). This turbulence, being transported downward through the watercolumn, redistributes momentum throughout the vertical plane and stirs up additional sediment once it reaches the bottom. In the cross-shore direction the wave induced forcing is balanced by a gradient in the set-up of the mean water level (Longuet-Higgins and Stewart, 1964). However, given the vertical imbalance between the wave forcing and the set-up in combination with the wave induced mass transport a return flow results (Dyhr-Nielsen and Sørensen, 1970). In the case of obliquely incident breaking waves, the shear stress induced by the roller has a shore-parallel component, thereby generating a longshore cur-

rent, which in turn is balanced by a bottom shear stress. A sketch of the various phenomena is shown in Figure 1.1.

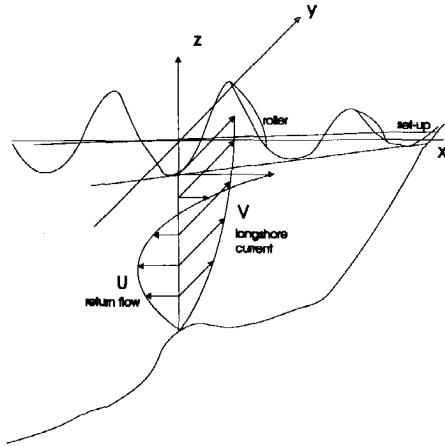


Figure 1.1: *Definition sketch*

As a feature the longshore current has less appeal than a so-called rip-current, where water transported onshore by the incident waves is pushed offshore in a narrow jet, with high velocities which can take a swimmer involuntarily far out to sea. Possibly because of their lesser threat to swimmers, the longshore current is less well known by the general public. Still, considering the mass of water that is actually transported, the longshore current is an order of magnitude larger than the less-frequently occurring rip-currents. It is the most important transport mechanism of sediment in the surfzone, known as the littoral drift. Obstruction of this drift results in an area of accretion, followed by erosion of the beach at the down-drift end, a well known phenomenon observed at many a harbour entrance. The importance of wave-driven longshore currents in coastal processes has long been established and much research has been done to model the longshore current velocity accurately (Bowen, 1969, Thornton, 1970, Longuet-Higgins, 1970). Traditionally these analyses are based on assumed alongshore uniformity and steady state conditions. This greatly facilitates the model equations and efficient modelling of the wave transformation and corresponding longshore currents becomes possible.

The fact that longshore currents are often far from being steady has been noted as early as 1957 (Stoker) and more recently during the SUPERDUCK field experiments in 1986 (Oltman-Shay et al., 1989). And contrary to the assumption

of alongshore uniformity, the longshore current is more likely to be inhomogeneous in the alongshore direction. These more recent observations have triggered a new research effort into the characteristics of longshore currents (Bowen and Holman, 1989, Dodd and Thornton, 1990, Putrevu and Svendsen, 1992, and others).

In this thesis, in line with the observations mentioned above, two phenomena associated with the dynamics of longshore currents will be examined: the presence of shear instabilities and the bathymetry-induced alongshore inhomogeneity of longshore currents.

## 1.2 Longshore current dynamics

### 1.2.1 Shear instabilities

During the SUPERDUCK experiment at Duck, North Carolina, shear instabilities in a wave-driven longshore current were first identified by Oltman-Shay et al. [1989]. Shear instabilities are more or less periodic disturbances in an otherwise uniform longshore current. Their presence results in an apparently meandering longshore current. They are advected with the longshore current with a phase speed in the order of half of the extremum of the longshore current velocity. This is far slower than the phase speed at the same frequency associated with edge waves. Bowen and Holman [1989] introduced the theoretical background based on the conservation of potential vorticity. They obtained a linear stability equation for longshore currents, showing with a simplified test case (horizontal bottom) that the backshear of the longshore current, i.e. the offshore cross-shore velocity gradient, is very important in the generation of shear instabilities. A strong back shear makes the longshore current unstable to a wide range of small perturbations. This was confirmed by Dodd and Thornton [1990] and Putrevu and Svendsen [1992] using more realistic longshore current velocity and bottom profiles. Falqués et al. [1994] showed that the distance of the peak of the longshore current velocity to the shoreline,  $X_b$ , is also important in the generation of the longshore instabilities. An increase in  $X_b$  results in a wider range of unstable wave numbers. The generation of shear instabilities is strongly affected by the presence of dissipative effects. Putrevu and Svendsen [1992] and Dodd et al. [1992] showed that the number of possible unstable modes and their corresponding growth rate is reduced if dissipation due to bottom friction is increased. The combined effect of bottom friction and eddy viscosity on the stability of wave-driven longshore currents was investigated by Falqués et al. [1994], who show that for eddy viscosity and bottom friction giving rise to similar damping, eddy viscosity gives a stronger reduction of the span of unstable wave numbers compared to bottom friction.

The above mentioned linear stability analysis is only valid for shear instabilities of infinitesimal amplitude, i.e. initial conditions. More detailed analytical and numerical analyses were made using weakly non-linear (Dodd and Thornton, 1992) and fully non-linear modelling (Nadaoka and Yagi, 1993, Deigaard et al., 1994, Falqués et al., 1994, Allen et al., 1995, Özkan and Kirby, 1995, Özkan-Haller and Kirby, 1996 and 1997, Slinn et al., 1998) to describe the development of shear instabilities in wave-driven longshore currents to finite amplitude values.

The relevance of shear instabilities in the prediction of the cross-shore distribution of the longshore current velocity is not clear as yet. Shear instabilities are believed to cause a significant amount of cross-shore momentum transfer (Bowen and Holman, 1989). Numerical studies (Dodd and Thornton, 1992) indicate an inflexion point in this redistribution, resulting in a smoothing of the initial longshore current velocity profile. The redistribution depends on the cross-shore structure of the shear instabilities and the phase coupling between the velocity components. This means that for an accurate prediction of the longshore current velocity profile knowledge is required of the possible existence of shear instabilities and their associated momentum transfer.

## 1.2.2 Alongshore inhomogeneity

As a result of the DELILAH field experiment (Birkemeier, 1991), also performed at Duck, North Carolina, there has been much discussion on the cross-shore distribution of the wave-driven alongshore current velocity on barred beaches. Where comparison of model results with both field (Thornton and Guza, 1986, Church and Thornton, 1993, among others) and laboratory data (Visser, 1984, Svendsen and Putrevu, 1994, among others) for wave-driven longshore currents on planar beaches show in general good agreement, this is not necessarily so for barred beaches. In the case where field measurements show a maximum longshore current velocity in the trough, as observed during the DELILAH field experiment, numerical model studies for uniform longshore currents show that the maximum is near the bar crest with another maximum close to the shore line, corresponding to the locations where wave breaking occurs. However, not all field measurements show this kind of longshore current velocity distribution (Whitford and Thornton, 1995). Several mechanisms have been examined to explain this difference in behaviour, including turbulence effects (Church and Thornton, 1993), rollers (Lippmann et al., 1994), shear instabilities (Church et al., 1992), and alongshore pressure gradients (Putrevu et al., 1995). However, all the effects mentioned previously, with the exception of the alongshore pressure gradient, can at most cause a relatively minor shift of the velocity maximum away from the bar crest. They are not believed to contain a mechanism which would cause the maximum velocity to occur in the trough. Only the pressure



gradient is such a mechanism. The fact that such gradient has not been observed in the field does not exclude it from being a likely cause, simply because a very weak gradient, too weak to be observable under normal conditions, suffices to generate a current with significant velocities. These gradients are likely to be associated with alongshore inhomogeneities in the bathymetry. Variations in the crest level of the bar translate themselves in alongshore variations of the set-up, thereby generating a current in the trough (Putrevu et al., 1995).

### 1.3 Outline of thesis

In the research presented in this thesis the emphasis is on the dynamics of longshore currents, looking at alongshore non-uniformities and slow time modulations of the longshore current velocity. To this end a combination of both laboratory and field experiments with numerical modelling has been used.

First a detailed description is given of the laboratory test set-up and results obtained from the data-analysis of laboratory experiments on wave-driven longshore currents on both barred and non-barred beaches. The objective for the laboratory experiments was twofold: to examine the generation, growth and equilibrium conditions of shear instabilities under controlled conditions. Next, to examine the cross-shore distribution of the longshore current velocities for purely wave-driven currents, with emphasis on the position of maximum current velocity with respect to areas where wave energy is dissipated.

Next the modelling of longshore currents is discussed. The effects of mixing, bottom friction and rollers on the cross-shore distribution of the longshore current velocity are examined in detail with help of numerical modelling. Existing model equations, based on the assumption of alongshore uniformity, are used to compare to the laboratory measurements of wave driven longshore currents on a barred beach in absence of alongshore pressure gradients. However, alongshore uniformity in its true sense is not likely to be met in the field, where small spatial variations in bedlevel and/or wave conditions can be expected. The next step is to use the verified model to establish the relative importance of alongshore pressure gradients induced by longitudinal bed undulations for the longshore current distribution over a barred beach. With this in mind the field measurements obtained during the DELILAH experiment in 1990 at the US Army Corps of Engineers' Field Research Facility at Duck, North Carolina were examined. The approach is analogous to the work done by Putrevu et al. [1995] for the case of planar beaches. However, aside from the difference in bottom profile, attention is focussed on the comparison with measurements versus a hypothetical case.

The longshore current instability is assessed in the following Chapter. First

the stability analysis of wave-driven longshore currents, both linear and non-linear is discussed. The effects of bottom friction and wave dissipation on the shear instability signature are examined. A detailed comparison with the laboratory results is performed, looking at the initial growth rate, the frequency dispersion and finite amplitude conditions. The effects of the shear instabilities on the longshore current velocity profile are treated in the following Chapter. As mentioned previously, the shear instabilities are expected to result in a cross-shore redistribution of momentum. This is examined in great detail using cross-shore spectral analysis to compute the frequency distribution of the shear instability induced momentum flux. The total transfer is obtained by integration over the frequency domain. Comparison is made with model results of the shear instability structure and the associated cross-shore momentum transfer. Numerical modelling is also used to virtually extend the wave basin in order to predict the alongshore development of the longshore current velocity profile at a place where the shear instabilities are in equilibrium.

Finally a discussion is given on the observed phenomena and its relevance for engineering purposes.

## Chapter 2

# Laboratory Experiment: Mean wave and flow properties

### 2.1 Introduction

As mentioned in the Introduction, the objective of the laboratory experiment is twofold. The primary objective is to examine the generation, growth and equilibrium conditions of shear instabilities under controlled conditions to provide measurement data to test theoretical predictions of their dispersion relation and growth rates. An important part of this experiment is to establish longshore currents in the wave basin which are uniform alongshore prior to the onset of shear instabilities. So a second objective is defined: examining the cross-shore distributions of wave-driven longshore currents in absence of an alongshore pressure gradient. This in view of the discussion on the position of the maximum current velocity in relation to the areas where wave energy is being dissipated by breaking. This Chapter treats the set-up of the experiments and the selection of test conditions, given the constraints of the laboratory basin. Next the mean wave and flow properties obtained for the various tests are presented and discussed. Parts of this chapter have been published in Reniers et al. [1994] and Reniers and Battjes [1997]. The dynamic flow properties associated with shear instabilities will be presented separately in Chapter 3.

### 2.2 Experimental set-up

The experimental set-up is predominantly governed by the need to model the generation and growth of shear instabilities accurately. The relevance of shear instabilities to laboratory experiments was already assessed by Putrevu and Svendsen [1992]. Based on their numerical results they find typical length scales of

$O(8)$  m and time scales of  $O(20)$  s for shear instabilities in the Visser experiment [1980, 1984]. In addition they estimate the temporal growth rate of the shear instabilities, concluding that in the Visser experiment the dissipative effects are dominant and therefore suppress the occurrence of shear instabilities. A second assessment was made by Brøker et al. [1994], who used the numerical results of Deigaard et al. [1994] to scale to laboratory conditions. From their analysis it follows that the length of the basin should be substantial, approximately 50 to 100 metres if a root mean square wave height of 10 cm is considered, before shear instabilities become apparent. From these analyses it is clear that attempts to generate shear instabilities under laboratory conditions are not in the least guaranteed to be successful. In order to maximise the possibility for the instabilities to develop, based on the characteristics mentioned in the Introduction, we have opted for the following choices given the restrictions of the available basin:

- maximum length of the beach (more room for the instabilities to develop)
- barred profile (greater distance of back shear to the waterline)
- smooth bottom (small dissipation due to friction)
- large angle of incidence (strong back shear)

Based on these criteria the experimental lay-out was determined as shown in Figure 2.1. A wave basin of approximately 40 m long and 25 m wide was used. A wave generator consisting of individual wave paddles is located at the offshore end of the basin, with a total length of 26.4 m. The paddles were moving in phase in the present experiments. The beach makes an angle of  $30^\circ$  with respect to the wave generator to create a large incident angle and a longer beach with a length of 33 m, and thus more room for instabilities to develop. This means that the distance from the wave generator to the breaker line varies along the beach. In case of first order wave generation this would result in a varying wave field along the breaker line, depending on the phase difference between the first and bound second harmonic and the spurious second harmonic. To avoid this, second order Stokes wave generation has been used, accounting for the bound second harmonics. Variation of the wave field along the breaker line was not assessed explicitly, though intercomparison of the wave height transformation along four different transects showed the wave field to be approximately uniform alongshore. A pump was used to recirculate the longshore current. The maximum pumped discharge was 200 l/s, enough to cover a range of wave conditions. Wave guides at both sides were terminated at some distance from the water line to allow the in- and outflow of the longshore current. The inflow opening had been constructed in such a way that it was possible to distribute the pumped discharge along the cross-shore profile in order to match the wave-driven current and hence increase the length over which the longshore current was uniform.

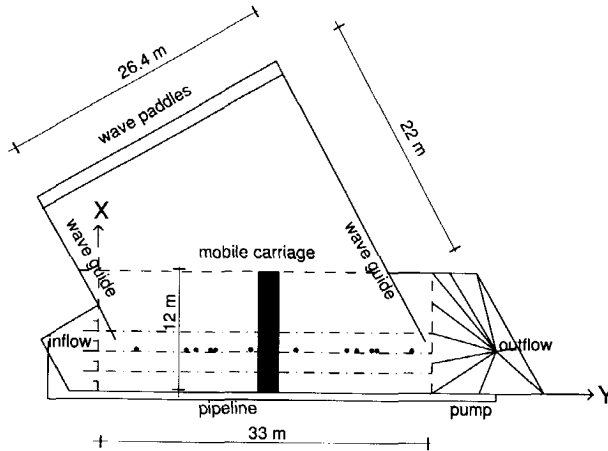


**Figure 2.1:** Layout of experimental set-up, position of current meters in along-shore array denoted by markers.

## 2.3 Test Conditions

The set of experiments had to be completed within a timespan of 8 weeks (this included the time required to build the experimental set-up). This meant that only a limited number of runs with different wave conditions could be performed during the experiment. The idea was to find the conditions most conducive to the generation of shear instabilities. These were arrived at using results from numerical 1D wave transformation and longshore current models (see Chapter 4) combined with a linear stability analysis (see Chapter 5). The following parameters were varied in the computations within the limits imposed by the experimental facility:

- $H$ : wave height
- $T$ : wave period

- $\theta$ : angle of incidence
- $d_0$ : water depth at wave maker
- $z_b$ : bottom profile
- $k_N$ : bottom roughness

These limits are discussed briefly in the following. First the wave maker limitations. The wave periods generated in the basin are typically in the range of 1 to 2 seconds. Then for a given water depth,  $d_0$ , in the order of 50 cm, the maximum wave height,  $H_{max}$ , which can still be generated is in the order of 15 cm. A second and more stringent restriction on the maximum wave conditions results from the requirement that Stokes second order wave theory should be valid at the wave maker. A measure for the amplitude of the bound super harmonic is given by the Ursell number,  $U_l$ :

$$U_l = \frac{HL^2}{d_0^3} \quad (2.1)$$

where  $L$  is the wave length at the wave maker. For Ursell numbers larger than 25 Stokes second order theory is no longer valid. A third restriction is given by the fact that reflections have to be kept at a minimum, to avoid a non-uniform wave field. The reflection coefficients,  $R_c$ , are obtained from an empirical formula based on experimental data (Battjes, 1974):

$$R_c = 0.1\xi^2 \quad (2.2)$$

and:

$$\xi = \frac{m}{\sqrt{\frac{H_i}{L_0}}} \quad (2.3)$$

where  $m$  is the bottom slope,  $H_i$  the local incident wave height and  $L_0$  the deep water wave length. A final restriction is obtained from the pump capacity. The maximum pump discharge has to be able to match the wave-driven discharge to avoid spurious recirculations in the basin. The wave-driven discharge is a function of incidence angle, wave height, bottom profile and bed-roughness. The bottom profile, with a Gaussian bar, was selected with the objective to have intense wave breaking near the bar crest, followed by reforming of the waves in the trough and additional dissipation near the shore line.

Numerous computations were performed to optimise the bottom profile and reach a limited set of potential wave conditions which complied with the restrictions imposed by the experimental facility. By intercomparison of the various computational results and taking into account the previously mentioned restrictions, a final set of experimental conditions was obtained (see Table 2.1).

waves	profile	test	$d$ (cm)	$H$ (cm)	$T$ (s)
regular	barred	SA243	55.0	8.0	1.0
regular	barred	SA337	55.0	10.0	1.0
regular	barred	SA432	55.0	12.0	1.1
regular	barred	SA635	55.0	13.5	1.1
regular	barred	SA537	55.0	8.0	2.0
random	barred	SO014	55.0	6.7	1.2
regular	planar	SC219	45.0	8.0	1.0
regular	planar	SC315	45.0	10.0	1.0

**Table 2.1:** Conditions used throughout the experiment,  $H$  represents the wave height at the wave maker and  $T$  the corresponding wave period, except for the case of random waves where  $H$  represents the root mean square wave height and  $T$  the peak period.

The laboratory experiments have been conducted with monochromatic and random waves with an incidence angle of  $30^\circ$ . The measurements were performed on a barred concrete profile as shown in the lower panel of Figure 2.2, with a 1 : 20 slope offshore. The bar profile had a crest height of about 0.1 m, which resulted in an approximately 1 : 8 slope on the seaward side of the bar. Shoreward of the bar, a plane 1 : 10 slope extended to an elevation above the expected run-up. Lowering the water level below the bar crest in combination with the same incident wave conditions as for the higher water level gave the opportunity to assess the effect of the presence of the bar on the generation of the instabilities. For the wave conditions used throughout the experiment, the wave reflection was expected to be less than 5%, with the exception of test SA537 where reflections are expected to be up to 10%.

## 2.4 Instruments

A set of 8 two-dimensional electromagnetic velocity meters (EMF) was used to measure the cross-shore distribution of the flow field. The 8 EMF's had a disk shape with a diameter of 3.3 cm. Calibration of the instruments was performed prior to the experiments, showing linear behaviour for velocities up to 1 m/s with an accuracy in the order of 1 cm/s. The current velocity meters were set at  $1/3$  of the water depth from the bottom. The cross-shore array of 8 EMF's was attached to a mobile carriage (Figure 2.2) to monitor the cross-shore distribution of the longshore current velocity. In addition 10 resistant type wave gauges were mounted on the carriage to monitor the wave transformation and set-up of the

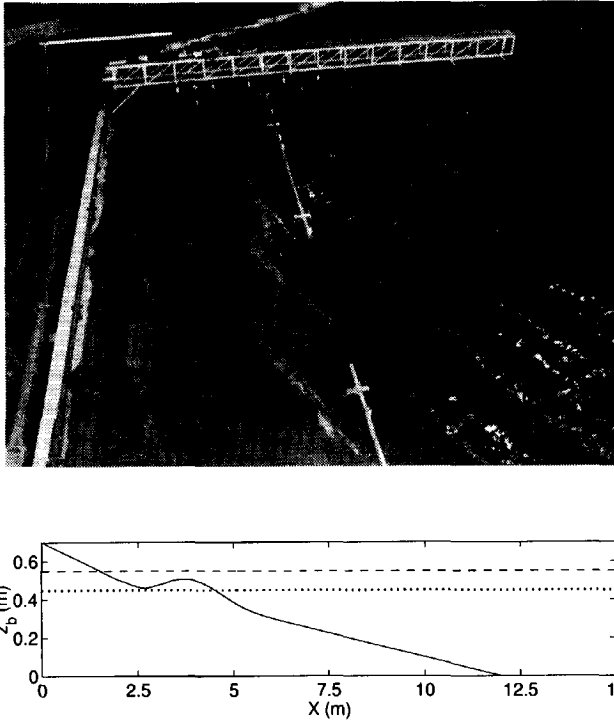


**Figure 2.2:** Upper panel: Instruments attached to the mobile carriage during the experiments. Lower panel: Bottom profile used throughout the experiments with mean water level for barred (dashed) and non-barred (dotted) beach profiles.

mean water level, with a linear response up to 20 cm with an accuracy in the mean water level of  $O(1)$  mm. It was possible to move the carriage along the beach during a test to measure the current velocity and wave height in any transect between the wave guides. The position of the various instruments is given in Table 2.2. The total arrangement resulted in a flexible measurement set-up with a high resolution across the beach.

## 2.5 Recirculation

The flow at a given transect is a combination of the pumped discharge and the wave-driven recirculation in the basin. Visser (1980,1991) showed that a



EMF	01	02	03	04	05	06	07	08		
$x(m)$	2.00	2.50	3.00	4.00	5.00	5.50	6.00	7.00		
WHM	01	02	03	04	05	06	07	08	09	10
$x(m)$	1.75	2.25	2.75	3.50	4.00	5.25	6.50	8.0	9.0	11.0

**Table 2.2:** Distance of electromagnetic current velocity meters (EMF) and wave height meters (WHM) from the beach.

minimum recirculation in the basin corresponds to an alongshore uniform wave driven current. His argument is as follows.

The recirculation is, in theory, zero when the pumped discharge is equal to the discharge forced by the waves. However, due to lateral mixing, a small recirculation remains. If the pumped discharge is too small, part of the wave driven flow is forced to recirculate in the basin. In case the pumped discharge is too large, this also results in a recirculation due to convection and lateral friction.

For each test condition (Table 2.1), the following had to be established to obtain an alongshore uniform current:

- width of the outflow opening
- the optimal pumped discharge corresponding to a wave driven current only
- redistribution of the pumped discharge at the inflow opening

If the width of the outflow opening was too large, a double recirculation cell would occur in the case of a barred beach, irrespective of the fact whether the pumped discharge matched the wave-driven discharge or not. To avoid this, the wave guide would be extended just into the surfzone, forcing the excess flow in the main basin to deeper water near the outflow opening, resulting in a single recirculation cell. Further decreasing the width causes the flow to contract towards the downstream end of the basin, thereby decreasing the length over which the flow is uniform.

Once the width of the outflow opening was established, the uniformity of the longshore current was verified by a visual check of the recirculation in the basin, using dye or floaters, in combination with the measured cross-shore distribution of the longshore current velocity in four transects along the beach. Velocities were measured for 5 minutes in each transect (increasing the sample time beyond this value proved to give negligible differences in the measured mean, both for monochromatic and random waves).

In the case where the pumped discharge was not near the optimal discharge, a strong offshore directed flow would occur along the wave guide at the downstream end of the basin. This could easily be observed using the floaters and/or dye.

The velocity measurements would show whether or not the distribution of the pumped discharge at the inflow opening had to be adapted. After each change in the basin configuration, the wave and current field were allowed to adapt for half an hour, after which the velocity field was measured again to check uniformity.

The preliminary data analysis was almost real time, so results could be checked immediately after the measurements had been performed, resulting in an efficient process to establish alongshore uniform currents.

## 2.6 Barred beach conditions

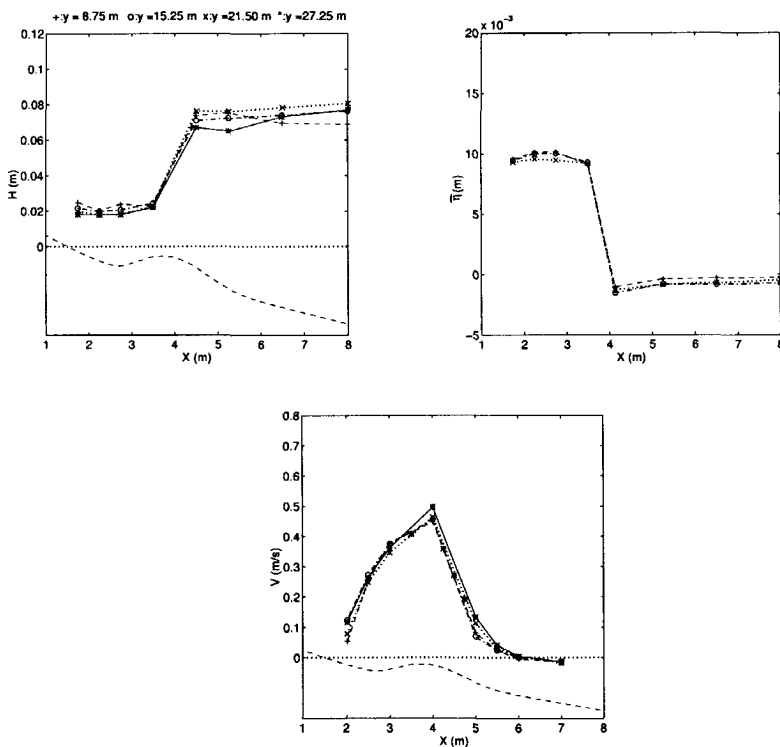


**Figure 2.3:** Measurements test SA243. Upper left panel: Wave height distribution. Upper right panel: Set-up of mean water level. Lower panel: Longshore current velocity profile.

The results for test SA243, which will be considered as the base case in the following, with regular obliquely incident waves of 8 cm height and 1 second wave period, are shown in Figure 2.3. For presentation purposes the results obtained from the first wave gauge offshore are not shown.

Most wave breaking occurred on the offshore side and on top of the bar (see also Figure 2.4), followed by a non-breaking area in the trough and then some additional breaking near the water line. The breaking occurs in a narrow strip of about two wave lengths, in which the wave height shows a steep decline. The wave height transformation is shown at four transects at various positions with respect to the inflow denoted by  $y$ , demonstrating that the wave field is approximately uniform along the basin.

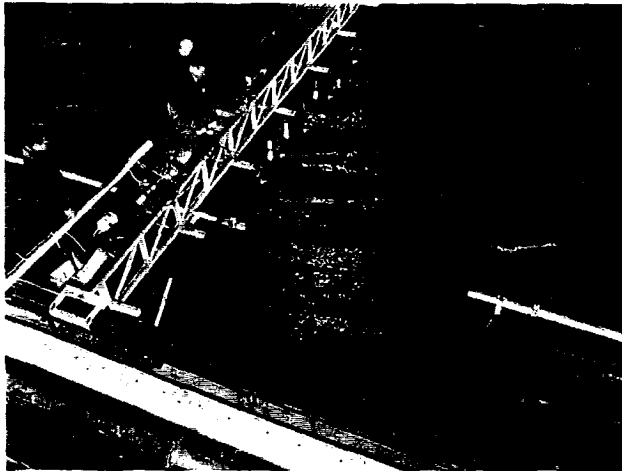


**Figure 2.4:** Dispersion of dye for test SA243 showing a bimodal longshore current velocity structure. (Dye experiment performed by Pieter Pasterkamp, Piet Rorije and the author all present on the mobile carriage.)

The longshore current velocities show nearly uniform distributions along the beach. The pumped discharge for this specific test was 65 l/s. The width of the breaker zone is seen to be narrow compared with the width of the measured current profile. However, lateral mixing drives the current outside the area of wave forcing, causing the current profile to become smoother.

The longshore current velocity has a clear maximum near the bar crest, though the measuring grid in the cross-shore direction is not dense enough to determine the exact position of the maximum. Part of the experiment was to examine the cross-shore structure of the shear instabilities (see Chapter 6). These

measurements were performed with an alongshore array of twelve EMF's. The position of the alongshore array was varied with respect to the shore line. For test SA243 one EMF in the alongshore array coincided with the fourth measuring transect, resulting in additional measurements of the longshore current velocity. These are also shown in Figure 2.3, indicating that the maximum longshore current velocity is indeed near the bar crest.

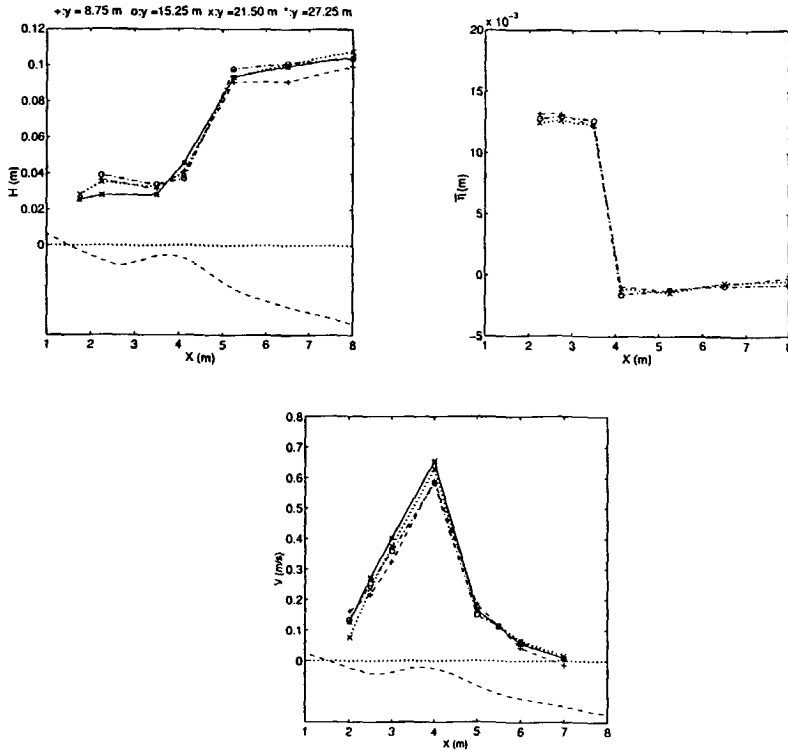


Figure 2.5: Measurements test SA337. Upper left panel: Wave height distribution. Upper right panel: Set-up of mean water level. Lower panel: Longshore current velocity profile

The current velocity close to the shoreline cannot be measured directly with the EMF's due to the limited water depth. The EMF's require a minimum submergence of about 1 cm and should not be closer to the bottom than 2 cm. This means that it is not possible to measure velocities at water depths smaller than

3 cm. To obtain qualitative information on the current velocity profile at small depths, i.e. near the shoreline, dye was used. The dispersion of dye for test SA243 is shown in Figure 2.4. The dye was inserted from the measurement carriage across the surfzone starting at the shore line with the picture taken shortly after. It clearly shows the high alongshore velocities on top of the bar (note the breaker line) and small velocities in the trough. In addition we can see a second maximum in the longshore current profile near the water line. These observations lend support to the theory that in case of predominantly wave driven currents the maximum velocities are where wave breaking occurs, i.e. near the bar crest and near the water line, resulting in a bimodal longshore current velocity profile.

The results for an increased wave height (10 cm), test SA337, are shown in Figure 2.5. The wave period is kept at 1 second. The wave field is again shown to be approximately uniform with maximum differences in wave height offshore in the order of 10%. The set-up of the mean water level is increased, but the alongshore differences in the set-up are still negligible. Due to the increased wave height, wave breaking starts further offshore, resulting in a slightly broader current velocity profile (compare Figures 2.3 and 2.5). The wave height in the trough is about 50 % larger than in the previous case due to the increased set-up level. The 25 % increase in incident wave height results in a 25 % increase of the maximum measured longshore current velocity on top of the bar (Figure 2.5) and in a 40 % increase in the wave driven longshore current mass flux, corresponding to a pumped discharge of 90 l/s.

The results for test SA432,  $H = 12.0$  cm and  $T = 1.1$  s, are shown in Figure 2.6. The variation of wave height along the beach at the sea-side of the bar is significant if compared to the base case. Especially near the inflow opening there are some unexpected variations in wave height. We expect this to be due to the interaction of the incident waves with the current velocity field, which is stronger and more inhomogeneous in this case. The inhomogeneity is apparent from the measured cross-shore distributions of the longshore current velocities, where the current in the first transect clearly has a different velocity profile than in the other transects, indicating that the cross-shore distribution of the pumped inflow discharge is not correct. The redistribution of the longshore current then causes flows in the cross-shore direction, which interact with the incident waves. Once the waves start breaking, alongshore variability decreases, resulting in a uniform wave field over most of the bar and trough.

The alongshore gradients in the set-up over the trough are small, with an increased maximum set-up level due to the higher incident wave energy. Over the bar crest larger differences in set-up are apparent, though part of that can be explained by the strong gradients occurring there, for which the present me-

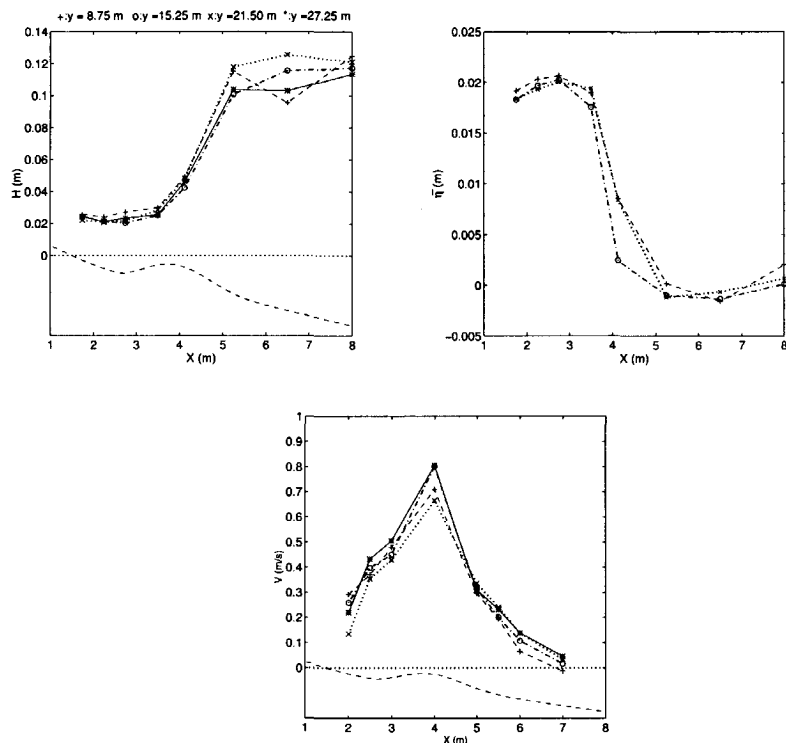


**Figure 2.6:** Measurements test SA432. Upper left panel: Wave height distribution. Upper right panel: Set-up of mean water level. Lower panel: Longshore current velocity profile

asurement resolution may be inadequate.

In Figure 2.6 it is shown that the longshore current at the seaward side of the bar is gradually increasing alongshore. This is most likely due to a mismatch at the inflow redistribution. The maximum current velocity over the bar crest reaches approximately 0.8 m/s. Differences in the longshore current velocity occur throughout the surfzone. The pumped discharge has been increased to 150 l/s to match the wave-driven flow.

The results for the maximum wave condition, test SA635 with  $H = 13.5$  cm and  $T = 1.1$  s, are shown in Figure 2.7. During this test the offshore wave field is strongly varying, with maximum differences occurring in the transect near the

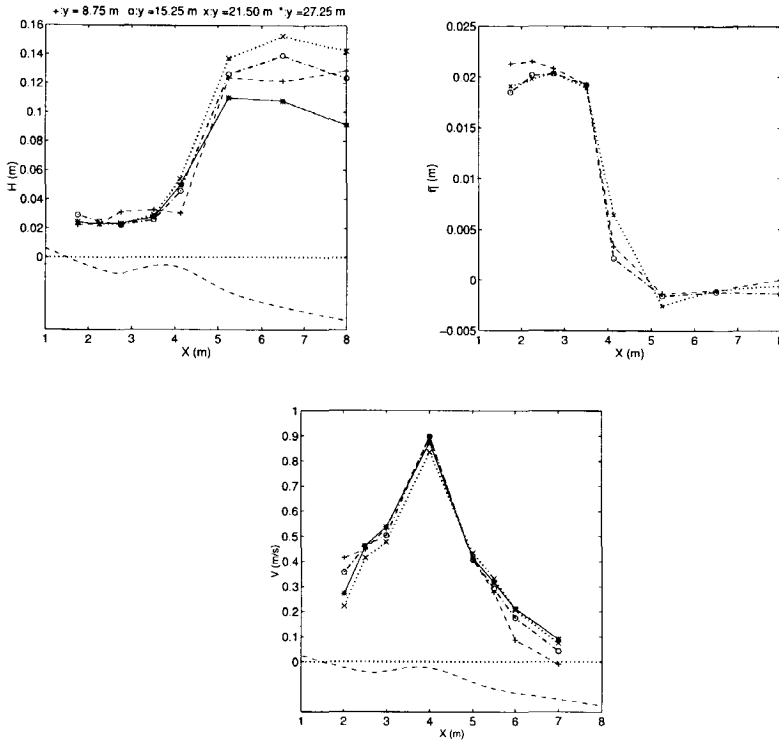


**Figure 2.7:** Measurements test SA635. Upper left panel: Wave height distribution. Upper right panel: Set-up of mean water level. Lower panel: Longshore current velocity profile

outflow. Most likely this is related to the relatively strong longshore current, with velocities up to 0.9 m/s. From visual observations it was apparent that reflections occurred as the current entered the deeper downstream basin (see Figure 2.1) following the outflow opening, thereby affecting the wave field. Contrary to the wave field, the set-up of the mean water level is reasonably uniform alongshore. Similar to the previous case an alongshore increasing current velocity is observed offshore. In this test the maximum pumped discharge of 200 l/s had been reached.

Figure 2.8 shows results for test SA537, with a wave height of 8 cm and a period of 2 seconds. The wave field is again less uniform in this case compared to the

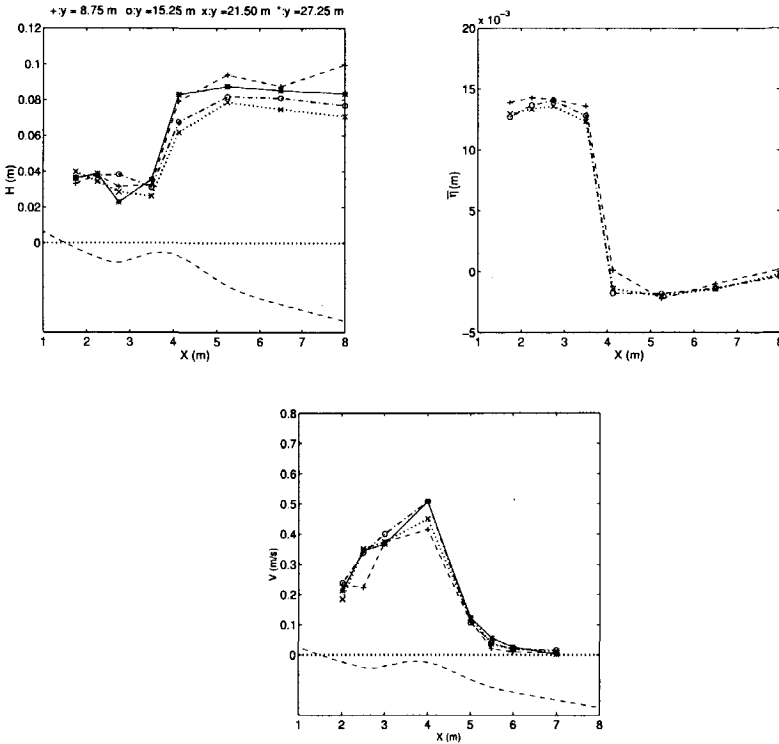


**Figure 2.8:** Measurements test SA537. Upper left panel: Wave height distribution. Upper right panel: Set-up of mean water level. Lower panel: Longshore current velocity profile

base case. The comparison with test SA243 shows that for test SA537 the wave height in the trough is higher, again due to the increased set-up level (compare Figures 2.3 and 2.8). The results for the current velocity show that increasing the wave period at constant wave height causes the longshore current velocity inshore of the bar to increase, indicating that the region of wave-forcing is extended further away from the bar crest, though the wave height transformation is similar in both cases. Offshore the current velocity profiles are similar.

The results in the case of random waves, test SO014, are shown in Figure 2.9. The wave field again is approximately homogeneous. The width of the breaker-zone is now in the order of three wavelengths. The difference in maximum set-up



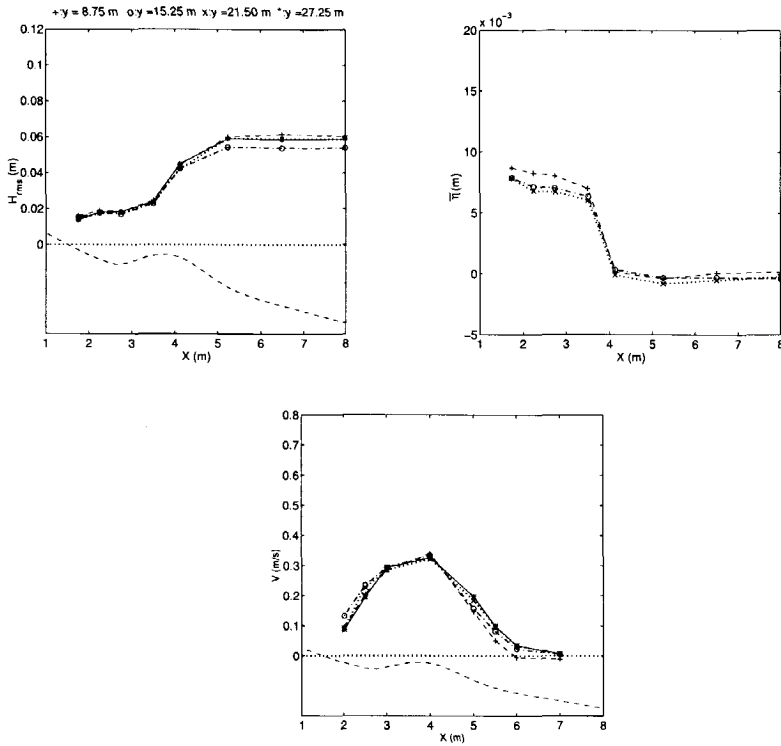


**Figure 2.9:** Measurements test SO014. Upper left panel: Wave height distribution. Upper right panel: Set-up of mean water level. Lower panel: Longshore current velocity profile

between the transect near the inflow opening and further downstream has increased but is still small ( $O(10^{-3})$ ) m. The longshore current velocity profile is smoother than in the monochromatic wave cases (compare Figures 2.3 and 2.9), as is to be expected due to the varying wave height and corresponding position of wave breaking, i.e. the forcing of the longshore current is spread over a broader area. The maximum longshore current velocity is less than in both previous cases, whereas offshore, the longshore current velocity is larger. Still, the maximum current velocity is on top of the bar and clearly not in the trough.

## 2.7 Non-barred beach conditions

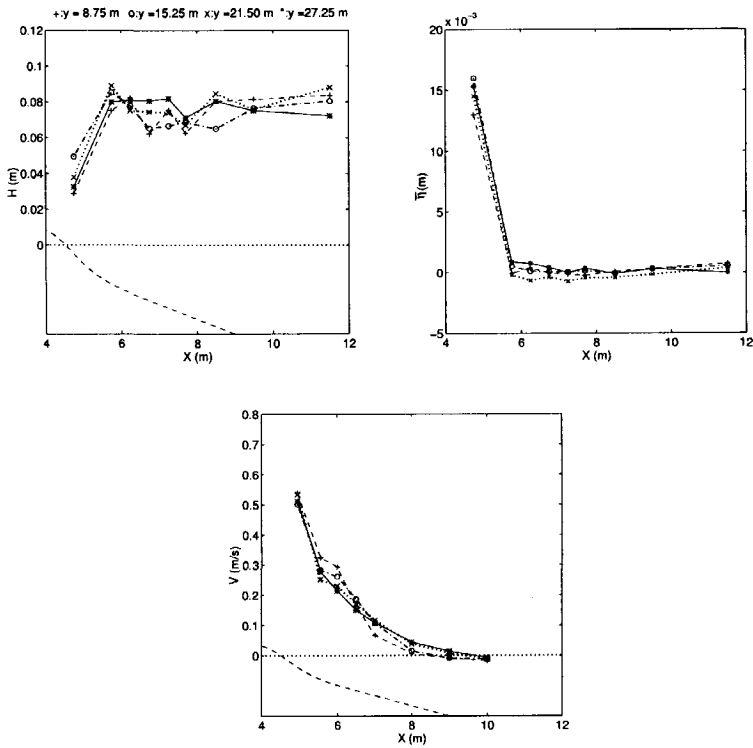


**Figure 2.10:** Measurements test SC219. Upper left panel: Wave height distribution. Upper right panel: Set-up of mean water level. Lower panel: Longshore current velocity profile

The results in the case of a non-barred beach, test SC219, are shown in Figure 2.10. Wave breaking occurs in a narrow strip close to the shoreline, which is confirmed by the measured set-up, starting at or beyond the next to last measuring point. The wave field is less uniform compared with most of the previous cases.

It proved to be difficult to obtain a uniform longshore current in case of a non-barred beach. The longshore current profile in the first two transects shows that the distribution of the pumped discharge at the inflow opening was not optimal. Further downstream the longshore current becomes more homogeneous.

The maximum current velocity occurs close to the shoreline at a depth smaller than the minimum measuring depth for the EMF. It is apparent from the measurements that there is strong lateral mixing which drives the current outside the surfzone.

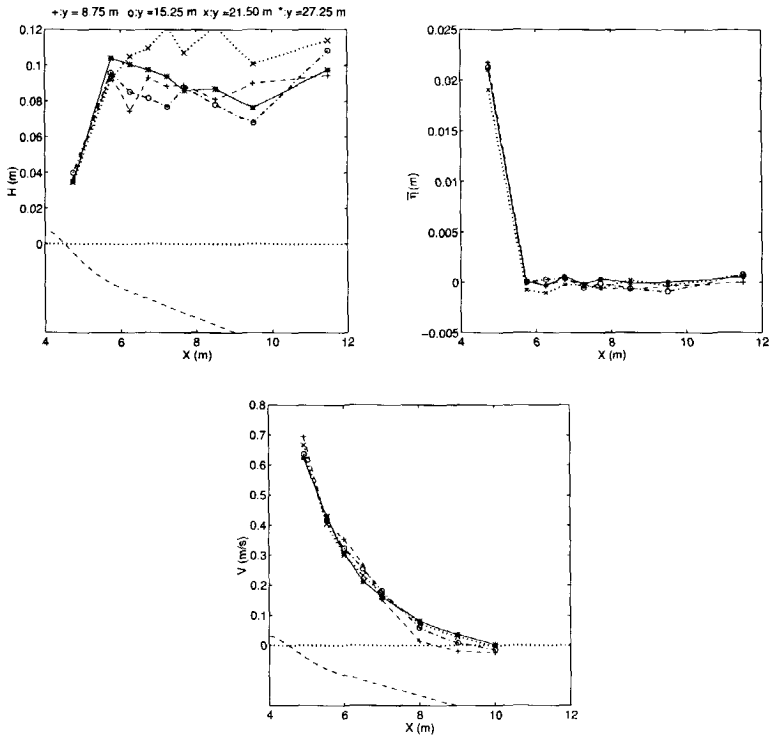


**Figure 2.11:** Measurements test SC315. Upper left panel: Wave height distribution. Upper right panel: Set-up of mean water level. Lower panel: Longshore current velocity profile

Similar results were obtained for test SC315, see Figure 2.11, where the wave height has been increased to 10 cm. The spatial variability of the wave field has increased further. Wave breaking still occurs in a narrow strip near the shoreline, which is not covered by the spatial resolution of the wave gauges. The maximum longshore current velocity has increased  $O(20\%)$  with respect to the previous case. The mismatch of current velocities at the inflow has increased accordingly.

## 2.8 Conclusions

The results for the measured set-up show that the alongshore variation in set-up in most of the cases were small, indicating that the measured current velocity profiles correspond to purely wave-driven currents.

In the case of forcing by monochromatic waves on a barred beach, the maximum of the longshore current velocity was clearly near the bar crest, coinciding with the location where waves are breaking. The dye experiment showed that in this case a second maximum in the longshore current velocity occurred near the shoreline, where the remaining wave energy was dissipated after propagating over the bar. The longshore current velocity in the trough increased if the wave period or the wave height were increased, indicating that the wave forcing was extended toward the shore.

In the case of random waves on a barred beach, the longshore current velocity profile became smoother, but the maximum longshore current velocity was still near the bar crest and clearly not in the trough.

Based on the above we conclude that the maximum longshore current velocities occur where breaking is most intense, i.e. on the bar and near the shoreline. Lateral mixing smoothes the current profile, but does not significantly affect the position of the maximum current velocity, which in the case of a barred beach clearly remains near the crest. This holds for the cases of short waves (test SA243), long waves (test SA537) and random waves (test SO014) on barred beaches.

For monochromatic waves on a plane beach the maximum alongshore current velocity occurred very close to the water line, at a depth smaller than the minimum depth for instrument deployment. Strong mixing caused the velocity profile to smooth out, becoming of comparable width as the current velocity profiles in the case of a barred beach.

# Chapter 3

## Laboratory Experiment: Dynamic flow properties

### 3.1 Introduction

In the following the results for the dynamic flow properties obtained from the various tests are presented and discussed. Prior to that a description is given of the spectral analysis procedures used in the analysis. The data on the alongshore development of the flow dynamics was obtained from two identical longshore arrays. Each array deployed six current meters, shown in Figure 2.1, to measure the development of the shear instabilities along the beach. The current velocity meters were set at 1/3 of the water depth from the bottom to obtain a measure of the depth-averaged velocity. They were attached to four beams each of 6 metres long, supported by thin poles at either end of the beam to avoid a vast number of poles to support the individual EMF's. The total number of lags is determined by the number of instruments and their position with respect to each other (e.g. Huntley et al., 1984). The distance of the EMF's from the inflow-opening,  $y$ , is given in Table 3.1.

EMF	01	02	03	04	05	06
$Y(m)$	3.75	8.75	9.75	11.25	11.75	15.25
EMF	07	08	09	10	11	12
$Y(m)$	19.75	24.75	25.75	27.25	27.75	31.25

**Table 3.1:** Distance of electromagnetic current velocity meters (EMF) from the inflow opening

Detailed measurements of the cross-shore structure for Test SA243 were obtained by repositioning these alongshore arrays perpendicular to the beach. In

doing so the vertical position of the current velocity meters would be changed to keep a representative measurement of the depth-averaged velocity based on a logarithmic vertical velocity profile. During the repositioning the input wave and flow conditions were maintained. Measurements would restart after the disturbances induced by the repositioning of the instruments had disappeared (estimated duration less than half an hour). Note that instruments could not be positioned at the bar crest given the strong wave breaking induced turbulence.

Spectral analysis is performed both in the frequency and combined frequency-longshore wavenumber domain. The first shows how much energy is present in a specific frequency bandwidth. This does not imply that the observed energy in the low-frequency bandwidths is due to the presence of shear instabilities. It could also be due to basin-related long wave resonance. Given the fact that the phase speed of shear instabilities is much lower than the phase speed associated with (infra-)gravity waves, the spectral analysis in the wave-number domain will show whether the observed wave energy is due to the presence of shear instabilities. The frequency-wavenumber spectral analysis is based on the Maximum Entropy Method (Burg, 1967). The length of each array was 11.5 metres, allowing estimates of the frequency ( $f$ )-longshore wavenumber ( $k_y$ ) spectrum over the upstream half and the downstream half of the beach.

Parts of this chapter have been published in Reniers et al. [1994] and Reniers et al. [1997].

## 3.2 Spectral Analysis

The velocity timeseries were sampled with a frequency of 25 Hz over a half hour period. The analysis in the frequency domain is performed with FFT-transforms. For that purpose the timeseries are divided into a number of half-overlapping subseries for which the spectral components are computed. By averaging over the subseries stable spectral estimates can be obtained.

The frequency-longshore wavenumber spectrum is given by:

$$S(f, k_y) = \int \phi(r, f) e^{(-ik_y r)} dr \quad (3.1)$$

where:

$f$  = wave frequency

$k_y$  = longshore wave number

$\phi$  = spatially lagged frequency cross-spectrum

$r$  = spatial lag

To compute the cross-spectral values for two velocity time series at a given alongshore spatial lag, their signals represented by  $x$  and  $y$ , are composed in the following way:

$$z(t) = x(t) + iy(t) \quad (3.2)$$

In discrete form their Fourier-transform is given by:

$$Z_k = \sum_{n=0}^{N-1} (z_n) \exp(-2\pi \frac{kn}{N}) \quad (3.3)$$

where  $z_n = z(t_n)$  and  $t_n$  equals  $n$  times the constant time interval  $\Delta t$ . The Fourier coefficients for  $x$  and  $y$  can now be written as:

$$X_k = X_{1,k} + iX_{2,k} = \frac{Z_k + Z_{N-k}}{2} \quad (3.4)$$

$$Y_k = Y_{1,k} + iY_{2,k} = \frac{Z_k - Z_{N-k}}{2} \quad (3.5)$$

where  $X_{i,k}$  and  $Y_{i,k}$  are real. Next the cross-spectral values are obtained from:

$$\phi = X_k Y_k^* = (X_{1,k} Y_{1,k} + X_{2,k} Y_{2,k}) - i(X_{1,k} Y_{2,k} + X_{2,k} Y_{1,k}) \quad (3.6)$$

where the co-and quad values are given by the real and imaginary parts of the cross-spectrum respectively. Again averaging over half-overlapping subseries, stable estimates of the co-and quad spectral values are obtained. This procedure is performed for each discrete spatial lag  $r_j$ .

Due to the limited number of spatial lags, FFT methods cannot be used to perform the transformation expressed by eq. 3.1. To obtain the spectral estimate we have resorted to the Maximum Entropy Method (Burg, 1967), which essentially fits a polynomial to the cross-spectral values for each fixed frequency and at each spatial lag:

$$\sum_{j=-N}^{j=N} \phi(r_j, f) \exp(-ir_j k_y) = \frac{a_0(f)}{|1 + \sum_{j=1}^N a_j(f) \exp(-ir_j k_y)|^2} \quad (3.7)$$

This results in a linear set of equations between the cross-spectral values,  $\phi(r_j, f)$  and the coefficients  $a_n(f)$ , which can be solved efficiently (Burg, 1968) if the cross-spectral values are given at equidistant intervals. This is not the case (see Table 2.2), so we have to use a different solution method which does not depend on the spatial lags,  $r_j$ , being uniform.

Therefore the problem is restated in the following way. The entropy associated with wave-number space can be expressed as (dropping  $f$ )

$$\mathcal{E} = -\frac{1}{2\pi} \int \ln(S(k_y)) dk_y \quad (3.8)$$

We want to maximise the entropy  $\mathcal{E}$  subject to the constraint

$$h_j(S) \equiv \frac{1}{2\pi} \int S(k_y) \exp(ik_y r_j) dk_y - \phi_j = 0 \quad (3.9)$$

for all  $j$ , where  $\phi_j$  is the cross-spectral density at lag  $r_j$ . Using (3.9) we maximise the function  $f$  defined by

$$f = \frac{1}{2\pi} \int [-\ln(S(k_y)) + \sum_j \mu_j S(k_y) \exp(ik_y r_j)] dk_y - \sum_j \mu_j \phi_j \quad (3.10)$$

in which  $\mu_j$  are Lagrangian multipliers. The derivative to  $S(k_y)$  is

$$\frac{df}{dS} = \frac{1}{2\pi} \int \left[ \frac{-1}{S(k_y)} + \sum_j \mu_j \exp(ik_y r_j) \right] dk_y = 0 \quad (3.11)$$

so that

$$S(k_y) = \frac{1}{\sum_j \mu_j \exp(ik_y r_j)} \quad (3.12)$$

Introducing this into eq. 3.10 for the cost-function:

$$q = \frac{1}{2\pi} \int_{-k_{y,max}}^{k_{y,max}} [1 + \ln(\sum_j \mu_j \exp(ik_y r_j))] dk_y - \sum_j \mu_j \phi_j \quad (3.13)$$

which is to be maximised as a function of the Lagrangian multipliers  $\mu_j$ . The maximisation of  $q$  is performed with the BFGS method (Dennis and Snelb, 1983) using the gradient of  $q$  with respect to  $\mu_l$ :

$$q'(\mu_l) = \frac{1}{2\pi} \int_{-k_{y,max}}^{k_{y,max}} \frac{\exp(ik_y r_l)}{\sum_j \mu_j \exp(ik_y r_j)} dk_y - \phi_l \quad (3.14)$$

Recognising the Fourier transform, the gradient can be obtained for all available values of the lags  $r_l$ , where  $k_{y,max}$  is the Nyquist wave number. Using the cross-spectral density at discrete intervals,  $\phi_j$ , as input, the Lagrangian multipliers  $\mu_j$  can be obtained and the spectrum reconstructed from eq. 3.12.

To test the performance of the two methods described above, a covariance function is generated in the following way:

$$\text{Re}(\phi_j) = (0.25 \cos(0.5 r_j) + 0.05 \cos(r_j)) \exp(-r_j/100) \quad (3.15)$$

$$\text{Im}(\phi_j) = (0.25 \sin(0.5 r_j) + 0.05 \sin(r_j)) \exp(-r_j/100) \quad (3.16)$$



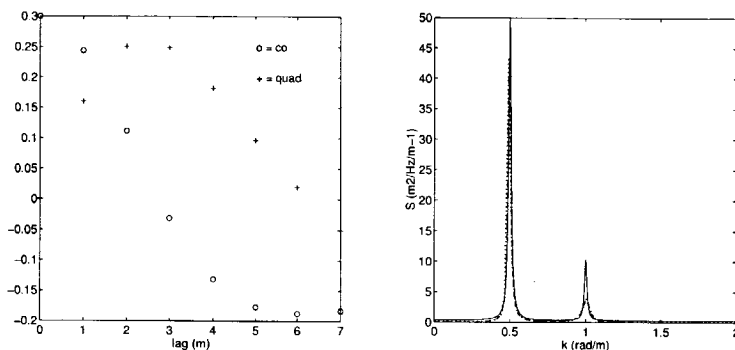


**Figure 3.1:** Left panel: Co- and quad values,  $\phi(r)$ , used in spectral estimates expressed in  $\text{m}^2/\text{Hz}$ . The values at lags 4 and 6 have been omitted in the case Lagrangian multipliers are used. Right panel: Spectral estimates based on eq. 3.7 (dashed) and using Lagrangian multipliers (dotted) eq. 3.12 vs. target spectrum (solid)

The corresponding spectrum is obtained with the Fourier Transform of the covariance function for a large number of lags. To obtain the MEM-spectral estimates, only the first seven lags have been used. The corresponding co- and quad values,  $\phi(j)$  for these lags are shown in Figure 3.1. The two spectral estimates are also shown in Figure 3.1. The first is obtained with the MEM for equidistant data (Burg, 1967). The second estimate is obtained using Lagrangian multipliers where co- and quad values at lags 4 and 6 have been omitted to create a non-equidistant distribution. Both spectral estimates compare favourably with the real spectrum, showing sharp spectral features at the correct wave numbers. The energy present in the second harmonic is somewhat underpredicted in both cases.

### 3.3 Results

#### 3.3.1 Frequency Domain

To check on the shear instabilities, a spectral analysis in the frequency domain has been made of all time series obtained with the current velocity meters in the longshore array for the longshore velocity. For brevity, attention is focussed on the results obtained for test SA243. Similar results were obtained for other tests.

The result of the spectral analysis for the longshore velocity in the frequency

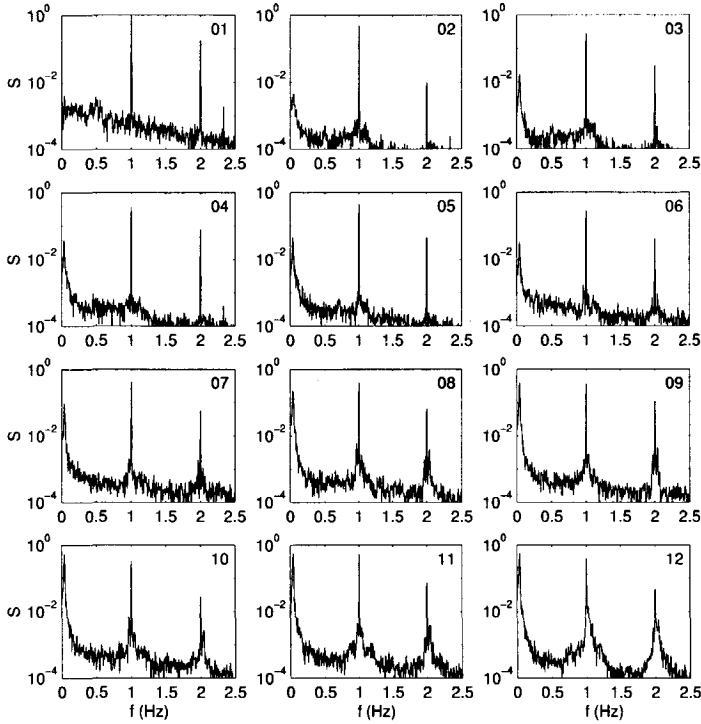


**Figure 3.2:** Alongshore velocity spectra obtained from EMF 01 in the upper left hand corner to EMF 12 in the lower right hand corner, showing the energy density,  $S$ , in  $(m/s)^2/Hz$  as function of frequency in Hz for test SA243

domain is shown in Figure 3.2. EMF 01 shows the spectral density at 3.75 m from the inflow opening. There are two distinct peaks present, due to the primary wave at 1.0 Hz and the bound superharmonic at 2.0 Hz. The noise which is apparent in the plots is ascribed to turbulence caused by the inflow at the beginning of the beach. This interpretation is supported by the fact that the energy density at most of these frequencies is dampened as the current flows along the beach toward EMF's 02 and 03 at 8.75 m and 9.75 m from the inflow opening respectively.

The most striking feature in the spectra is the strong increase in spectral density at low frequencies. This spectral density increase continues as we move along the beach toward the outflow opening, apparently reaching an equilibrium

near EMF 11, from where the spectral density no longer seems to increase. It is interesting to see that the sidebands at the primary and secondary wave frequencies are increasing in magnitude in the downstream direction, suggesting an interaction with the low frequency features.

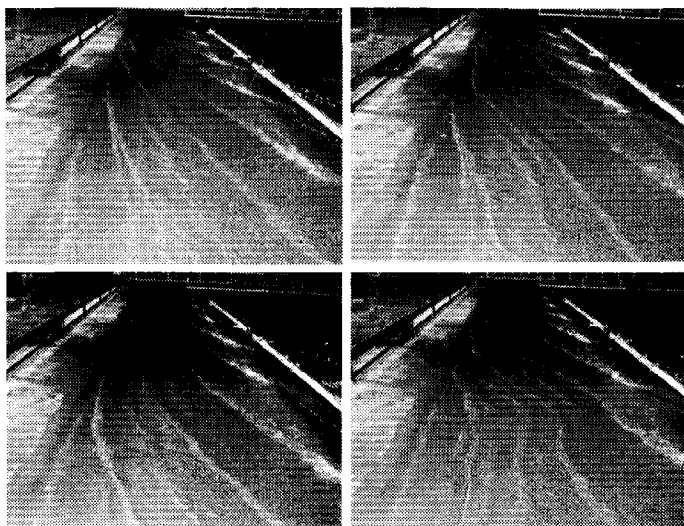


**Figure 3.3:** Snap shots with an interval of approximately 4 seconds (starting in the upper left corner going from left to right) of the experimental set-up and wave field during test SA243.

This interaction is also apparent in a sequence of photographs of the wave field during test SA243 (see Figure 3.3). Starting at the upper left panel we see that after passing the bar crest waves stop breaking in the trough and propagate further toward the shoreline, showing curved wave crests due to bottom refraction. Given the decreasing depth from trough to water line a curvature is expected convex to the shore, which is indeed apparent in the upper left panel of Figure 3.3. A few seconds later a local disturbance is present showing concave instead of convex wave crests (see upper right panel of Figure 3.3), where current refraction due to the presence of the disturbance must take precedence over bottom refraction. Further in time this oscillation propagates downstream thereby increasing in magnitude, displaying an increased interaction with the incident wave crests.

A closer look at the alongshore development of the spectral density in the low-frequency part of the spectrum is shown in Figure 3.4. This shows that a

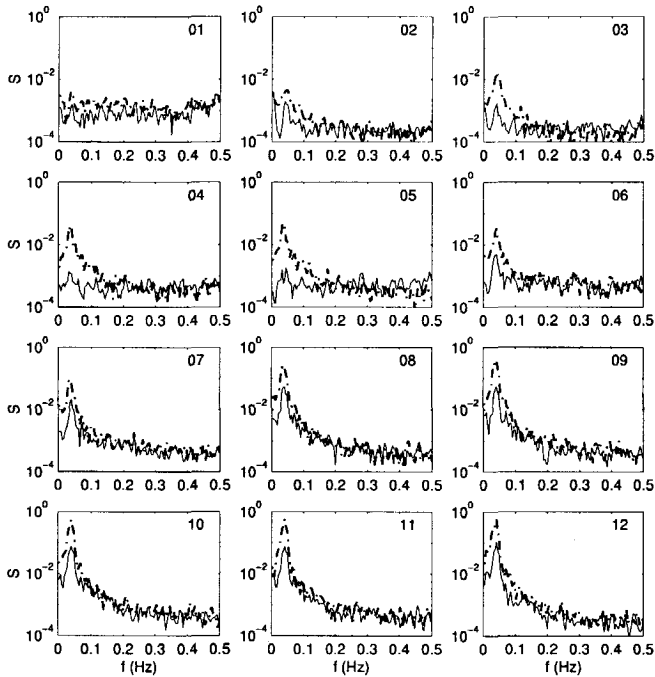


**Figure 3.4:** Low-frequency alongshore (dash-dotted) and cross-shore (solid) velocity spectra obtained from EMF 01 in the upper left hand corner to EMF 12 in the lower right hand corner, showing the energy density,  $S$ , in  $(\text{m/s})^2/\text{Hz}$  as function of frequency in Hz for test SA243

distinct peak occurs at .04 Hz.

Similar results to those presented above for the alongshore velocities have been obtained for the cross-shore velocities which are also shown in Figure 3.4. A notable difference is the delayed pickup of the energy density in the low-frequency part of the spectrum, which now starts approximately halfway down the basin. Also the final intensity measured at the downstream end is smaller than obtained for the longshore velocities. This most likely corresponds to the cross-shore structure of the observed oscillations, i.e. depending on the cross-shore position of the alongshore arrays the  $u$  or  $v$  velocity component may dominate.

In the following, we give evidence that the low-frequency energy density is associated with shear instabilities.

### 3.3.2 Wavenumber Domain

Cross-spectral analysis of the alongshore velocity is performed for the upstream and the downstream part of the beach separately, for EMF's 03 to 06 and EMF's 07 to 12 of the two arrays respectively.

The strong growth of the low-frequency oscillations in the upstream part of the beach affects the cross-spectral values. For this reason EMF's 01 and 02 have been left out of the cross-spectral analysis.

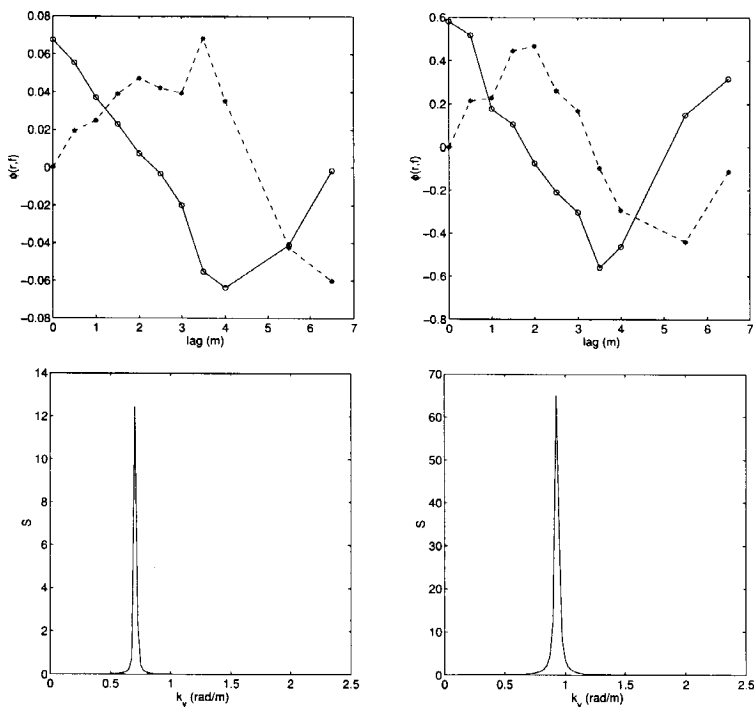


**Figure 3.5:** Upper panels:  $Co$  (drawn) and  $quad$  (dashed) values in  $(m/s)^2/(Hz)$  of alongshore velocity at the downstream array for  $f = 0.0244$  Hz (left) and  $0.0407$  Hz (right) for test SA243. Lower panels: Corresponding wave number spectra in  $(m/s)^2/(m^{-1} Hz)$ .

Typical results obtained with cross-spectral analysis for the downstream array are shown in Figure 3.5 for two frequencies,  $f = 0.0244$  Hz and  $f = 0.0407$  Hz. The  $co$ - and  $quad$ -values values are somewhat erratic, due to the non-stationarity

of the velocity field. Still, the sequence of co-and quad-values clearly indicates that there are progressive waves present.

The  $k_y$ -spectral estimates at these two frequencies are also shown in Figure 3.5. The results indicate a dominant wavelength of 9 m for the first frequency bandwidth and 6.8 m for the second. These wavelengths are much shorter than expected for gravity waves of this frequency.

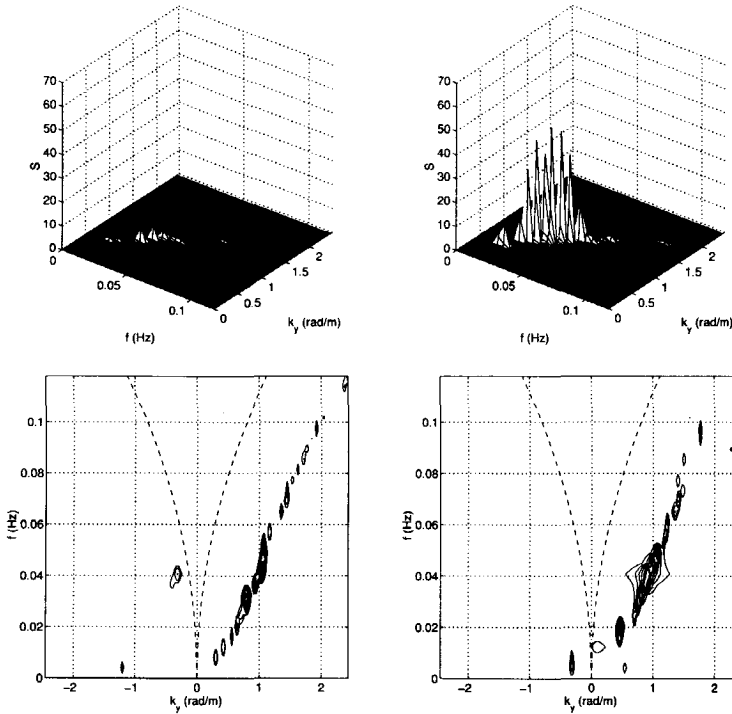


**Figure 3.6:** Test SA243:  $f - k_y$ -spectrum for alongshore velocity obtained from the upstream (left panels) and downstream array (right panels) displayed as a surface plot (upper panels) and contourplot (lower panels) with contours at .1 .2 .5 1 2 5 10 20 50  $(\text{m/s})^2/(\text{m}^{-1}\text{Hz})$ . The zero-mode edge wave dispersion curves for a plane beach indicated by dashed lines.

Performing the same analysis for all frequency bands results in  $(f, k_y)$ -spectra, shown in Figure 3.6 for the upstream and the downstream arrays respectively. The results indicate an almost linear dispersion relation with a phase speed of

about 35 cm/s, which is roughly equal to the mean longshore current velocity. The area in between the zero-mode edge wave dispersion curves, see Figure 3.6, represents energy density associated with gravity waves. The observed energy density is clearly outside this domain. Therefore we conclude that the observed oscillations represent shear instabilities. Given the nearly constant phase speed for all frequencies the position with maximum energy density corresponds to the fastest growing temporal mode (denoted FGM in the following, see also Appendix A), which is frequently used in comparisons with computational results. In this case the FGM is located at an alongshore wave number of  $0.91 \text{ (m}^{-1}\text{)}$  with a corresponding frequency of 0.041 Hz.

Comparison of the spectral estimates for the upstream and the downstream array (compare left and right panels of Figure 3.6) again shows the strong increase in magnitude of the shear instabilities while propagating along the beach.

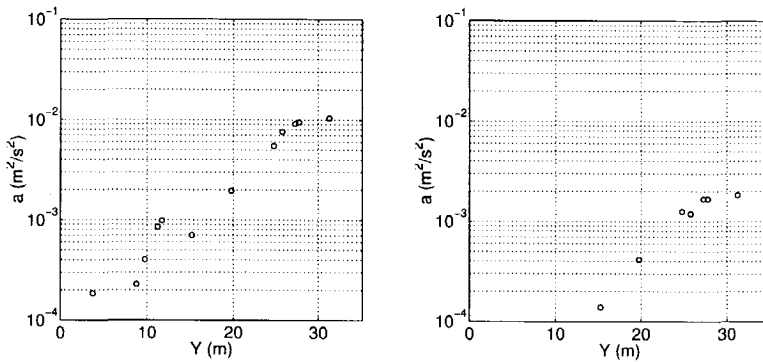


**Figure 3.7:** Alongshore growth of total variance in 0 to 0.1 Hz frequency band for alongshore velocities (left panel) and cross-shore velocities (right panel) during test SA243.

A semilogplot of the total variance in the frequency band from 0 to 0.1 Hz, denoted by  $a$ , as a function of the longshore coordinate is presented in Figure 3.7. This clearly shows an approximately exponential growth of this energy for both the alongshore and cross-shore velocities. The values at the most downstream stations may suggest a levelling off and an approach to equilibrium. Given the fact that the distance between these EMF's is small, and the scatter present in the measured growth of the instabilities, caution is required in concluding that an equilibrium is reached.

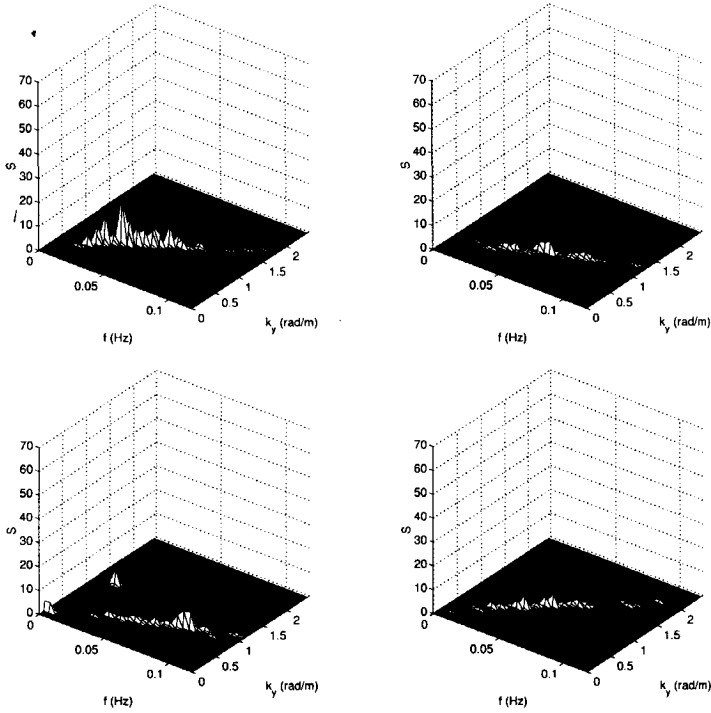


**Figure 3.8:**  $f - k_y$ -spectrum for alongshore velocity obtained from downstream array for Tests SA337 (left upper panel), SA432 (upper right), SA635 (lower left) and SA537 (lower right). Spectral energy density expressed in  $(m/s)^2/(m^{-1}Hz)$ .

Next we discuss the results of the additional tests. First a test where the incident wave height is increased (Test SA337,  $H_i = 10$  cm) with respect to the previous test (SA243,  $H_i = 8$  cm). The longshore current velocity distribution for increased wave height shows a stronger mean velocity shear (see Figure 2.5). As mentioned earlier, an increased backshear is expected to give a wider shear instability range. This is confirmed by comparing the results obtained for Tests SA243 and SA337 (compare Figures 3.6 and 3.8).

The measured dispersion relation for Test SA337 is again almost linear, though with an increased phase velocity with respect to Test SA243,  $c = O(45)$  cm/s vs.  $c = O(35)$  cm/s, in correspondence with the increased longshore current velocities. A stronger shear is also expected to lead to a larger growth rate,



whereas the intercomparison shows the energy density at the downstream end to be less. Part of this can be explained by the increased propagation speed of the shear instabilities, which results in less time to develop given the limited length of the basin. Furthermore, the damping due to the eddy viscosity increases with increasing wave height, reducing the growth rate. The shear instability intensity reached at the downstream end of the beach is a delicate balance of forcing, damping and propagation time; these aspects are discussed in Chapter 5.

The results for test SA432, where the incident wave height is further increased to  $H_i = 12$  cm, are also shown in Figure 3.8. Again there is a wide range of instabilities present. Note that as a result of the increased velocity shear, see Figure 2.6, the peak frequency corresponding to the fastest growing mode has increased to approximately 0.06 Hz (compared to 0.04 Hz for test SA243). The further increased longshore current velocity is again apparent in the measured phase velocity of the shear instabilities,  $c = O(65)$  cm/s. This increase results in a smaller intensity of the instabilities at the downstream end compared to the previous cases.

The results for the maximum wave condition, test SA635, with the highest longshore current velocity (see Figure 2.7), are also shown in Figure 3.8. There is some spurious energy at frequencies less than 0.02 Hz, followed by a linear dispersion of the energy density at higher frequencies. The peak frequency has increased further to approximately 0.08 Hz. The phase velocity has increased up to approximately 75 cm/s whereas the maximum longshore current velocity is approximately 90 cm/s (see Figure 2.7). The downstream shear instability intensity has decreased even further, being of  $O(10\%)$  of the results obtained for test SA243 (see also Figure 2.7).

In SA537, where the wave period has been increased to 2 seconds, the longshore current velocity values are of similar magnitude as test SA243, but have a different distribution (compare Figures 2.3 and 2.8). The back shear of test SA537 is only slightly weaker, still the measured shear instability intensity at the downstream end of the basin is significantly smaller (compare Figures 3.6 and 3.8). The latter cannot be explained by the phase velocity of the shear instabilities, which is of  $O(35)$  cm/s in both cases.

Finally a test is discussed where random waves (SO014) instead of regular waves (SA243) were used to generate the longshore current. This results in a smoother velocity profile and weaker backshear (Figure 2.9). The expected instability range is therefore narrower than in the base case. The  $f - k_y$ -spectrum for Test SO014, obtained at the downstream end of the basin, is shown in Figure 3.9.

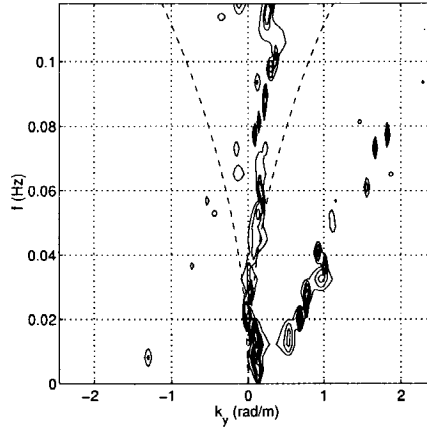


**Figure 3.9:**  $f - k_y$ -spectrum for alongshore velocity obtained from downstream array for Test SO014. Spectral energy density expressed in  $(\text{m/s})^2/(\text{m}^{-1}\text{Hz})$ . The zero-mode edge wave dispersion curves for a plane beach indicated by dashed lines.

The energy density concentrated along the zero alongshore wave number line corresponds to the low-frequency part of the incident infra-gravity waves. The energy density concentration outside the wave-number band associated with the incident waves is indeed narrow in frequency, ( $0.01\text{Hz} < f < 0.04\text{ Hz}$ ), with some energy at higher frequencies. This is clearly associated with the shear instabilities. The phase velocity is of  $O(30)$  cm/s, which is less than test SA243, corresponding to the decrease in the longshore current velocity.

For tests SC219 and SC315, with a planar profile, shear instabilities were not detected. This may seem surprising given the strong back shears that occur in the longshore current velocity profiles (see Figures 2.10 and 2.11). Still, as mentioned earlier, the position of the maximum longshore current with respect to the water line is an important parameter too, which is considerably smaller in the case of a planar beach profile. This will be examined further in Chapter 7.

The results for the various test are summarised in Table 3.2.

test	$c$ (cm/s)	$V_{max}$ (cm/s)	FGM: $k_y$ (rad/m)	FGM: $f$ (Hz)
SA243	35.0	50.0	0.91	0.041
SA337	45.0	65.0	0.75	0.035
SA432	65.0	80.0	0.70	0.060
SA635	75.0	90.0	0.86	0.082
SA537	35.0	50.0	0.81	0.040
SO014	30.0	35.0	0.81	0.028

**Table 3.2:** Summary of results obtained from the experiment.  $c$  : phase speed,  $V_{max}$ : maximum longshore current velocity, FGM:  $k_y$ : position FGM along the  $k_y$ -axis, FGM:  $f$ : similar but along the frequency axis.

### 3.4 Conclusions

The experiments clearly demonstrated the possibility of shear instabilities on a barred beach in a laboratory generated wave-driven longshore current. This followed from a successful analysis of the longshore current dynamics with a spectral analysis technique based on the Maximum Entropy Method (Burg, 1967) which has been extended in order to analyse the dispersion characteristics of the longshore current dynamics. The dispersion curves thus obtained were almost linear, with a phase speed of order of 70 % of the maximum longshore current velocity. Using the zero-mode edge-wave dispersion as a reference it was clear that the energy cannot be associated with gravity waves and therefore corresponded to shear instabilities.

Starting at the upstream end the shear instabilities show an exponential growth along the beach, possibly approaching an equilibrium near the outflow for Test SA243. Given a number of uncertainties caution is still required in concluding that an equilibrium is actually reached. The finite amplitude shear instabilities for the various tests differed considerably, indicating that the downstream conditions are a delicate balance of forcing, damping and propagation time. These matters will be investigated in Chapter 5 and 6 with help of non-linear numerical modelling.

In all cases the observed low-frequency energy corresponded to shear instabilities only, with the exception of Test SO014, where due to the randomness of the incident wave field, part of the low frequency energy corresponded to gravity waves.

The results showed that there is a significant influence of the beach profile on the occurrence of shear instabilities. They did occur on a barred beach but were not observed on a non-barred beach.



# Chapter 4

## Modelling of longshore currents

### 4.1 Introduction

Much research has been done to model the longshore current velocity accurately. Comparison of model results with both field (Thornton and Guza, 1986, Church and Thornton, 1993, among others) and laboratory data (Visser, 1984, Svendsen and Putrevu, 1994, among others) for wave-driven longshore currents on planar beaches show in general good agreement. However, there has been much discussion on the cross-shore distribution of the wave-driven alongshore current velocity on barred beaches (Church and Thornton, 1993, Smith et al., 1993). As mentioned in Chapter 1, the case where field measurements show a maximum longshore current velocity in the trough, as observed during the DELILAH field experiment (Birkemeier, 1991) at Duck, North Carolina, numerical model studies for alongshore uniform currents show that the maximum is near the bar crest with another maximum close to the shore line, corresponding to the locations where wave breaking occurs. Note that not all field measurements show a longshore current velocity distribution with a maximum in the trough (Whitford and Thornton, 1995).

In the above mentioned modelling of wave-driven longshore currents, alongshore uniformity in bathymetry and wave-and current fields is often assumed. This greatly simplifies the model equations to 2-D in the cross-shore. However, alongshore uniformity in its true sense is not generally expected to be met in the field, where small spatial alongshore variations in bedlevel and/or wave conditions are likely to be present. In the following we introduce a set of equations to model the wave-driven longshore current for a bathymetry which varies alongshore.

The objective of this chapter is to establish the cross-shore distribution of the longshore current velocity over a barred beach with respect to the areas of wave breaking and the potential presence of alongshore pressure gradients induced by

weak alongshore bed undulations. To that end a set of equations is introduced to model the wave-driven longshore current for a bathymetry which may vary alongshore. Existing state of the art model equations have been used; no attempt has been made to improve these formulations.

It is assumed that the breaking wave transformation can be modelled with the concept of surface rollers (Svendsen, 1984). The idea is that the organised wave energy which is released at breaking is first transferred to energy of a roller which rides on the wave front with the phase speed of the waves. The difference in velocity between the roller and the water particles at the wave front yields a shear stress between the roller and the underlying wave front. The work done by the shear stress equals the dissipation of roller energy. The time needed for the organised wave energy to dissipate through the roller causes a spatial lag between the location of wave breaking and the actual dissipation (Nairn et al., 1989).

Once the model equations have been introduced comparison between computational results and the previously described laboratory measurements is used to assess the effects of rollers, bottom friction and mixing on the cross-shore distribution of the longshore current velocity for a purely wave-driven flow. In the comparison with measurements attention is focussed on random waves because these are a better approximation of what happens in the field than periodic waves.

Next the longshore current profiles obtained during the DELILAH experiment (Birkemeier, 1991) at the US Army Corps of Engineers' Field Research Facility at Duck, North Carolina are examined. A comparison is made with measurements where the following cases are considered:

- weak alongshore variation
- strong alongshore variation
- alongshore uniformity

Intercomparison of the various cases yields additional information on the importance of alongshore non-uniformities and their consequences in modelling the longshore current.

Parts of this chapter have been published in Reniers, Thornton and Lippmann [1995], Lippmann, Thornton and Reniers [1995] and Reniers and Battjes [1997].

## 4.2 Modelling

### 4.2.1 Wave transformation

Considering a stationary wave field of obliquely incident random waves on a variable bathymetry, the wave transformation is modelled with a 2D-wave roller model. The balance for the wave energy,  $E_w$ , on a variable bathymetry is given by:

$$\frac{\partial E_w c_g \cos(\theta)}{\partial x} + \frac{\partial E_w c_g \sin(\theta)}{\partial y} = -D_w \quad (4.1)$$

where  $c_g$  represents the group velocity,  $D_w$  the wave energy dissipation,  $x$  the distance along the shore normal (positive onshore),  $y$  the distance alongshore (following the cartesian convention) and  $\theta$  the angle of incidence with respect the  $x$ -axis. The wave energy is defined along the up-wave boundaries. To model the wave energy dissipation due to wave breaking different formulations can be used (Battjes and Janssen, 1978, Thornton and Guza, 1983, Roelvink, 1993, among others). Introducing the dissipation model according to Battjes and Janssen (1978):

$$D_w = \alpha \frac{\rho g}{4T_p} H_{max}^2 Q_b \quad (4.2)$$

where  $T_p$  is the peak period and  $\alpha$  a coefficient of  $O(1)$ . The fraction of breaking waves,  $Q_b$ , is computed from the implicit relation:

$$Q_b = \exp\left(\frac{1 - Q_b}{(H_{rms}/H_{max})^2}\right) \quad (4.3)$$

where  $H_{rms}$  represents the root mean square wave height and the maximum wave height,  $H_{max}$ , is given by:

$$H_{max} = \frac{0.88}{k} \tanh\left(\frac{\gamma kh}{0.88}\right) \quad (4.4)$$

Here  $\gamma$  is a wave breaking parameter representing saturation.

The group velocity is obtained from linear wave theory:

$$c_g = \frac{d\omega}{dk} = \left(\frac{1}{2} + \frac{kh}{\sinh(2kh)}\right) c \quad (4.5)$$

where  $\omega$  is the angular frequency,  $k$  the wave number,  $h$  the total water depth (including set-up) and  $c$  the phase speed given by:

$$c = \frac{\omega}{k} \quad (4.6)$$

Given the bottom topography the wave number,  $k$ , can be obtained from the linear wave dispersion relation:

$$\omega^2 = gk \tanh(kh) \quad (4.7)$$

$g$  being the gravitational acceleration. The wave incidence angle,  $\theta$ , is obtained from the computed wave refraction over the bottom topography.

The wave energy dissipation serves as input in the balance for the roller energy,  $E_r$  (Nairn et al., 1989, Stive and de Vriend, 1994):

$$\frac{\partial 2E_r c \cos(\theta)}{\partial x} + \frac{\partial 2E_r c \sin(\theta)}{\partial y} = -D_r + D_w \quad (4.8)$$

where  $D_r$  represents the roller energy dissipation expressed by (Longuet-Higgins, 1970, Deigaard, 1993):

$$D_r = c\tau_t \quad (4.9)$$

and  $\tau_t$  represents the wave-averaged shear stress between the roller and wave interface. The shear stress for a steady roller is given by (Duncan, 1981):

$$\tau_t = \frac{\rho g A \sin(\beta)}{L} \quad (4.10)$$

where  $\rho$  is the water density,  $\beta$  represents the slope of the wave front,  $A$  the roller area and  $L$  the wave length corresponding to  $T_p$ . The roller area is related to the roller energy by (Svendsen, 1984):

$$E_r = \frac{\rho A c^2}{2L} \quad (4.11)$$

so eq. 4.9 can be rewritten to:

$$D_r = \frac{2g \sin(\beta) E_r}{c} \quad (4.12)$$

choosing  $\beta$  a single unknown is left in eq. 4.8,  $E_r$ , which is taken to be zero at the upwave boundaries.

## 4.2.2 Current velocity

The wave-group and depth-averaged current velocity field is computed with non-linear shallow water equations. The continuity equation is given by:

$$\frac{\partial \bar{\eta}}{\partial t} + \frac{\partial (hu)}{\partial x} + \frac{\partial (hv)}{\partial y} = 0 \quad (4.13)$$



where  $\bar{\eta}$  represent the short wave-averaged water level,  $u$  and  $v$  the short-wave and depth-averaged velocity components in the  $x$  and  $y$  direction respectively. The cross-shore momentum balance is given by:

$$\frac{\partial u}{\partial t} + u \frac{\partial u}{\partial x} + v \frac{\partial u}{\partial y} = -F_x - g \frac{\partial \bar{\eta}}{\partial x} + \frac{1}{h} \frac{\partial}{\partial x} \left( \nu_t h \frac{\partial u}{\partial x} \right) + \frac{1}{h} \frac{\partial}{\partial y} \left( \nu_t h \frac{\partial u}{\partial y} \right) - \tau_x \quad (4.14)$$

where  $\tau_x$  represents the short-wave averaged combined wave and current bottom shear stress in the cross-shore direction. The alongshore momentum equation is given by:

$$\frac{\partial v}{\partial t} + u \frac{\partial v}{\partial x} + v \frac{\partial v}{\partial y} = -F_y - g \frac{\partial \bar{\eta}}{\partial y} + \frac{1}{h} \frac{\partial}{\partial x} \left( \nu_t h \frac{\partial v}{\partial x} \right) + \frac{1}{h} \frac{\partial}{\partial y} \left( \nu_t h \frac{\partial v}{\partial y} \right) - \tau_y \quad (4.15)$$

where  $\tau_y$  represents the short-wave averaged combined wave and current bottom shear stress in the alongshore direction.

The forces  $F_x$  and  $F_y$  represent the wave forcing. They are defined as:

$$F_x = \frac{1}{\rho h} \left( \frac{\partial S_{xx}}{\partial x} + \frac{\partial S_{yx}}{\partial y} \right) \quad (4.16)$$

$$F_y = \frac{1}{\rho h} \left( \frac{\partial S_{yy}}{\partial y} + \frac{\partial S_{xy}}{\partial x} \right) \quad (4.17)$$

where the subscripts refer to the direction in which the forces act and the radiation stress, including the roller contribution, is obtained from linear wave theory:

$$S_{xx} = \left( n \left( 1 + \cos^2(\theta) \right) - \frac{1}{2} \right) E_w + 2 \cos^2(\theta) E_r \quad (4.18)$$

$$S_{xy} = \sin(\theta) \cos(\theta) (E_w + 2E_r) \quad (4.19)$$

$$S_{yy} = \left( n \left( 1 + \sin^2(\theta) \right) - \frac{1}{2} \right) E_w + 2 \sin^2(\theta) E_r \quad (4.20)$$

with:

$$n = \left( \frac{1}{2} + \frac{kh}{\sinh(2kh)} \right) \quad (4.21)$$

The eddy viscosity,  $\nu_t$ , associated with lateral mixing is obtained from (Batjes, 1975):

$$\nu_t = h \left( \frac{D_r}{\rho} \right)^{\frac{1}{3}} \quad (4.22)$$

where the roller energy dissipation,  $D_r$ , is obtained from the wave transformation. Various boundary conditions can be applied for the flow model, prescribing velocities, discharges or surface elevation. Details will be discussed in the relevant sections on model-data comparison.

## 4.3 Comparison with laboratory data

### 4.3.1 Reduction of equations

Given the fact that the experimental set-up, described in Chapter 2, represents an alongshore uniform configuration, the wave and flow equations can be simplified to account for cross-shore variations only. This reduces the computational effort and facilitates the analysis. At present we are interested in the mean flow characteristics and therefore wave-group averaged quantities are considered in the following. The balance for the wave energy now reduces to:

$$\frac{dE_w c_g \cos(\theta)}{dx} = -D_w \quad (4.23)$$

Given the alongshore uniformity the wave incidence angle can be obtained from Snell's law:

$$\frac{\sin(\theta)}{c} = \frac{\sin(\theta_0)}{c_0} \quad (4.24)$$

where the subscript, 0, denotes a reference point offshore.

The roller energy equation reduces to (Stive and de Vriend, 1994):

$$\frac{d(2E_r c \cos(\theta))}{dx} = -\frac{2g \sin(\beta) E_r}{c} + D_w \quad (4.25)$$

The storage of wave energy and momentum depends on the value of the wave slope  $\beta$ . Large values correspond to more or less instantaneous dissipation, resulting in a small roller area, and vice versa. The wave slope is not known a priori, but given the fact that the roller contributes to the set-up of the mean water level, a good estimate of  $\beta$  can be obtained from the time-averaged cross-shore momentum balance:

$$F_x + g \frac{d\bar{\eta}}{dx} = 0 \quad (4.26)$$

where the zero mean mass flux in the cross-shore direction has been taken into account. The first term represents the gradient in radiation stress associated with the wave and roller motion, the second term the cross-shore pressure gradient associated with the set-up,  $\bar{\eta}$ . The combined cross-shore wave-current bottom shear stress,  $\tau_x$ , has been neglected.

The above results in three coupled differential equations to model the wave transformation, being the time-averaged wave energy balance (4.23), the energy balance for rollers in breaking waves (4.25) and the cross-shore momentum balance to compute the set-up of the mean water level (4.26). The three equations are solved simultaneously by numerical integration over the cross-shore profile (implemented in the numerical model UNIBEST-TC, Bosboom et al., 1997), resulting in the cross-shore distribution of wave height, set-up and roller energy. The model requires a bottom profile and boundary conditions for the wave energy,  $E_w$ , the roller energy,  $E_r$  and the set-up,  $\bar{\eta}$ . In addition  $\beta$  has to be chosen and a number of coefficients have to be defined, viz. two wave breaking parameters,  $\alpha$ , which is set at 1, and  $\gamma$  which is obtained from (Battjes and Stive, 1985):

$$\gamma = 0.5 + 0.4 \tanh \left( 33 \frac{H_{rms,0}}{L_0} \right) \quad (4.27)$$

The longshore current velocity is computed from the reduced wave-and depth averaged alongshore momentum equation, Eq. 4.15, which is rewritten as:

$$F_y = \frac{1}{h} \frac{d}{dx} \left( \nu_t h \frac{dV}{dx} \right) - \tau_y \quad (4.28)$$

where  $V$  is the mean longshore current. The first term represents the forcing due to a change in wave-induced momentum flux as a result of wave and roller dissipation, the second term is the horizontal mixing where the cross-shore variation of the turbulent eddy viscosity is taken into account. The depth-invariant alongshore wave induced forcing can also be obtained from the alongshore component of the shear stress (Deigaard, 1993);

$$F_y = \tau_t \sin(\theta) \quad (4.29)$$

The (non-linear) bottom shear stress is modelled as:

$$\tau_y = \frac{1}{T_p} \int_0^{T_p} \rho c_f \sqrt{\tilde{u}^2 + 2\tilde{u}V \sin(\theta) + V^2} (V + \tilde{u} \sin(\theta)) dt \quad (4.30)$$

where  $c_f$  is a friction coefficient and  $\tilde{u}$  the instantaneous near-bed orbital velocity based on the  $H_{rms}$  and in the direction of wave propagation. In the computations  $c_f$  is used as a fit parameter. The whole set results in an implicit second order differential equation in  $V$ , which is solved iteratively; boundary conditions are provided by setting  $V$  to zero offshore and at the shoreline.

### 4.3.2 Results

The test involving random waves, SO014, has been selected from the set of laboratory measurements (see Chapter 2) for a comparison study, based on the knowledge that random waves give a better approximation of what happens in the field. Numerical model results are compared to the measurements thereby assessing effects of rollers, bottom friction and lateral mixing on the cross-shore distribution of the longshore current velocity.

The result for the wave height transformation and set-up of the mean water level is shown in Figure 4.1. Overall, both wave height and set-up compare

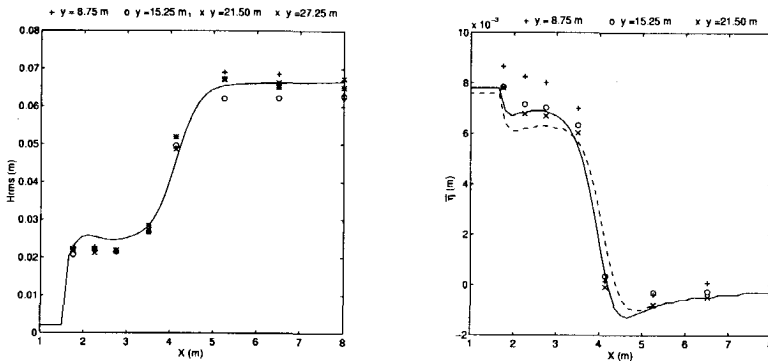


**Figure 4.1:** Left panel: Wave height transformation, comparison between computational results (solid line) and measurements. Right panel: Set-up of mean water level computed with (solid line) and without (dashed line) the roller contribution, compared with measurements.

favourably with the measurements. In the trough the wave height is slightly overpredicted. Still, the wave energy decay over the bar is well predicted and so is the set-up if the roller effect is included with  $\beta = 0.1$ . In the case where the roller is not included, the set-up level near the shore line is somewhat underestimated (Figure 4.1). However, inclusion of the roller appears to cause hardly any spatial lag in the present case.

The measurements for the longshore current velocity were performed at one third of the water depth from the bed, which in the case of a logarithmic velocity profile is representative for the depth-averaged flow. However, it is not known whether the velocity profiles are actually logarithmic, so the measured velocities may differ from the depth averaged velocity. In the comparison between measurements and model results, it is assumed that these differences are small.

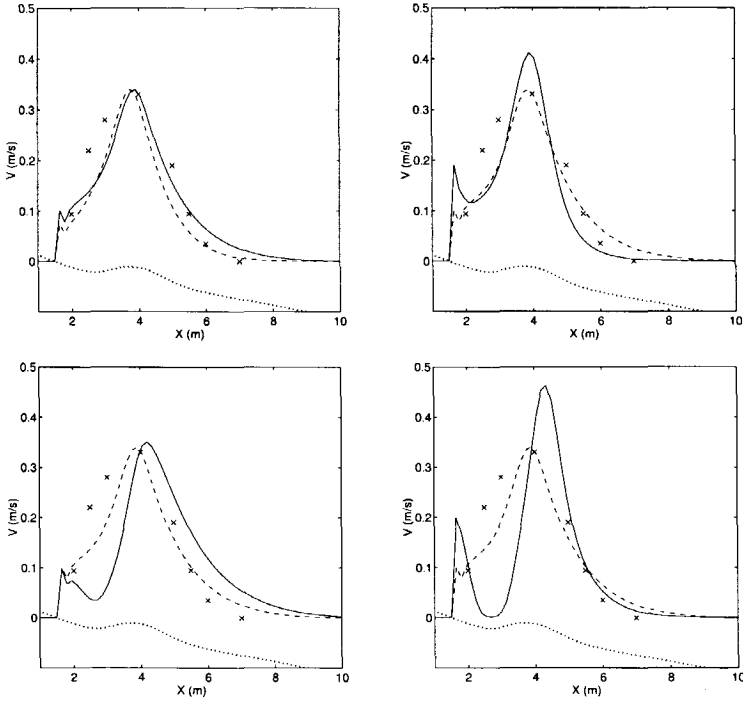


**Figure 4.2:** Computed longshore current velocities. Upper left panel: Using linear,  $c_f = 0.015$  (dashed line) and non-linear,  $c_f = 0.007$  (solid line) bottom shear stress. Upper right panel: Without mixing. Lower left panel: Without a roller. Lower right panel: Without a roller and without mixing. Measurements at  $y = 21.50$  m ( $x$ ) and bottom profile (dotted line, not to scale) are given as a reference.

The results for the computed longshore velocities, using  $c_f = 0.007$ , show good agreement with the measurements (see upper left panel Figure 4.2). The cross-shore distribution of the longshore current velocity profile matches the measured distribution quite well. The location and the value of the computed and measured maximum longshore current velocity coincide though the limited cross-shore resolution in the measurements has to be kept in mind. This shows the ability to predict the longshore current velocity profiles for purely wave driven flows on barred beaches, for alongshore uniform conditions, using existing model equations.

A closer look at the results shows that the longshore current velocities are overpredicted at the seaward end of the bar and underpredicted in the trough. It is difficult to say what causes these differences, given the fact that forcing, mixing and bottom friction have similar order effects on the predicted current velocities in these areas. These effects are examined in more detail below.

The sensitivity of the computed longshore current velocity to the bottom shear stress formulation is illustrated by the use of a simpler, linear bottom friction. Often the bottom shear stress is linearised under the assumptions that the longshore current velocity is small compared to the wave orbital velocity and that the angle of incidence is small (Longuet-Higgins, 1970):

$$\tau_y = \rho c_f \overline{|\bar{u}|} \sin(\theta) V \quad (4.31)$$

These assumptions are violated in the case presented, but the idea is to investigate the importance of the bottom shear stress formulation. The bottom friction coefficient,  $c_f$ , has been increased to 0.015 to give the same maximum current velocity as in the non-linear case. The resulting velocity profiles, see upper left panel of Figure 4.2, show a good agreement with the measurements both for the linear and nonlinear bottom shear stress formulations. Only minor differences in the longshore current velocity occur, an observation made earlier by Thornton and Guza [1986].

The roller effect on the longshore current velocity profile is illustrated in the lower panels of Figure 4.2. If the roller contribution is excluded from the longshore momentum balance the locations of the measured and computed maxima no longer coincide. The absence of storage of alongshore directed momentum in the model without roller results in a premature release of this momentum, resulting in an underestimation of the longshore current velocities in the trough. This shows that the cross-shore distribution of the alongshore forcing can only be modelled correctly if the roller contribution is taken into account.

If mixing is included, only part of this effect is compensated (see lower left panel of Figure 4.2), but it also leads to an overestimation of the current velocities offshore. Though mixing by itself has no significant impact on the position of maximum velocity it is important in modelling the cross-shore distribution of the

longshore current (see the upper right panel of Figure 4.2). It is often assumed that in case of random waves, no additional mixing is required to model the longshore current velocity profile. In this case however, the predicted longshore currents are clearly too narrow compared to the measurements if mixing is not included. It seems therefore that in the case of random waves on a barred beach the lateral mixing effect is more important than in the case of random waves on a plane beach. This is ascribed to the fact that in the case of a plane beach there is a gradual increase and decrease in the wave forcing as the water depth decreases, whereas on a barred beach there is concentrated wave breaking on the bar followed by a rapid decrease in the number of breaking waves in the trough, resulting in stronger shears and thereby increased mixing.

Overall, it appears that both roller and lateral mixing have effects on the longshore current profile of comparable magnitude but of a different kind: the roller shifts the profile shoreward and mixing smears it out. Both are needed to obtain reasonable agreement with the measured profile.

## 4.4 Comparison with field data

### 4.4.1 Description of experiment

The field data were obtained during the DELILAH experiment in 1990 at the US Army Corps of Engineers' Field Research Facility at Duck, North Carolina. An overview of the area is shown in Figure 4.3. Recognising the pier which extends approximately 800 m into the easterly direction, the measuring area, also known as the mini grid, starts at a distance of 250 m north of the pier and extends over a length of approximately 400 m along the beach and 350 m in the cross-shore direction covering the surfzone. The local bathymetry in the vicinity of the pier can vary significantly with respect to the areas further away, which are generally much more alongshore uniform.

The measurements used throughout this section have been obtained from a cross-shore measurement array deployed within the mini grid to measure the wave transformation and cross-shore distribution of the longshore current velocities (see right panel of Figure 4.3). Note that the comparison with model results is based on the depth averaged mean longshore current velocities. The vertical elevation of the instruments is a function of the initial position and bed level. The bed level changes from day to day, which was measured each day. Assuming that the vertical velocity profile of the mean longshore current is logarithmic, the measured current velocities were corrected to yield the depth averaged current velocities using the measured depth of water and elevation of the current meter relative to the bed for each day.

The waves and resulting longshore currents varied considerably during the

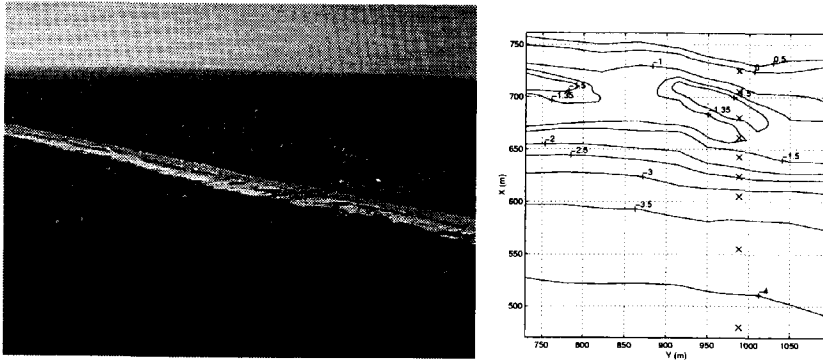


**Figure 4.3:** Left panel: Plan view of Field Research Facility at Duck, North Carolina. Offshore pier direction coincides with east (courtesy of FRF). Right panel: Part of minigrid with bathymetry of 10 Oct. Position of velocity meters and colocated pressure transducers denoted by x's.

experiment. Waves and currents were mild from 3-9 October. On the 10th, a frontal system from the south generated broad-band waves at relatively large angles (about 40 degrees from the south in 8 m depth) driving a strong longshore current to the north (up to 1.5 m/s). The storm abated between the 11th and 12th, when on 13 October, large swell waves ( $H_s \sim 2.5\text{m}$ ) arrived from the south due to distant hurricane Lili; these waves gradually diminished on subsequent days. On the 19th, a small frontal system passed from the north generating waves from the north and currents to the south (see Thornton et al., 1996 for details).

The large scale morphology responded to the changing waves and currents. The morphology normally features rhythmic crescentic bars during times of quiescent waves. Alongshore rhythmic features are evident on the 10th of October in the time-lapse video exposure (Figure 4.4) where wave breaking is inferred from the lightly coloured areas owing to surface foam, i.e. over the bar and near the shoreline. The video image clearly shows the cyclic character of the observed undulations extending far beyond the mini grid. The morphology tends to a linear bar(s) during times of storms with strong longshore currents, which is reflected in subsequent video exposures for 12, 15 and 19 October (see Figure 4.4). There is often a bulge of sand at the foot of the pier and a scour hole at the end of the pier. The persistent longshore currents to the north during 10-18 October moved this bulge of sand progressively northward into the measurement area. As will be seen, this bulge of sand can have a strong effect on the hydrodynamics.



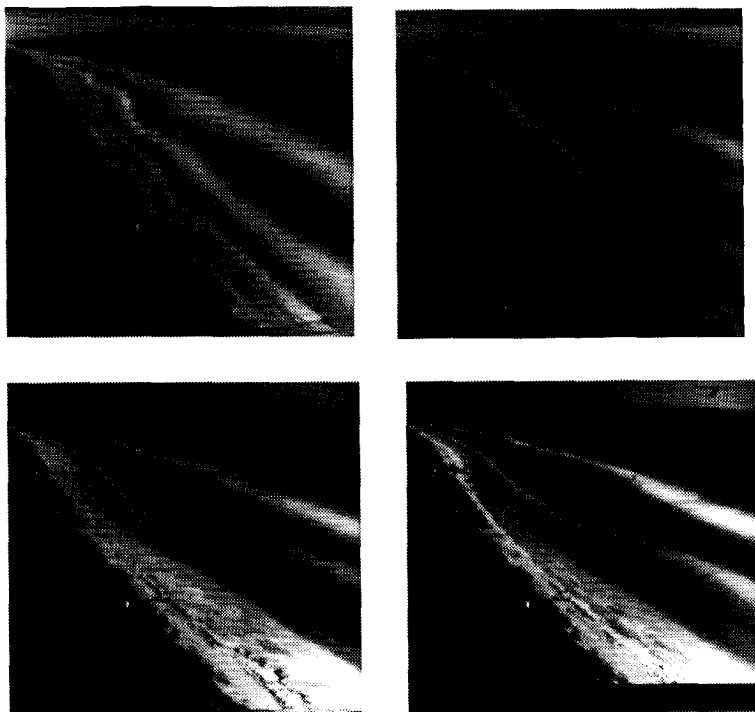


**Figure 4.4:** *Time lapse video exposures of the nearshore on 10 (upper left), 12 (upper right), 15 (lower left) and 19 (lower right) October.*

#### 4.4.2 Reduction of equations

From the video imaging it is clear that the morphology present from 10 to 19 October of the field experiment is not uniform alongshore. Therefore the full equations should be used to compute the spatial distribution of the wave and flow field. However, considering the cross-shore and alongshore length scales Putrevu et al. (1995) showed that for weak alongshore variations a reduced set of equations can be obtained. In that case the wave transformation can be computed with the previously described 1-D wave propagation model. By applying the wave transformation model to a number of consecutive transects alongshore, the spatial distribution of wave height and resulting set-up are obtained. From this, the local alongshore pressure gradient across the transect of interest can be estimated. This has the advantage of a simple 1D approach, though including

the effect of an alongshore pressure gradient on the longshore current velocity profile. The wave and depth averaged alongshore momentum equation is then given by

$$F_y = \frac{1}{h} \frac{\partial}{\partial x} \left( \nu_t h \frac{\partial V}{\partial x} \right) - g \frac{\partial \bar{\eta}}{\partial y} - \tau_y \quad (4.32)$$

in which the forcing due to an alongshore pressure gradient, given by the second term on the right hand side, is included. The formulation above is subject to the following assumptions made by Putrevu et al. (1995): The longshore current velocity is expected to be small with respect to the phase speed of the incident waves:

$$V_{max} \sim \epsilon \sqrt{gh_b} \quad (4.33)$$

where  $\epsilon = O(.2)$  and  $h_b$  represent the water depth at which the waves start breaking. The incidence angle at wave breaking is small:

$$\sin(\theta_b)/\epsilon = O(1) \text{ and } \cos(\theta_b) \simeq 1 \quad (4.34)$$

The alongshore length scale is much larger than the cross-shore length scale:

$$L_x/L_y \sim \epsilon \quad (4.35)$$

and the maximum set-up of the mean water level is of  $O(\delta)$  with respect to the depth at breaking:

$$\bar{\eta}_{max} = \delta h_b \text{ and } \delta \ll 1 \quad (4.36)$$

These assumptions will be checked for each individual case. Given the predominance of swell in the observed wave conditions, the dissipation is modelled according to Thornton and Guza (1983), given by:

$$D_w = \frac{3}{16} \sqrt{\pi} \rho g f_p B^3 \frac{H_{rms}^3}{h} M \left[ 1 - \frac{1}{(1 + (H_{rms}/\gamma h)^2)^{\frac{5}{2}}} \right] \quad (4.37)$$

where  $f_p$  is the peak frequency,  $B$  a coefficient of  $O(1)$ , and the weighting function,  $M$ , is given by (Whitford, 1988)

$$M = \left( 1 + \tanh \left[ 8 \left( \frac{H_{rms}}{\gamma h} - 1 \right) \right] \right) \quad (4.38)$$

The wave energy dissipation again acts as a source term in the roller energy balance (equation 4.25). However, measured set-up data is not available to calibrate the roller model. Therefore the roller dissipation has been modelled as

a function of the wave asymmetry (Lippmann et al., 1994) and calibrated with visual observations of the spatial variation of wave breaking across the profile (Lippmann and Thornton, 1996). A brief description of their approach is given here. The wave asymmetry,  $e_w$ , is related to the wave slope by:

$$\sin(\beta) = \frac{2H_{rms}}{eL_p} \quad (4.39)$$

where  $L_p$  is the wave length associated with the peak frequency. Introducing this into eq. 4.25 gives:

$$\frac{\partial(2E_r c \cos(\theta))}{\partial x} = -\frac{4gH_{rms}}{eL_p} E_r + D_w \quad (4.40)$$

Taking into account the distribution of wave rollers, the average roller energy is defined by:

$$E_r = \frac{2\rho c^2}{L_p} \int_0^\infty Ap(H)W(H)dH \quad (4.41)$$

where  $p(H)$  is the wave height distribution of the incident waves and  $W(H)$  a weighting function which determines when rollers exist and  $A$  is a function of the local wave height:

$$A = \frac{L_r^3}{e_w^2 L_p^3} \sqrt{\frac{g}{h}} \frac{H^2}{T_p} \quad (4.42)$$

and the roller length,  $L_r$ . A solution of eq. 4.40, with  $L_r$  and  $e_w$  being the only unknowns, can be obtained for a given value of  $e_w$ . By matching the computed cross-shore distribution of the percentage of wave breaking:

$$Q(x) = \int_0^\infty p(H)W(H)dH \quad (4.43)$$

to the measurements an optimal value for  $e$  and the corresponding roller energy dissipation,  $D_r$ , is obtained.

### 4.4.3 Comparison

In the next part, comparisons of field data with numerical model results are described. The procedure in all cases is to calibrate the wave transformation model based on the measured wave height and percentage of wave breaking along the cross-shore measurement transect. Once calibrated, the wave transformation model is applied to cross-shore transects throughout the mini grid. Next, the local alongshore pressure gradient and alongshore shear stress are used to drive the longshore current over the measurement transect. The hydrodynamic conditions for the various cases are presented in Table 4.1. Intercomparison of the different cases is used to assess the effects of wave forces and alongshore pressure gradients on the longshore current velocities.

Day	time (h)	$\delta h$ (m)	$H_{rms}$ (m)	$T_p$ (s)	$\theta^\circ$	$h_b$ (m)	$V_{max}$ (m/s)	$U_w$ (m/s)	$\theta_w^\circ$
Oct 10	05	-0.37	0.80	10.7	-38.	2.3	1.0	2.2	111.
Oct 12	07	-0.15	0.90	8.9	-38.	2.7	0.9	5.1	67.
Oct 19	05	-0.11	0.86	5.8	60.	2.4	0.8	9.1	-141.
Oct 18	16	-0.20	0.82	6.2	-46.		0.7	11.2	76.

**Table 4.1:** Test Conditions,  $\delta h$ : tidal elevation relative to mean sea level,  $H_{rms}$ ,  $T_p$  and  $\theta$  all at 8 m water depth.  $h_b$ : depth at breaking,  $V_{max}$ : maximum longshore current velocity,  $U_w$ : wind speed and  $\theta_w$ : wind direction with respect to the coast normal.

#### 4.4.4 Weak alongshore variation

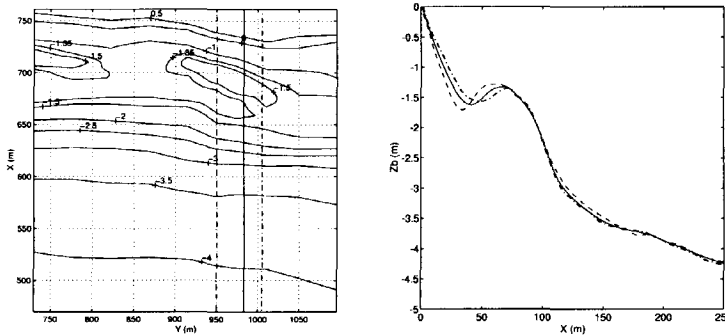


**Figure 4.5:** Left panel: Bathymetry for computational domain obtained for 10 Oct. Middle and neighbouring transects indicated by vertical lines; corresponding profiles shown in right panel.

On Oct. 10 moderate swell waves,  $H_{rms} = .80$  m, with a  $T_p$  of 10.7 s, were incident from the south-east at an angle,  $\theta$ , of  $-38^\circ$  with the coast normal. The bottom contours obtained with linear interpolation between various bottom profile measurements for Oct. 10 are shown in the left panel of Figure 4.5. The spacing between the individual profiles is in the order of 25 meters. The bathymetry clearly shows the presence of alongshore non-uniformities, with alongshore length scales of  $O(200)$  m. The differences in bed-level along the bar crest and trough are of  $O(.2)$  m. The bathymetry has a typical barred profile as was observed during most of the time throughout the DELILAH field experiment. The bar crest is located approximately 100 m offshore with a water depth in the or-

der of 1.2 m with respect to the mean sea level. This is followed by a trough region with a maximum water depth in the order of 1.7 m. The offshore slope is  $O(1 : 100)$ . The slope at the seaward side of the bar and near the shore line are both  $O(1 : 20)$ . The accuracy of the bathymetric survey system is of  $O(.03)$  m.

The bathymetry transects were measured at a small angle ( $1-4^\circ$ ) to the shore normal (see left panel Figure 4.5). To align the calculations in the longshore direction, the bottom profiles used in the computational wave transformations are shifted in the cross-shore direction such that the offshore side of the bar coincides in each transect (see right panel Figure 4.5). This assumption is based on the fact that the differences in bathymetry in the alongshore direction are small compared with the total water depth, and therefore, will not affect the mean flow direction of the longshore current.

Next we check whether the underlying assumptions based on a slow alongshore modulation of the bathymetry as defined by Putrevu et al. [1995] are valid for Oct. 10. Wave breaking starts on the seaward side of the bar at a depth of 2.3 m where the tidal elevation of approximately  $-0.4$  metres has been taken into account. The maximum longshore current velocity is in the order of 1 m/s which gives:

$$\epsilon = \frac{V_{max}}{\sqrt{gh_b}} \simeq 0.20$$

which is okay. The angle of incidence at breaking is estimated at  $15^\circ$  thereby complying with the afore mentioned assumptions. Estimates of the length scales involved are obtained from the bottom slope in both directions,  $s_x = 1:20$  and  $s_y = 1:100$ , as measured from the bathymetric survey data (see Figure 4.5).

$$\frac{L_x}{L_y} = \frac{s_y}{s_x} = 0.20 = O(\epsilon)$$

The maximum set-up of the mean water was not measured but is estimated from numerical calculations to be in the order of 0.1 m:

$$\delta = \frac{\eta_{max}}{h_b} = O(0.05) \ll 1$$

which shows that the assumptions made have not been violated for Oct. 10. Note that the scaling arguments for the trough are different, given the fact that the bed level becomes more or less horizontal and waves cease breaking. This will be discussed later.

The wave transformation model comparison with data is shown in the left panel of Figure 4.6. Incident waves from the south-east refract and shoal while propagating from deeper water. Wave breaking occurs mainly on the bar, resulting in a strong decrease in wave height. The waves reform in the trough where the height stays more or less constant, followed by additional wave breaking near

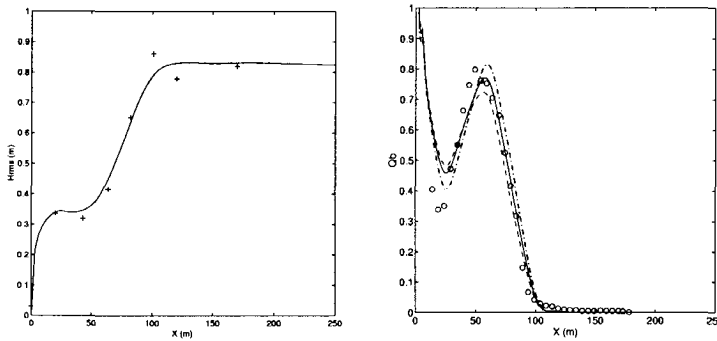


**Figure 4.6:** Left panel: Computed transformation of  $H_{rms}$  at the measurement transect (solid line) compared with measurements (+). Right panel: Fraction of breaking waves for Oct. 10, measurements (o) and model results obtained for  $e_w = 0.5$  (dash-dotted line),  $e_w = 0.7$  (solid line) and  $e_w = 0.9$  (dashed line).

the shore line. The computations show a good match with the measurements. The calibration of the roller dissipation model is obtained from the match with the measured percentage of breaking waves. A good match between the measurements and computations is obtained for an asymmetry value,  $e_w$ , of 0.7 (Figure 4.6).

Next, the calibrated wave transformation model is applied at two adjacent transects. The waves in the south transect decay more over the bar (see upper left panel Figure 4.7, due to the smaller water depth. This results in a locally higher set-up of the mean water level (upper right panel Figure 4.7),  $O(2)$  cm, but relatively less wave energy in the trough and less set-up at the shore line. Near the shore line, the cross-shore set-up gradients are very steep. So a small offset in the cross-shore position, based on the expected stream lines, results in large alongshore set-up gradients. Based on the present modelling effort it is not possible to make a reliable estimate of the alongshore set-up gradients near the shoreline. These are therefore not taken into account, the main interest being the forcing of longshore current in the trough. Note that the depth of water near the shore line is small and therefore the expected pressure gradients are small also.

Given that the set-up level south of the measurement transect is higher than to the north, the pressure gradient acts in the same direction as the wave forcing (lower left panel Figure 4.7). The longshore current calculations are compared with measurements (upper right panel Figure 4.7). If the local pressure gradient is ignored, the position of the maximum longshore current velocity is predicted

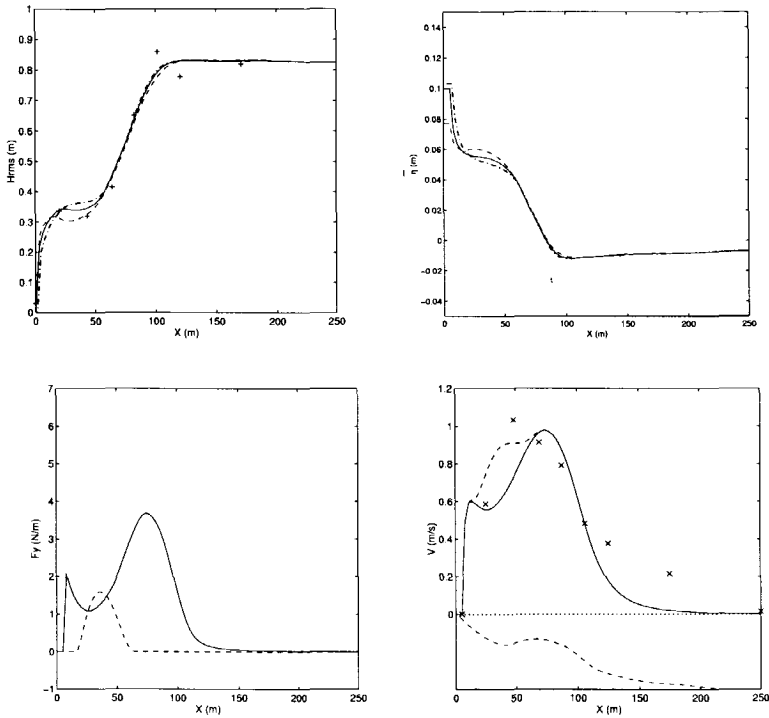


**Figure 4.7:** Conditions on Oct 10. Upper left panel:  $H_{rms}$  at the measurement transect computed (solid) and measured ('+'), the southerly (dashed) and northerly transect (dash-dotted) respectively. Upper right panel: corresponding computed set-up. Lower left panel: Wave forcing (solid) and local alongshore pressure gradient (dashed). Lower right panel: Longshore current velocities using  $c_f = 0.0035$  with (dashed) and without (solid) the local pressure gradient. Bottom profile (dashed) is given as a reference (not to scale).

to be near the bar crest, whereas the measurements show the maximum to be in the trough. Including the local pressure gradient results in a better match with the measurements, showing a strong flow in the trough. Next we look at a case of strong alongshore variation.

#### 4.4.5 Strong alongshore variation

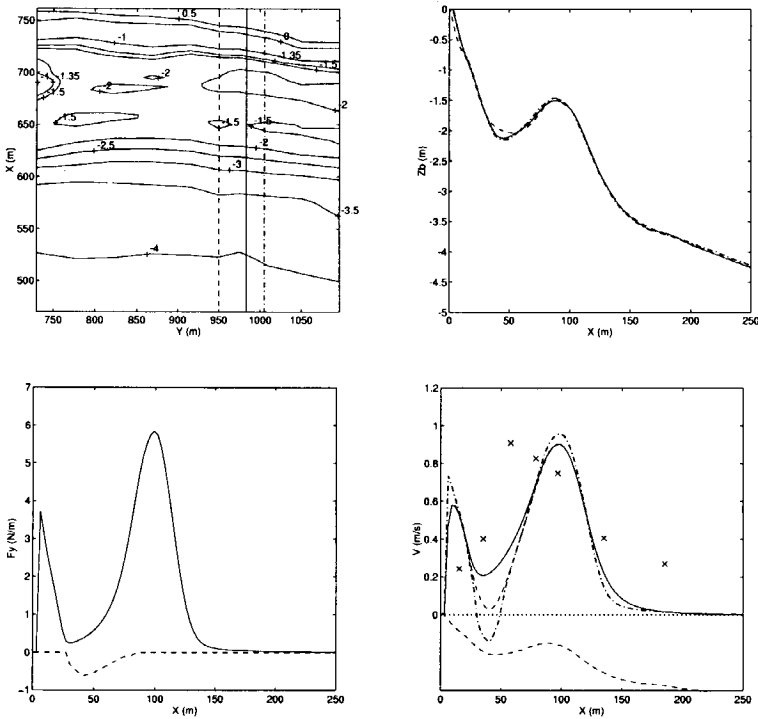


**Figure 4.8:** Conditions on Oct 12. Upper left panel: Bathymetry. Upper right: Corresponding bottom profiles. Lower left panel: Computed wave forcing (solid) and local alongshore pressure gradient (dashed). Lower right panel: Computed longshore current velocities (solid line), without pressure gradient (dashed line) and without mixing (dash-dotted line) with  $c_f = 0.006$ . Measurements denoted with 'x'.

In the vicinity of the measurement transect, the bathymetry for October 12 (lower left panel of Figure 4.8) is more uniform alongshore than in the previous



case, with a linear bar and trough. However, further south toward the pier, the bathymetry is no longer uniform alongshore, showing a change in the single barred profile.

The same procedure as described previously is used to compute the local forcing and the corresponding longshore current. The bottom profiles of the two adjacent transects are shown in the upper right panel of Figure 4.8, which shows a mild variation of the bed level in the trough, becoming shallower toward the south. The bar crest however has very little alongshore variability.

The forcing due to wave breaking and pressure gradient are shown in the lower left panel of Figure 4.8. Only a small gradient in the set-up level remains in the trough, resulting in a forcing that is directed in the opposite direction from the wave forcing.

Next the longshore current velocities with and without a pressure gradient are computed (lower right panel Figure 4.8). The results show that including the local pressure gradient does not improve the computation of the longshore current velocities. The computations show a maximum velocity near the bar crest, unlike the measured velocity distribution, which shows a maximum closer to the trough. Applying the alongshore pressure gradient results in an increased discrepancy between the computed and measured longshore current velocities in the trough. It is interesting to see that there is no flow reversal, even though the pressure gradient is locally larger than the wave forcing. Mixing causes the profile to smooth out, resulting in a unidirectional flow field (lower right panel Figure 4.8). Therefore, flow reversals would not be expected if the opposing pressure gradient is small with respect to the wave forcing.

From the time exposures of breaking waves (Figure 4.4) it is apparent that on October 12 the toe of a much larger bed feature is entering the computational domain. Near the toe the alongshore length scale is of similar order as the cross-shore length scale (see Figure 4.8). The response of the set-up of the mean water level to the changes in the profile south of the measurement transect is shown in Figure 4.9. Note that given the strong variations of the bed, it is no longer appropriate to use a one-dimensional wave propagation model to compute the wave transformation and set-up. What follows is therefore predominantly a qualitative assessment of the effect of a strong alongshore pressure gradient acting over the trough. Given the strong alongshore variations in bathymetry, the longshore current inertia has been added to the alongshore momentum equation:

$$V \frac{\partial V}{\partial y} = -F_y - g \frac{\partial \bar{\eta}}{\partial y} + \frac{1}{h} \frac{\partial}{\partial x} \left( \nu_t h \frac{\partial V}{\partial x} \right) - \tau_y \quad (4.44)$$

represented by the first term. Next the relative importance of the various contributions in eq. 4.44 for the longshore current in the trough is discussed. We

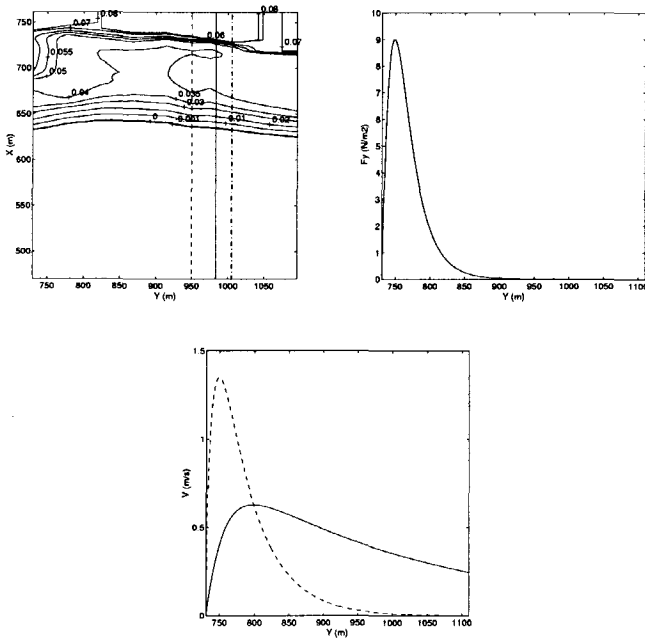


**Figure 4.9:** Conditions on Oct 12. Left panel: Synoptic view of the set-up of the mean water level in m. Right panel: Estimated forcing along the beach over the trough due to the presence of an alongshore pressure gradient. Lower panel: Corresponding longshore current velocity in the trough with (solid) and without inertia terms (dashed).

discriminate between cases where alongshore pressure gradients and wave forcing are acting in the same direction or in opposite directions. In both cases there is a strong decrease in the wave forcing once the waves enter the trough and breaking occurs less frequently. Consequently the turbulent eddy viscosity becomes less. Without mixing, the case of wave forcing and pressure gradient acting in opposite directions leads to flow reversals and corresponding strong gradients in the longshore current velocity. This means that although the eddy viscosity has decreased, lateral mixing cannot be neglected, thereby preventing the alongshore pressure gradient driven current in the trough from fully developing. Given the small longshore current velocity in the trough, the longshore current inertia becomes negligible. It is therefore expected that for the case of opposed forcing the total cross-shore distribution of the longshore current velo-

city is dominated by the wave forcing on the bar crest and shore line. This is not the case for unidirectional forcing where cross-shore velocity gradients are expected to be significantly less and lateral mixing decreases correspondingly. The geographic trapping between the shore line and bar in combination with weak lateral mixing may then lead to strong alongshore pressure gradient driven currents in the trough and a corresponding increase in the relative importance of the longshore current inertia.

Next the inertia effect for Oct 12, where a strong alongshore pressure gradient over the trough acting in the flow direction can be expected between 700 and 800 m (see Figure 4.9), is examined in more detail. The simplified alongshore momentum equation over the trough, neglecting mixing and wave forcing, is given by

$$V \frac{\partial V}{\partial y} = -\frac{c_f |V| V}{h_t} - g \frac{\partial \bar{\eta}}{\partial y} \quad (4.45)$$

where  $h_t$  is the water depth in the trough and a simplified non-linear bottom shear stress formulation has been used. The forcing is obtained from the computed alongshore set-up gradients in the trough, where a water depth of 1.5 m is used (right panel Figure 4.9). A first estimate of the longshore current velocity in the trough (right panel Figure 4.9) is computed with eq. 4.45, where  $V$  is taken to be zero at the upstream end. The inertia effect is evident as is the significant flow velocity at the measurement transect. Therefore, it is likely that only part of the longshore current resulted from local pressure gradients. In this case more sophisticated modelling tools are required to assess the effects of the upstream bathymetry on the flow conditions near the measurement transect.

The time exposures of Figure 4.4 show that further north the bathymetry is much more uniform, with a single linear bar. In cases where waves are incident from the north-east, wave forcing acts opposite to the pressure gradient resulting from the bed-undulations south of the measurement transect. It is expected that in this case the measured longshore current velocities will correspond closely to a wave-driven current only as will be seen in the next case.

#### 4.4.6 Alongshore uniformity

The short period wave conditions, with  $T_p = O(6)$  s, incident from the north-east (see Table 4.1) during the 19th of October are different from the cases previously considered. The bathymetry north of the measurement transect displays a linear bar and trough (Figures 4.4 and 4.10). It is also evident that the bed feature observed earlier has propagated further into the measuring domain.

The forcing by the local pressure gradient is shown to be small compared with the wave forcing (lower left panel of Figure 4.10)). The resulting longshore current velocity profile compares well with the measurements (right panel of

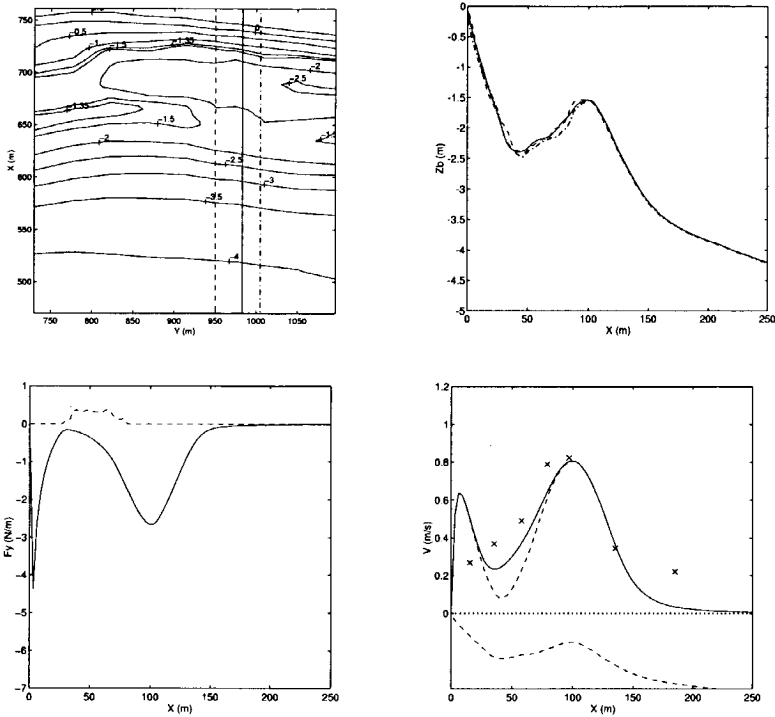


**Figure 4.10:** Conditions Oct 19. Upper left: Bathymetry. Upper right: corresponding bottom profiles. Lower left: Forcing due to wave breaking (solid) and local alongshore pressure gradient (dashed). Lower right: Corresponding longshore current velocities with local pressure gradient (solid line) and without (dashed line) for  $c_f = 0.0035$ . Measurements denoted by 'x'.

Figure 4.10)). Note that in this case the current velocity maxima, both measured and computed, are near the bar crest where wave breaking occurs, unlike the previous cases with a maximum current velocity in the trough. This supports the assumption that a relatively small pressure gradient cannot generate a strong flow in the trough if it acts in the opposite direction to the wave forcing. The model results show a second maximum close to the shore, but measurements are not available in that region to conclude as to whether a second maximum is actually present or not.

## 4.5 Discussion

In this Chapter we attributed the observed discrepancies between the measured and computed longshore current velocity profiles for the various field cases to the presence of an alongshore pressure gradient. An important aspect in reaching this conclusion is the comparison with laboratory data. During the laboratory experiment the effect of an alongshore pressure gradient was minimised. Using a simplified balance between the estimated alongshore pressure gradients over the trough and bottom shear stress, neglecting wave forcing and lateral mixing, we typically find for the laboratory experiment:

$$V = \frac{gh_t}{c_f|U|} \frac{\Delta\bar{\eta}}{\Delta y} = \frac{9.81(m/s^2) \cdot 0.07(m)}{0.01 \cdot 0.1(m/s)} \frac{0.001(m)}{12.75(m)} = O(0.05)m/s \quad (4.46)$$

where  $U$  represents the orbital velocity. The resulting current velocity is indeed small with respect to the measured velocity in the trough and implies a purely local wave-induced driving force.

The comparison between laboratory measurements and computational results has therefore demonstrated the ability to model purely wave driven longshore currents on barred beaches, using existing model equations. Including lateral mixing, roller effects and a non-linear bottom shear stress, good correspondence is obtained. Thus verified, the model has been used in a comparison with field data, knowing that longshore currents in the field are in general not locally wave driven only, but result from a variety of different mechanisms, including wind and pressure gradients.

Three different cases have been considered. The results suggest that in the case of slow modulation of the alongshore bottom profile the longshore current velocity distribution can be obtained from the local force balance. Still, some caution is required in concluding that this is actually the case here, not knowing what the upstream wave-and current conditions are. It is apparent from the time exposures on 10 October that we are looking at some rhythmic features in the bathymetry (Figure 4.4), but it is not known whether these features are also present south of the mini grid.

The results obtained for the second case are typical for the Delilah experiment, where long period waves incident from the south-east resulted in strong longshore currents in the trough. We have used the argument that this is a result of an alongshore directed pressure gradient acting over the trough in combination with inertia of the longshore current.

Most of the time, swell waves were incident from the south-east. However, the results obtained for the third case are typical of waves incident from the north-east, resulting in a longshore current maximum near the bar crest.

One might argue that the short period, sea wave conditions on the 19th are significantly different from the long period swell waves present during the other cases, and that this could be responsible for the observed differences in the longshore current velocity profiles. To investigate this possibility, we selected a data set where sea waves were incident from the south-east, which occurred on October 18 (see Table 4.1). Given the one day difference, the bottom profile is very much similar to October 19.

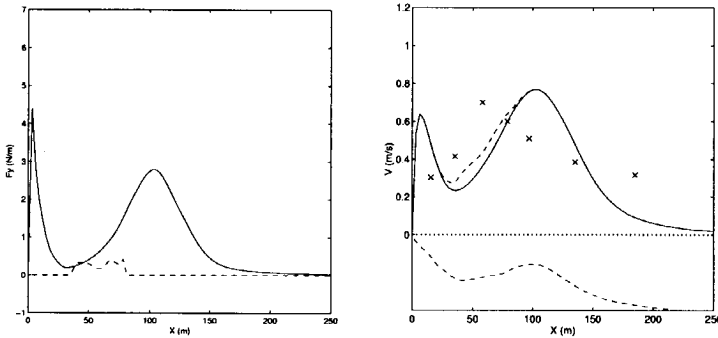


**Figure 4.11:** Conditions on Oct 18. Left panel: Wave (solid) and pressure forcing (dashed) and corresponding longshore current velocities (right panel) with the local pressure gradient (solid line) and without (dashed line) using  $c_f = 0.0035$ . Measurements denoted by 'x'.

Applying the same procedure in computing the forcing, the computational results do not show the strong flow in the trough as seen in the measurements (Figure 4.11); therefore, the difference in wave period, ie. sea or swell, is unlikely to be the reason for the observed differences.

In all cases, the current velocity further offshore is underestimated by the model results. This cannot be explained with the present analysis, given the fact that wave breaking in this area is negligible. Only part of this can be explained by the wind forcing, given the fact that for the cases under examination the wind velocity is relatively small.

## 4.6 Conclusions

Laboratory data obtained for random waves incipient on a barred beach, consisting of current velocity measurements as well as wave transformation and

set-up data, have been used for verification and validation of a numerical model for uniform alongshore conditions. Comparison of computational results with measurements showed good agreement for wave transformation, set-up and longshore current velocity profiles. This demonstrates the ability to model purely wave driven longshore currents with existing model equations. Lateral mixing was required to obtain a good match with the data. This showed that the randomness of the incident wave field by itself could not account for the necessary smoothing of the longshore current profile in the case of a barred beach. The transition effect, caused by the surface roller, was important in the correct prediction of the location of maximum wave forcing. In addition, the delayed release of alongshore wave momentum caused a significant increase in the longshore current velocity in the trough. However, in the absence of a mean alongshore pressure gradient, inclusion of the roller effect does not shift the longshore current velocity maximum on a barred beach to the deepest part of the trough.

The thus verified numerical longshore current model has been extended with an additional forcing of the longshore current due to the presence of an alongshore pressure gradient. Next the model was applied to examine the DELILAH measurement data on longshore current velocity distributions. This showed that bathymetry induced alongshore pressure gradients were present during the DELILAH experiment. Including these pressure gradients can be important in the analysis of the measured longshore current velocity profiles, which supports the earlier theoretical results obtained by Putrevu et al. [1995]. A relatively small alongshore pressure gradient over the trough, acting in the same direction as the wave forcing, has a significant effect on the longshore current velocity distribution. In the cases where this alongshore pressure gradient varies weakly in the alongshore direction, the current velocity can be obtained from the local force balance. With increased modulation, the inertia effect gains importance and the local approach is no longer valid. This was generally the case for waves incident from the south-east. In the case of opposed forcing, the computed longshore current velocity profiles match the measured longshore current, with velocity maxima over the bar and at the foreshore where waves are breaking.

Summarising, the preceding conclusions imply that in absence of an alongshore pressure gradient the maximum longshore current velocity occurs near the areas of most intense breaking, and that the occurrence of velocity maxima in the trough, as observed during the Delilah field experiment, can be ascribed to the presence of an alongshore pressure gradient (excluding wind effects).





# Chapter 5

## Longshore current instability

### 5.1 Introduction

In the previous Chapter we examined the time-mean properties of the longshore current. It is clear from the experiments described in Chapter 3 that the longshore current has dynamic properties as well. Depending on the cross-shore distribution of the wave-driven longshore current velocity, low-frequency modulations in the horizontal velocity field may be present. These oscillations result from the shear instability of the longshore current. Small perturbations in the velocity field grow at the expense of the potential vorticity associated with the longshore current. The theoretical background for this was introduced by Bowen and Holman [1989]. They obtained a linear stability equation for longshore currents, showing with a simplified test case (horizontal bottom) that the backshear of the longshore current is very important in the generation of shear instabilities. A strong back shear makes the longshore current unstable to a wide range of small perturbations. This was confirmed by Dodd and Thornton [1990] and Putrevu and Svendsen [1992] using more realistic longshore current velocity and bottom profiles. Later studies (Falqués et al., 1994) also showed that the distance of the longshore current velocity maximum to the shoreline,  $X_b$ , is important in the generation of the longshore instabilities. An increase in  $X_b$  results in a wider range of unstable wave numbers.

The generation of shear instabilities is strongly affected by the presence of dissipative effects. Putrevu and Svendsen [1992] and Dodd et al. [1992] showed that the number of possible unstable modes and their corresponding growth rate is reduced if dissipation due to bottom friction is increased. The combined effect of bottom friction and eddy viscosity on the stability of wave-driven longshore currents was investigated by Falqués et al. [1994], who show that for eddy viscosity and bottom friction giving rise to similar damping, eddy viscosity gives a stronger reduction of the span of unstable wave numbers compared to bottom

friction.

The linear stability analysis is only valid for shear instabilities of infinitesimal amplitude, i.e. initial conditions. More detailed analytical and numerical analyses were made using weakly non-linear (Dodd and Thornton, 1992) and fully non-linear modelling (Nadaoka and Yagi, 1993, Deigaard et al., 1994, Falqués et al., 1994, Allen et al., 1995, Özkan and Kirby, 1995, Özkan-Haller and Kirby, 1996 and 1997, Slinn et al., 1998) to describe the development of shear instabilities in wave-driven longshore currents to finite amplitude values.

Still, there has been little data to verify the predictions obtained from these models. The observational data presented in Chapter 3 provides an opportunity to verify numerical model results. This will be performed for both initial and finite amplitude conditions. The assumption is that the longshore current at the upstream end of the basin is more or less undisturbed by the presence of the then still small shear instabilities, corresponding to initial conditions. As the shear instabilities propagate along the beach toward the outflow they reach finite amplitude values. Both results will be used in a comparison with linear and fully non-linear model results.

First a short description of the linear stability analysis by Falques and Iranzo [1994] is given. Next the input used for the model computations is discussed, some of which is obtained from additional model computations. The model yields information on the most unstable modes for the given input conditions, which can be compared with the results obtained from the  $f, k_y$  spectral analysis (see Chapter 3). The idea is to examine the effects on the shear instabilities caused by the longshore current velocity shear, bottom shear stresses and lateral mixing.

Next the fully non-linear modelling of growing shear instabilities is discussed. The wave transformation is modelled with a 2D-wave roller model to enable a correct prediction of the wave forcing (see Chapter 4). The numerical modelling here is different from the previously mentioned studies, which apply either a forcing based on the shear component of the radiation stress neglecting the roller contribution (Nadaoka and Yagi, 1993, Deigaard et al., 1994) or an arbitrarily shaped forcing of the longshore current (Allen et al., 1995) or a forcing based on the measured longshore current velocity profile (Ozkan and Kirby, 1996). In general the latter is already affected by the presence of finite amplitude shear instabilities and as such cannot be qualified as an initial longshore current velocity profile (Bowen and Holman, 1989, see also Chapter 6). The presently used wave transformation model was shown to give a good match with observed longshore current velocity profiles over barred beaches (see Chapter 4). The velocity field, resulting from the wave forcing, is modelled with the short-wave averaged non-linear shallow water equations as presented in Chapter 4.

Parts of this chapter have been published in Reniers et al. [1997] and Reniers and Battjes [1997].

## 5.2 Linear stability analysis

### 5.2.1 Model description

In the following a comparison is made between the observational data and results obtained from a numerical model. The linear stability model used here was formulated by Falques and Iranzo [1994]. It is based on the analysis of the temporal growth of the shear instabilities. The present set of experiments is a clear case of spatial growth, starting near the inflow and growing along the beach. It would therefore be appropriate to formulate the model in terms of spatially growing modes (as opposed to temporally growing modes which is easier to solve). However, we are primarily interested in the frequency-wavenumber signature of the shear instabilities, which can be obtained for the spatial problem from a solution of the temporal problem using Gaster's relations. In Appendix A we demonstrate that the approximation given by Gaster [1962] is applicable here and that the expected errors in the dispersion relation and growth rate are of  $O(5)\%$ . This is considered acceptable, given the other uncertainties in the input conditions for the stability analysis. A detailed analysis of the consequences of using temporal vs. spatial stability analysis for the present set of experiments was performed by Dodd and Falqués [1996].

A short description of the model by Falques and Iranzo [1994] is given below. Assuming alongshore uniformity, they consider a basic undisturbed state which is a steady solution of equations 4.13- 4.15 given by  $u = 0, v = V(x), \zeta = \bar{\eta}(x)$  where  $V(x)$  is the mean longshore current and  $\bar{\eta}(x)$  the wave set up/down. Then small perturbations of the form:

$$e^{ik(y-ct)}(u'(x), v'(x), \zeta'(x)) \quad (5.1)$$

are introduced in eqs. 4.13- 4.15 which upon linearisation results in the following eigenvalue problem (dropping '):

$$ik(V - c)u + \frac{c_d V}{h}u + g \frac{\partial \zeta}{\partial x} =$$

$$2 \frac{\partial \nu_t}{\partial x} \frac{\partial u}{\partial x} + \nu_t \left( 2 \frac{\partial^2 u}{\partial x^2} - k^2 u + ik \frac{\partial v}{\partial x} + \frac{2}{h} \frac{\partial h}{\partial x} \frac{\partial u}{\partial x} + \frac{ik}{h} \frac{\partial V}{\partial x} \zeta \right) \quad (5.2)$$

$$\frac{\partial V}{\partial x} u + ik(V - c)v + 2 \frac{c_d V}{h} v - \frac{c_d V^2}{h^2} \zeta + ik g \zeta = \frac{\partial \nu_t}{\partial x} \left( \frac{\partial v}{\partial x} + ik u \right) +$$

$$\nu_t \left( \frac{\partial^2 v}{\partial x^2} - 2k^2 v + ik \frac{\partial u}{\partial x} - \frac{1}{h^2} \frac{\partial h}{\partial x} \frac{\partial V}{\partial x} \zeta + \frac{1}{h} \frac{\partial V}{\partial x} \frac{\partial \zeta}{\partial x} + \frac{1}{h} \frac{\partial h}{\partial x} \left( \frac{\partial v}{\partial x} + ik u \right) \right) \quad (5.3)$$

$$\frac{\partial(hu)}{\partial x} + ikhv + ik(V - c)\zeta = 0 \quad (5.4)$$

The eigenvalue,  $c = \omega/k = (\omega_r + i\omega_i)/k$ , is the phase speed, which may be complex. The period and the wavelength are given by  $T = 2\pi/\omega_r$  and  $\lambda = 2\pi/k$ . In these linearized equations any perturbation in the radiation stresses,  $S_{ij}$ , has been neglected. Given the strong mean current velocity of  $O(.5)$  m/s, with respect to the incident wave orbital velocity amplitude,  $O(.2)$  m/s, during the experiments (see Chapter 2), the strong current approach has been used in the bottom friction formulation:

$$\tau_y = C_d v |V| \quad (5.5)$$

where  $C_d(x)$  represents the friction coefficient. The system 5.2-5.3-5.4 has been solved numerically by using spectral expansions. The details of the numerical procedure can be seen in Falqués and Iranzo [1994].

Given any set of profiles of undisturbed longshore current velocity, bottom friction coefficient, viscosity and bathymetry, Equations 5.2-5.3-5.4 can be solved for any wavenumber,  $k$ , so that the  $k, \omega_r$  and the  $k, \omega_i$  curves, that is, the dispersion and the instability curves can be computed. The basic flow is unstable if there is some wavenumber with positive growth rate,  $\omega_i > 0$ , and stable otherwise. The fastest growing mode, denoted by FGM, corresponds to the wavenumber  $k$  at which the maximum of  $\omega_i$  occurs.

The model requires the following input: bottom profile and mean water level, mean longshore current profile, coefficient for bottom friction and eddy viscosity due to wave breaking. The mean longshore current is obtained from the measurements where a spline is used to obtain the interpolated values required for the model input. For the friction coefficient, we use the classical expression for a logarithmic velocity profile:

$$C_d = \left[ \frac{1}{\kappa} \ln \left( \frac{33h(x)}{ek_N} \right) \right]^{-2} \quad (5.6)$$

where:

$e$  = basis of natural logarithm

$\kappa$  = von Karman constant ( $\kappa \cong 0.4$ )

$h(x)$  = mean waterdepth (including set-up/set-down)

$k_N$  = bottom roughness according to Nikuradse

The eddy viscosity is estimated by eq. 4.22 using the roller dissipation,  $D_r$ , as input. The latter is computed with a one dimensional wave-propagation model as described in Chapter 4. The measured wave height distribution and set-up are used to calibrate the wave model with respect to the breaker parameters,  $\gamma$  and  $\beta$  (see Chapter 4). The results for  $c_d$  and  $\nu_t$  thus obtained are used as input for the linear stability analysis. Note that the assumptions made for the friction coefficient and eddy viscosity may not be completely accurate. It is therefore expected that small discrepancies between measurements and predictions may occur.

Three different cases are considered in the comparison. The base case is defined by test SA243, with an incident wave height,  $H_i$ , of 8 cm and a wave period,  $T$ , of 1 s. This is followed by a test with an increased incident wave height (test SA337,  $H_i = 10$  cm) and a test where random waves were used (Test SO014,  $H_{rms} = 7$  cm) instead of regular waves. The total gives a good indication of all the test results obtained during the laboratory experiments (see Chapter 2, Table 2.1).

### 5.2.2 Results

In this Chapter the results obtained with the numerical linear stability model are compared with the measurements. The computed instability curve for the base case is shown in the left panel of Figure 5.1. Three conditions are examined for test SA243: without damping effects, bottom friction only and eddy viscosity plus bottom friction respectively. Intercomparison of the instability curves, see left panel of Figure 5.1, shows a significant reduction in the growth rate as the damping is increased. Accordingly the range of unstable wave numbers becomes more narrow. For full damping, i.e. including bottom friction and eddy viscosity, the FGM occurs at  $k_y = 0.85$  (rad/m) with a corresponding growth rate of 0.0065 (rad/s).

The results for the two additional tests show the influence of the changes in velocity shear. For the random wave case, the more gradual wave breaking results in a weaker velocity back shear and corresponding smaller growth rates (compare Figures 2.9 and 2.3) in Chapter 3). The wave number instability range has decreased in width with respect to test SA243. The wave number corresponding to the FGM has moved further toward the lower wave numbers,  $k_y = 0.5$  (rad/m), a decrease of 40% compared with test SA243. Increasing the wave height, test SA337, results in an increased longshore current velocity and corresponding larger back shear (compare Figures 2.5 and 2.3 in Chapter 3). This leads to a stronger growth rate and a wider range of unstable wave numbers. The

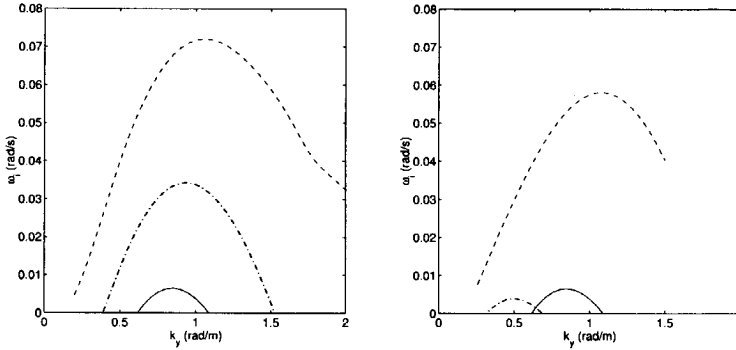


**Figure 5.1:** Left panel: Instability curves for test SA243. Without damping (dashed line), with bottom friction (dash-dotted) and eddy viscosity plus bottom friction (solid line). Right panel: Instability curves for tests SA243 (solid), SA337 (dashed) and SO014 (dash-dotted) with bottom friction and eddy viscosity.

position of the FGM is now located at  $k_y = 1.1$  (rad/m), which is an increase of approximately 30% with respect to test SA243.

The measured position of the FGM for test SA243, located at  $k_y = 0.91$  (rad/m) (see Chapter 3 Table 3.2), corresponds well with the predicted value of  $k_y = 0.85$  (rad/m). For test SA337 the position of the FGM in the measurements is less pronounced than for the base case. The energy density displays a smooth and broad distribution with a peak around  $k_y = 0.75$  (rad/m) with a corresponding frequency of 0.035 Hz (see Figure 3.8 Chapter 3). This is significantly lower than the predicted value  $k_y = 1.1$  (rad/m). In the case of random waves the measured FGM is located at  $k_y = 0.70$  (rad/m) with a corresponding frequency of 0.028 Hz, which is higher than the predicted value of  $k_y = 0.5$  (rad/m).

Figure 5.2 shows the comparison of the computed and measured dispersion relations for the shear instabilities for the three different tests. The computed dispersion relations are shown for the computed wave number instability ranges only. The correspondence is reasonable for the upstream part for tests SA243 and SA337. In the case of random waves, the measurements show spurious energy density, which obscures the shear instability signature in the wave number frequency plot (see upper right panel of Figure 5.2). This is most likely associated with the inflow conditions, the pumped discharge being constant whereas the forcing of the longshore current varies in time and space due to the randomness of the waves. This results in a mismatch with the flow conditions within the basin causing inflow disturbances. At the downstream end the computed wave

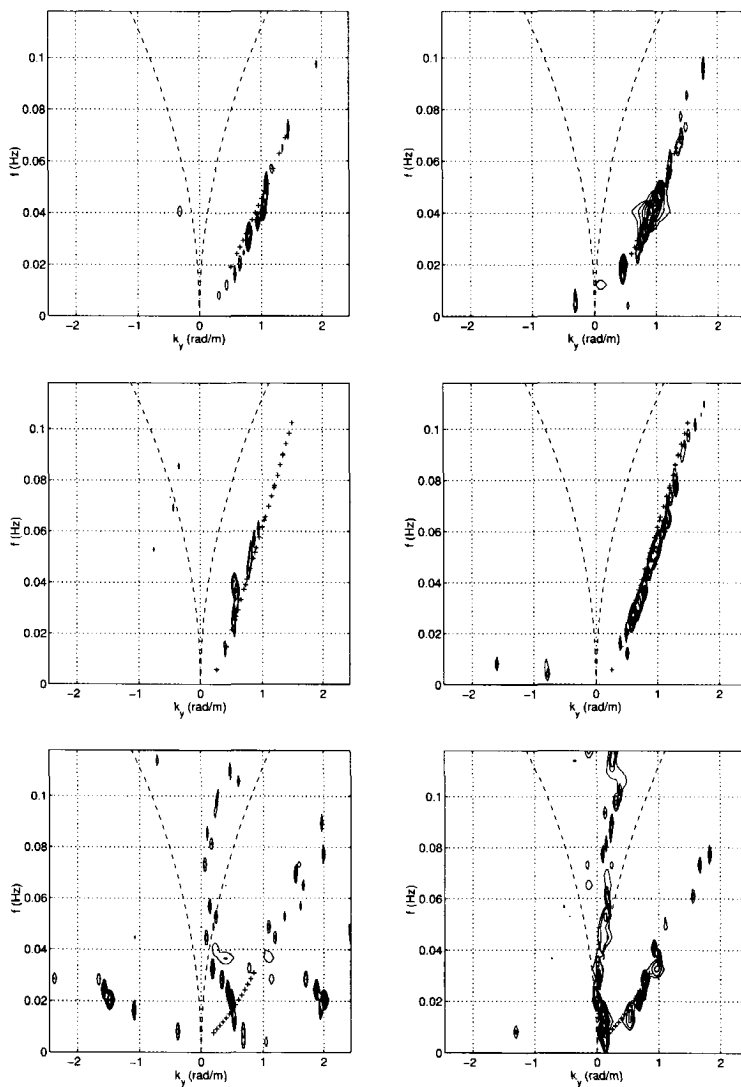


**Figure 5.2:** Left panels: Comparison of measured and computed (denoted by '+' signs) dispersion curves at the upstream (left) and downstream end (right) for tests SA243 (upper panels), SA337 (middle panels) and SO014 (lower panels). Zero mode edge wave dispersion curve depicted as a reference (dashed).

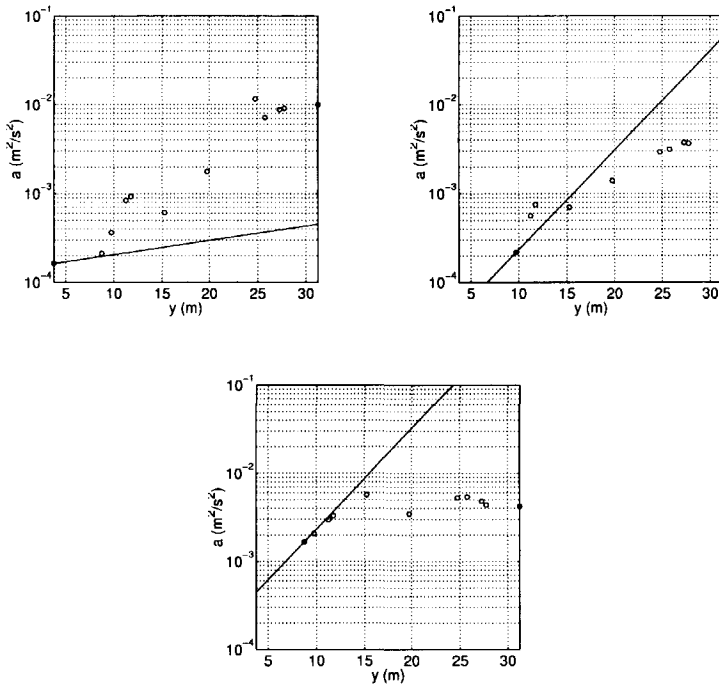


**Figure 5.3:** Alongshore increase of shear instability variance of alongshore velocity in frequency band from 0 to 0.1 Hz (circles) for Test SA243. Computational results (solid line) obtained from linear stability analysis with full damping. Similar results for tests SA337 (right) and SO014 (lower panel)

number range is in very good agreement with the range of wave numbers which contain significant energy for all tests. The shear instability signature for the random wave case (see lower right panel of Figure 5.2), has appeared clearly now, showing wave numbers which are somewhat higher than the prediction.

The overall correspondence is very good even though the observed shear instabilities downstream have a finite amplitude, for which a nonlinear analysis is more appropriate. The good correspondence of measured finite instabilities and predictions based on linear stability analysis was previously obtained by Dodd et al. [1992] for the SUPERDUCK data.

To compare the computed growth with the measured growth, it is assumed



that, given the almost linear dispersion relation, all instabilities propagate with the same speed (see Appendix A). Given the distance between the various measuring points, the time which the instabilities take to propagate from one point to another can be calculated. A first estimate of the predicted growth is then obtained by:

$$a(y) = a_0 \exp\left(2\omega_i \frac{y - y_0}{c}\right) \quad (5.7)$$

where  $a$  represents the variance present between 0 Hz and 0.1 Hz associated with the shear instabilities,  $\omega_i$  the growth rate,  $y$  the distance with respect to the inflow opening and  $c$  represents the propagation speed of the shear instabilities; the subscript 0 indicates the initial values at  $y = y_0 = 3.75m$ . The propagation speed is estimated at 0.35 (m/s), 0.45 (m/s) and 0.30 (m/s) for tests SA243, SA337 and SO014 respectively (see Table 3.2 in Chapter 3). In most of the experiments the energy density present in the frequency range mentioned is associated with shear instabilities only and a straightforward integration can be applied to obtain the alongshore growth. This is not the case for random waves, where the energy density in the low-frequency range is associated with low frequency gravity waves as well. Assuming homogeneous conditions for these low frequency waves an estimate of the growth rate is obtained by subtracting the energy present at the first measuring point from the integrated energy density at all other measuring points.

In Figure 5.3 the observed spatial growth is compared with the predicted growth for the FGM (see Figure 5.1) taking into account bottom friction and eddy viscosity; the growth rate is significantly underpredicted for test SA243. For test SA337 the computational results show an overprediction of the growth rate, though the mismatch is smaller. These results are remarkable given the fact that in both cases the range of unstable wave numbers is predicted so well. In the random wave case there is an initial exponential growth, which is matched closely by the predictions, up to the middle of the basin after which the observed growth rate levels off, indicating an equilibrium. The results indicate that the present modelling of the dissipative effects due to bottom friction and eddy viscosity is not adequate for an accurate prediction of the growth rate.

### 5.3 Non-linear modelling

In the following the results obtained from a non-linear model to compute the mean flow characteristics as well as the generation and growth of shear instabilities are compared with the measurements. This approach corresponds closely

with the experimental set-up, modelling the spatial development of the flow dynamics as opposed to the temporal modelling used in the linear stability analysis.

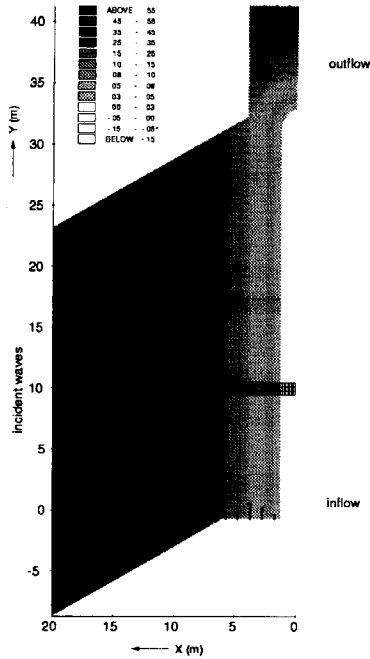


Figure 5.4: Model definition and bathymetry

The wave transformation equations have been described in Chapter 4 (see eqs. 4.1 to 4.7). Given the monochromatic wave conditions for most of the experiments the following wave dissipation formulation has been used in the wave modelling (Roelvink, 1993):

$$D_w = 2\alpha f_p (1 - e^{-\left(\frac{H}{\gamma h}\right)^n}) E_w \quad (5.8)$$

where  $\alpha$ ,  $n$  and  $\gamma$  are the breaker parameters and  $f_p$  the peak frequency and  $H$  the wave height. For high values of  $n$  the dissipation formulation corresponds to monochromatic wave breaking whereas for lower  $n$ -values random wave dissipation is approximated (Roelvink, 1993). Again the wave energy dissipation serves as input in the balance for the roller energy (eq. 4.8).

The model domain is shown in Figure 5.4. The cross-shore grid spacing varies from 0.5 m offshore to .15 m in the surfzone. In the alongshore direction the grid spacing is equidistant with a mesh size of .35 m. The simulated time was 45 minutes of which the final 30 minutes were used for the analysis. Time steps varied from 0.3 to 0.9 seconds. The bathymetry is also shown in Figure 5.4, where the bar crest and trough can be recognised by the sequence of dark and light shades. At the downstream end the bottom profile curves around to obtain a smooth transition toward deeper water, which is slightly different from the physical model where a steeper slope at the downstream end was used. The oblique side boundaries of the numerical model correspond with the wave guides in the physical model. The up-wave boundary corresponds to  $x=20$  in Figure 5.4. The incident wave energy,  $E_w$ , is introduced at the up-wave boundary. Inside the computational domain the propagation is governed by the precalculated wave incidence angle,  $\theta$ , and group velocity,  $c_g$ , based on a bottom refraction model. Current refraction is not taken into account.

The velocity field, driven by the wave forcing, is modelled with a modified version of the non-linear shallow water equations as described in Chapter 4. The cross-shore momentum balance is now given by:

$$\frac{\partial u}{\partial t} + u \frac{\partial u}{\partial x} + v \frac{\partial u}{\partial y} = -F_x - g \frac{\partial \zeta}{\partial x} + \nu_t \left( \frac{\partial^2 u}{\partial x^2} + \frac{\partial^2 u}{\partial y^2} \right) - \tau_x \quad (5.9)$$

and the alongshore momentum equation is given by:

$$\frac{\partial v}{\partial t} + u \frac{\partial v}{\partial x} + v \frac{\partial v}{\partial y} = -F_y - g \frac{\partial \zeta}{\partial y} + \nu_t \left( \frac{\partial^2 v}{\partial x^2} + \frac{\partial^2 v}{\partial y^2} \right) - \tau_y \quad (5.10)$$

where in the computation of the lateral mixing the cross-shore gradient of the eddy viscosity is no longer taken into account. This difference in modelling the lateral mixing proved to be essential in the modelling of the wave-driven longshore current for the random wave case. In that case the computed longshore current velocity profile could no longer be made to match the measured cross-shore distribution up to a sufficient degree. Given the fact that the evolution of the shear instabilities strongly depends on the longshore current velocity profile, a comparison with measurements is no longer useful and for this reason the random wave case, SO014, is not taken into account in the following.

The bottom shear stress is computed using the parametrisation of Soulsby et al. [1993] of the friction model of Bijker [1967]. The bottom roughness is used as a fit-parameter to obtain a good correspondence between measured and computed longshore current velocities and resulting generation and growth of shear instabilities in the velocity field. The measured alongshore flow velocities are prescribed at the inflow opening obtained from the measurements (see Figure 5.4), whereas at the outflow opening a constant zero water level has been

used. This is different from the actual experimental set-up where a constant pumped discharge was used. A no-flux boundary condition is used elsewhere. The coupled differential equations for the wave energy, roller energy and cross-shore and alongshore momentum are solved numerically (Petit, 1997).

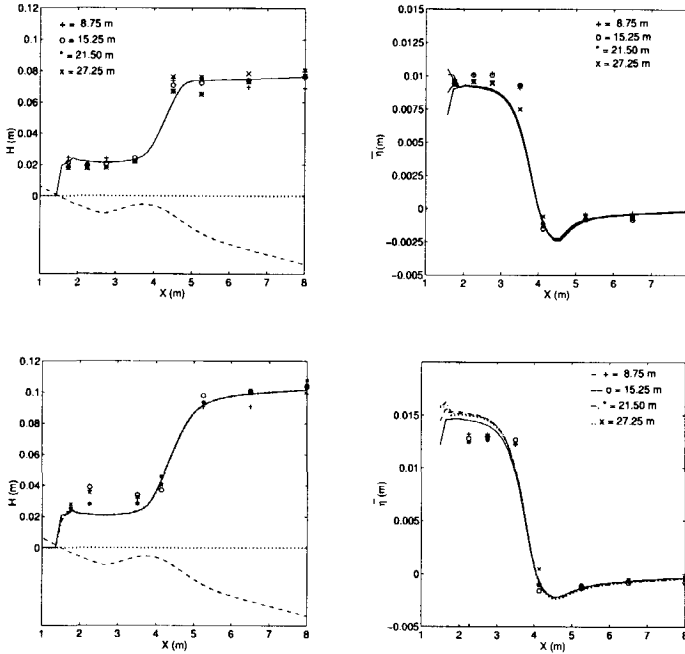


**Figure 5.5:** *Upper left panel: Comparison of computed wave transformation with measurements, test SA243. Computational results obtained for  $\alpha = 1$ ,  $\gamma = .55$  and  $n = 10$ . Upper right panel: Comparison of computed wave set-up for  $\beta = .1$  and measurements, test SA243. Similar for test SA337 (lower panels).*

The breaker coefficients associated with the wave model are calibrated using the measured cross-shore distribution of the wave height and set-up analogous to the 1D-case described in Chapter 4. The results (see Figure 5.5) show that the computed wave height for test SA243 corresponds well with the measurements. There is no alongshore variation in the computed wave height distribution. This is in contrast to the measurements where small differences in wave height are bound to occur due to (partial) reflections, wave current interaction, small differences in bathymetry, etc.

The computed set-up, obtained for  $\beta = 0.1$ , is shown in the right panel of Figure 5.5. The agreement between computations and measurements is good, though the measured maximum set-up is underestimated by  $O(10\%)$ . The final wet point shows some small wiggles associated with numerical accuracy. These are not believed to have an effect on the flow characteristics within the computational domain. Keeping the wave breaking parameters at its present values, the results for test SA337 are shown in the lower panels of Figure 5.5. The overall correspondence with the measurements is good, with in this case a slight overestimation of the maximum set-up values near the water line.

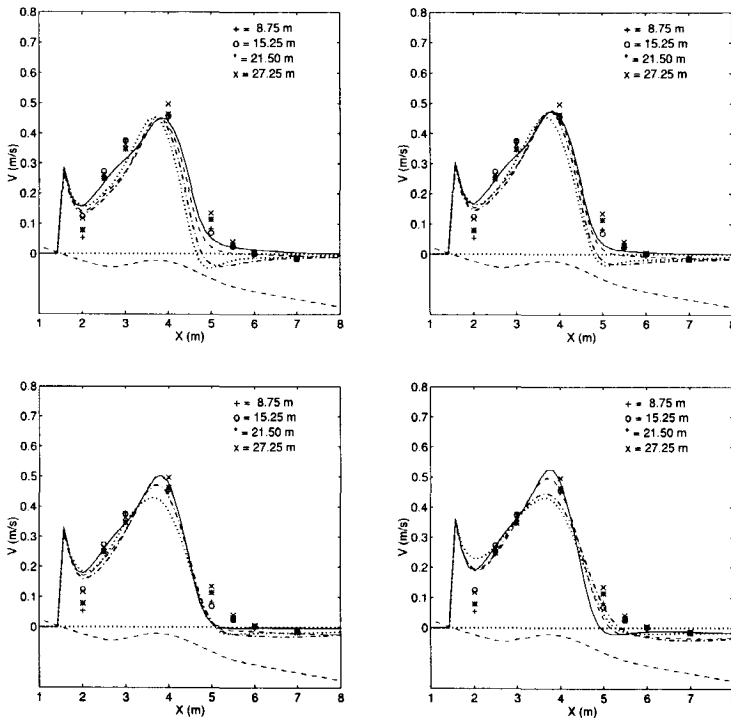


**Figure 5.6:** Mean longshore current velocity profiles obtained for a bottom roughness of  $k_N = 0.005$  m (upper left),  $k_N = 0.004$  m (upper right),  $k_N = 0.003$  m (lower left) and  $k_N = 0.002$  m (lower right) at various transects.

To calibrate the flow model the Nikuradse roughness length,  $k_N$ , is varied, with the objective to obtain a good match with the measured cross-shore distribution of the longshore current. A number of roughness values have been

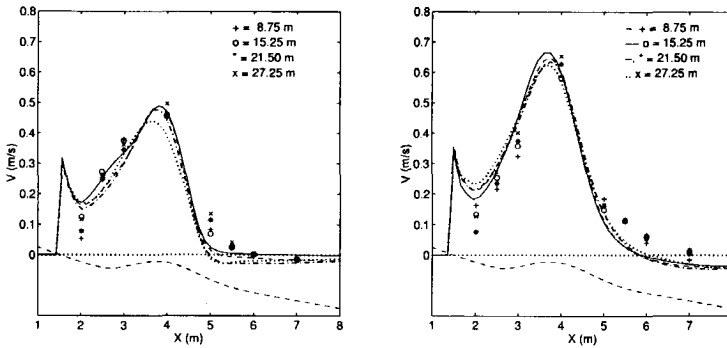


**Figure 5.7:** Comparison of mean longshore current profiles. Computations at 8.75 m (solid), 15.05 (dashed), 21.35 (dash-dotted) and 26.95 m (dotted line) obtained with  $k_N = 0.0035$  m for tests SA243 (left panel) and SA337 (right panel). Bottom profile shown as reference (lower dashed line)

applied, ranging from 0.002 m to 0.005 m for which the mean longshore current velocity distribution is compared to the measurements (see Figure 5.6). Overall the comparison shows good quantitative agreement. The velocity maximum is located near the bar crest and significant flow velocities are present in the trough. For decreasing bed roughness the maximum longshore current velocity increases, though only with small increments up to 15% for the range of roughness used.

A closer examination reveals some qualitative differences between the various computational results. Using a bed roughness of  $k_N = 0.005$  m (see upper left panel of Figure 5.6), results in an alongshore decrease of the longshore current velocity in the region of high backshear (near  $X = 5$  m), indicating a mismatch between the inflow velocity (i.e. comparable to a too large pumped discharge in the experimental model) and the wave-driven longshore current. Decreasing the roughness down to a  $k_N$  value of 0.003 m minimises this mismatch. A further reduction of  $k_N$  to a value of 0.002 m results in an alongshore increase in the longshore current velocity (see lower right panel Figure 5.6), where the discharge at the inflow is now too small compared to the waved-driven longshore current discharge.

It is noted that the computational longshore current velocity profile near the inflow has an optimal match with the measurements for higher roughness (compare the back shear obtained for a  $k_N$  value of 0.005 m and 0.003 m). Still, the alongshore behaviour of the mean longshore current is much better for the lower roughness, corresponding to a balance between the forcing, friction and

inflow conditions analogous to the measurements. This implies however that the backshear is overestimated compared to the measurements. This is expected to result in a higher growth rate than predicted by linear stability analysis.

The best match is obtained for a  $k_N$  value of 0.0035 m. The comparison between computed and measured mean longshore current for this value of  $k_N$  is shown in the left panel of Figure 5.7. The overall correspondence is good, showing strong velocities near the bar crest. Looking in detail shows that the back shear is overestimated with  $O(10\%)$  compared to the measurements. A second peak at the water line is present in the computations in a region where there are no measurements (because of depth limitations). A visual check using dye confirmed the existence of a second peak during the experiment, though no quantitative information on the velocities was obtained.

The measured alongshore changes in the mean longshore current velocity are small. This is also true for most of the computed velocity profiles. Only the velocity profile nearest to the outflow opening has become slightly smoother. Similar results are obtained for test SA337. Again a good match with the measurements is obtained, with strong velocities near the bar crest. The back shear is also slightly overpredicted.

Next we examine whether the computed flow for test SA243 exhibits similar behaviour regarding the generation and growth of shear instabilities as observed in the measurements. To visualise the generation of the shear instabilities the potential vorticity, given by:

$$\Omega = \frac{\frac{\partial v}{\partial x} - \frac{\partial u}{\partial y}}{h} \quad (5.11)$$

is shown in the upper panel of Figure 5.8. This shows some small adjustments occurring near the inflow, where the flow velocities prescribed at the boundary adjust to the wave-driven longshore current. Up to the middle of the basin ( $y = 15$  m) the flow is approximately alongshore uniform, after which the first indication of a slow oscillation becomes apparent. This disturbance increases in amplitude as the flow reaches the downstream end of the basin until the deeper part at the outflow has been reached. The estimated wave length is  $O(7)$  m. For test SA337, the resulting changes in the relative potential vorticity are much smaller. This is interesting, given the fact that the predicted growth rates are significantly higher than for test SA243. However, it is in line with the measured alongshore growth which is smaller than measured during test SA243.

Using the same spectral analysis technique as described in Chapter 3, the frequency- alongshore wave number signature of the computed shear instabilities can be determined. This analysis is performed on the alongshore velocities at the downstream end of the basin at an offshore distance  $x = 4.25$  m, analogous to the measurements. The comparison for test SA243 is shown in the left panels of Figure 5.9. The measurements show a relatively broad, approximately linear,

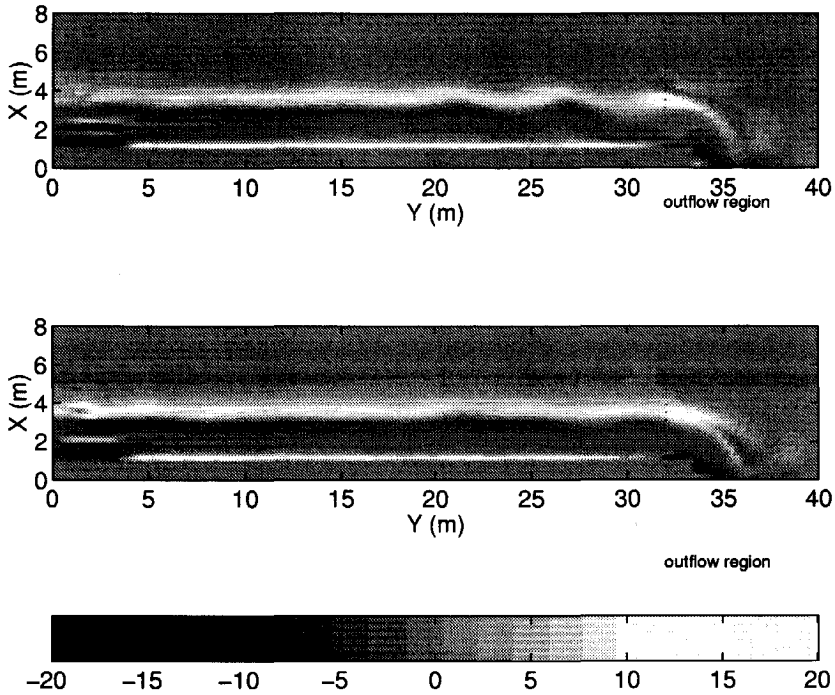


**Figure 5.8:** Upper panel: Snapshot of alongshore development of computed potential vorticity for test SA243. Similar for test SA337 (lower panel). Potential vorticity  $\Omega$  expressed in  $(ms)^{-1}$

distribution of the energy density with an estimated propagation speed,  $c$ , in the order of 35 cm/s. The peak of the spectrum is located at  $k_y = .91$  rad/m with a frequency of .0407 Hz. In contrast, the computations display a narrow distribution. Still, the spectral peak is located at  $k_y = .98$  rad/m, with a corresponding wave length of 6.4 m, and a frequency of 0.0366 Hz which compares fairly well with the observed spectral peak from the measurements. Similar narrow distributions of the computed spectral density were present for all friction factors and time steps used.

The comparison for test SA337 is shown in the right panels of Figure 5.9. In this case both measurements and computations show a broader distribution of the energy density, though the computed range is still smaller than obtained



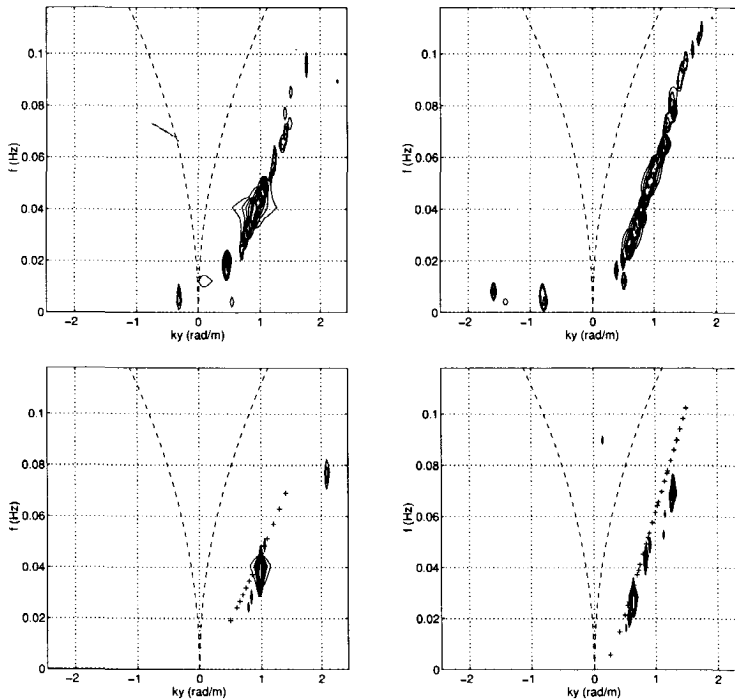


**Figure 5.9:** Measured (upper panels) and computed (lower panels) dispersion curves based on linear stability analysis (indicated by '+') and non-linear modelling for tests SA243 (left) and SA337 (right). Zero-mode edge wave dispersion lines indicated by dashed lines.

from the measurements. The peak in the computed energy density distribution is also more pronounced than in the measurements. It is located at alongshore wavenumber  $k_y = 0.64$  rad/m with a frequency of 0.028 Hz, which is more in line with the measurements,  $k_y = 0.75$  rad/m with a frequency of 0.035 Hz, than the results obtained from the linear stability analysis,  $k_y = 1.1$  rad/m with a frequency of 0.065 Hz. Both dispersion curves, i.e. obtained from the linear stability analysis and non-linear modelling, follow the measurements closely.

To compare the alongshore development of the shear instabilities, the contribution to the variance in the low-frequency range between 0.0 and 0.1 Hz, denoted by  $a$ , is plotted as function of the alongshore position of the current velocity meters both for computations and measurements. A clear exponen-

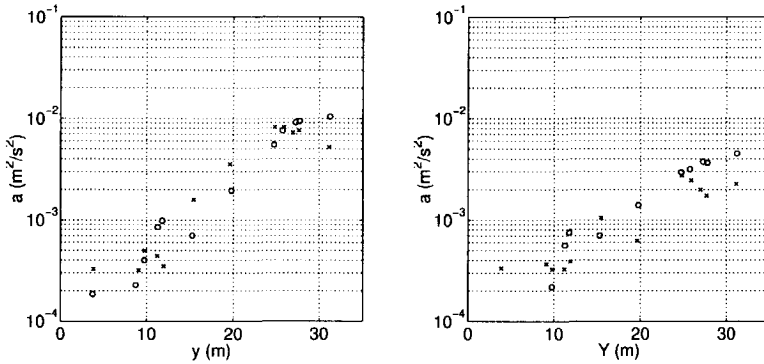


**Figure 5.10:** Alongshore development of integrated spectral density based on the alongshore shear instability velocities for test SA243 (left) and test SA337 (right). Computed results, obtained with  $k_N = 0.0035$  m, indicated by crosses vs. measurements indicated by circles.

tial growth along the beach can be observed for test SA243 (see left panel of Figure 5.10). The computed growth rate and the total variance reached at the downstream end obtained for the alongshore velocities are in fair agreement with the measurements. There is no clear indication that an equilibrium is reached at the downstream end of the basin, though both measurements and computations suggest a levelling off at the downstream end of the basin. This will be examined further in Chapter 6 using an extended numerical domain.

The results obtained for test SA337 are similar to the base case (see right panel of Figure 5.10). Again a fair agreement between the computed and measured alongshore development of the shear instability energy is obtained. Differences between computed and measured integrated spectral density occur at the downstream end, most likely associated with the differences in the computational and experimental bottom profile.

## 5.4 Discussion

The computed alongshore growth rate of the shear instabilities obtained from non-linear numerical modelling showed good agreement with the measurements. This is in contrast to the results obtained with the linear stability analysis, where significant differences were obtained. At this point it is not clear why this is the case.

$y'$	.50	1.17	1.30	1.50	1.57	2.03
$U'$	.15	.11	.11	.17	.14	.15
$y'$	2.63	3.3	3.43	3.63	3.70	4.17
$U'$	.25	.33	.35	.55	.53	.58

**Table 5.1:** Relative intensity of instabilities with respect to the incident waves, expressed in root mean square velocity ratio  $U' = U_{rms,lo}/U_{rms,hi}$ , as a function of normalised alongshore distance,  $y' = y/L_p$ , where  $L_p$  represents the instability peak-wave length of 7.5 m; the pass frequency was set at 0.5 Hz and  $U_{rms,hi}$  is  $O(.25)$  m/s.

As mentioned previously, the theoretical background for the presence of shear instabilities in the wave-driven longshore current was given by Bowen and Holman [1989]. Based on their analysis, they stated that the presence of shear instabilities is expected to have a significant influence on the resulting mean longshore current velocity profiles. The idea is that the presence of shear instabilities leads to a cross-shore transfer of momentum, resulting in a smoothing of the velocity profile. This effect is not apparent in the computed and measured longshore current velocity profiles, though the shear instabilities have reached finite amplitude values. The fact that the expected smoothing of the velocity profiles is not present could be due to the limited length of the basin, i.e. the shear instabilities have not reached sufficient values at the downstream end (i.e. too small to have a noticeable effect on the lateral mixing). However, the observations show shear instability velocities which are of the same order as the incident waves (see Table 5.1). This paradox of cross-shore momentum transfer and the absence of the associated changes in the mean longshore current velocity profile as the shear instabilities reach finite amplitude values will be examined in the following Chapter.

## 5.5 Conclusions

A comparison between measurements and computational results obtained from linear and non-linear modelling has been performed. In general the correspondence between computations and measurements is good. This is especially so for the frequency-alongshore wave number signatures of the shear instabilities, implicating a good match of the computed and measured phase speeds. Significant differences occur in the prediction of the alongshore growth of the shear instabilities. The linear stability model results show a mismatch between the predicted and measured growth rates for tests SA243 and SA337 respectively which is not present in the non-linear model results where the total energy reached at the

downstream end is in fair agreement with the measurements.

# Chapter 6

## Effects of instabilities on the longshore current

### 6.1 Introduction

In the preceding Chapter we have seen no clear evidence of interaction between the finite amplitude shear instabilities and the wave-driven longshore current. Still, the presence of shear instabilities is expected to result in cross-shore momentum transfer thereby influencing the underlying longshore current. This was put forward by Bowen and Holman based on their linear stability analysis. This potential for momentum transfer, often referred to as mixing, has been assessed by a number of other authors (Dodd and Thornton, 1990, Putrevu and Svendsen, 1992, Church et al., 1992), suggesting that the shear instabilities could result in a different longshore current velocity profile from the initial profile. More detailed numerical analyses were made using weakly non-linear (Dodd and Thornton, 1992) and fully non-linear models (Nadaoka and Yagi, 1995, Deigaard et al., 1994, Allen et al., 1995, Özkan and Kirby, 1995, Özkan-Haller and Kirby, 1996 and 1997, Slinn et al., 1998) to describe the development of shear instabilities in wave-driven longshore currents. These studies confirmed the expected momentum transfer, resulting in a smoothing of the initial longshore current velocity profile.

The aim of the present Chapter is to make a quantitative analysis of the effect of shear instabilities on the cross-shore distribution of the longshore current. To that end the phase coupling between the measured  $u$  and  $v$  velocity components is examined in detail using cross-shore spectral analysis to compute the frequency distribution of the momentum flux induced by shear instabilities. The total transfer is then obtained by integration over the frequency domain. The results are compared to the other terms in the longshore momentum equation used to compute the longshore current velocity.

Next the calibrated numerical model representing the laboratory basin as described in the previous Chapter, is extended with respect to the original basin length to examine the further development of the shear instabilities and longshore current profile as they reach equilibrium conditions.

Parts of this chapter have been published in Reniers and Battjes [1997].

## 6.2 Spatial structure

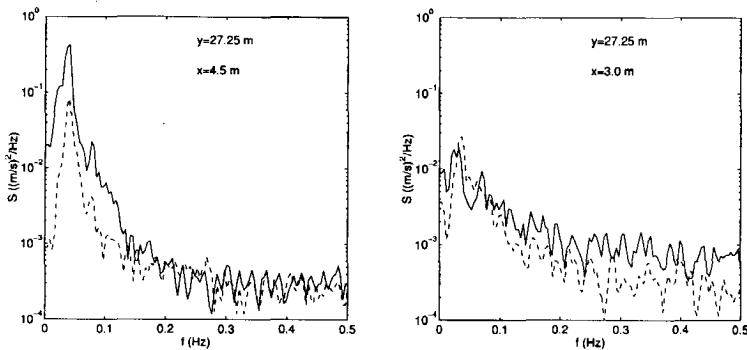


**Figure 6.1:** Left panel: Energy density of  $u$  (dashed line) and  $v$  (solid line). Left panel:  $x = 4.5$  m and  $y = 27.25$  m. Right panel:  $x = 3.0$  m and  $y = 27.25$  m.

During test SA243, see Chapter 2, the cross-shore position of the two alongshore arrays was varied to examine the alongshore development of the shear instability cross-shore structure. Spectral analyses based on the maximum entropy method showed that for all cross-shore positions the energy density in the low-frequency band,  $f < 0.1$  Hz, corresponded to shear instabilities only. Therefore some of the cross-shore structure already becomes evident from the spectral densities shown in Figure 6.1. At 27.25 m downstream from the inflow opening the measured energy density of  $u$  and  $v$  is shown in Figure 6.1 at the cross-shore positions  $X = 4.5$  m and  $X = 3.0$  m respectively. Offshore of the bar crest (left panel of Figure 6.1) the alongshore velocity,  $v$ , clearly dominates the cross-shore component,  $u$ . In the trough (right panel Figure 6.1) however they are of equal, though smaller magnitude.

More detailed information can be obtained by plotting the variance for each frequency band as a function of the cross-shore distance. From the spectral analysis it follows that the spectral peak is located at approximately 0.04 Hz (see

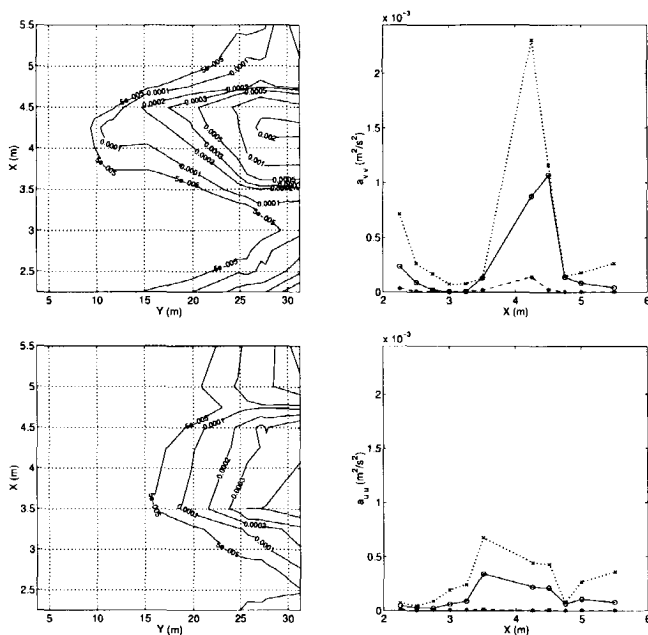


**Figure 6.2:** Left panels: Contours of variance of  $v$  (upper) and  $u$  (lower) developing along the beach in the band  $f = 0.0407 \text{ Hz} \pm 0.00205 \text{ Hz}$ . Right panels: Cross-sections of this variance at  $y = 11.25 \text{ m}$  (dashed),  $y = 24.75 \text{ m}$  (solid) and  $y = 31.25 \text{ m}$  (dotted) respectively. Measurements indicated by the markers. Test SA243.

Figure 6.1). The spatial structure for the corresponding frequency band ( $0.0407 \text{ Hz} \pm 0.00205 \text{ Hz}$ ) is visualised by the variance contours, shown in Figure 6.2, for the  $v$  (upper left panel) and  $u$  (lower left panel) components respectively. Given the fact that the shear instability intensity increases downstream, the spatial structure also evolves in the downstream direction. Upstream the variance is concentrated around the maximum back shear. Further downstream the  $v$ -variance in the trough picks up, seemingly developing separately from what is happening at the maximum back shear. This could indicate the existence of a second mode (Putrevu and Svendsen, 1992). Applying a  $f$ - $k_y$ -analysis on the longshore current velocities in the trough showed that this is not the case. Looking at the contour lines of equal variance in the vicinity of the maximum back shear the  $v$ -component apparently reaches an equilibrium at the downstream end, whereas

the  $u$ -component still increases in intensity.

The cross-sections, see right panels of Figure 6.2, show that at the position of the maximum longshore current shear,  $X = 4.25$  m, the variance of  $v$  is approximately five times that of  $u$ . In the trough ( $X = 3.0$  m) the variance of  $u$  and  $v$  are of equal order, though both are small compared to the variance of  $v$  at the offshore position. At the shoreline the image reverses again, with the variance of  $v$  reaching approximately half of its maximum value. In both the cross-shore and alongshore direction there are strong gradients associated with the shear instability velocities. In fact, the cross-shore resolution may be inadequate to fully reflect the spatial structure, for instance between 3.75 m and 4.5 m. This is where wave breaking is most intense and therefore the local velocities could not be measured.

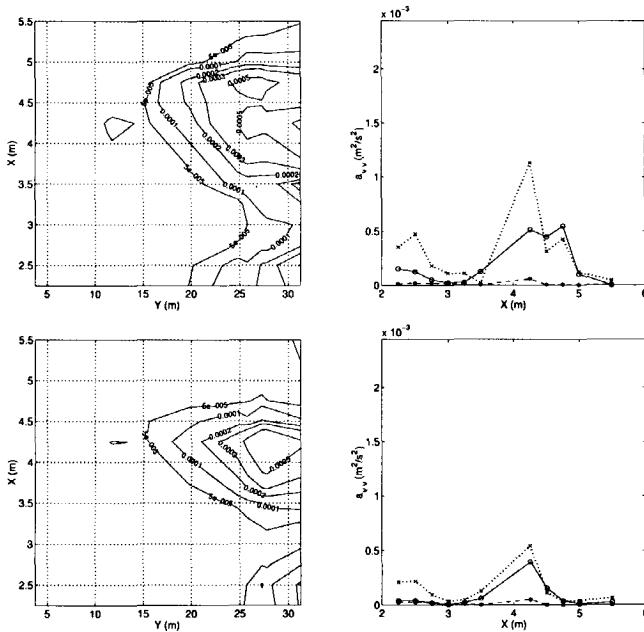


**Figure 6.3:** Left panels: Contours of variance of  $v$  developing along the beach in the bands  $f = 0.028 \text{ Hz} \pm 0.00205 \text{ Hz}$  (upper) and  $f = 0.048 \text{ Hz} \pm 0.00205 \text{ Hz}$  (lower panel). Right panels: Corresponding cross-sections of this variance at  $y = 11.25$  m (dashed),  $y = 24.75$  m (solid) and  $y = 31.25$  m (dotted) respectively. Test SA243.



For lower frequencies, as shown in the upper panel of Figure 6.3 for a frequency bin of 0.028 Hz  $\pm$  0.00205 Hz, the variance of  $v$  is still increasing at the downstream end. Whether or not equilibrium conditions are obtained is a function of growthrate and the number of cycles before the downstream end is reached. Given the shorter spatial scales for the higher frequencies, these will reach equilibrium sooner than the low-frequency oscillations. This can be seen for a higher frequency bin of 0.048 Hz  $\pm$  0.00205 Hz, where equilibrium for the variance of  $v$  has indeed been reached (see lower panels of Figure 6.3). Hence the total shear instability equilibrium conditions were not obtained during the present set of measurements.

### 6.3 Cross-shore momentum flux

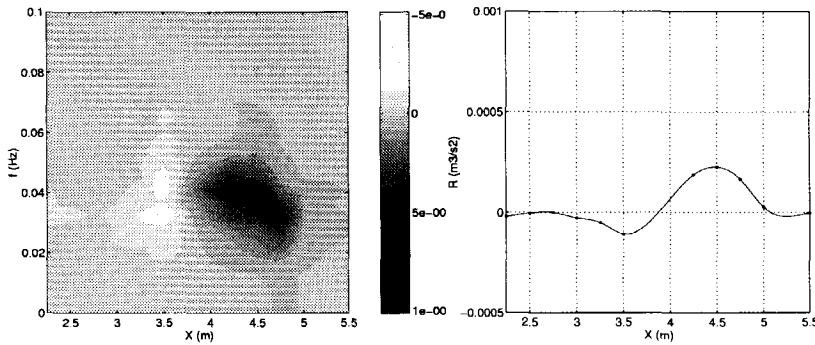


**Figure 6.4:** Left panel: Frequency distribution of shear instability momentum flux,  $R'$ , at 27.25 m from the inflow opening expressed in  $\frac{m^3}{s^2}/\text{Hz}$ . Right panel: Frequency integrated momentum flux at same position.

The momentum flux induced by the shear instabilities at the cross-shore measurement locations, denoted by the subscript  $i$ , in a single transect may be obtained from:

$$R(x_i) = \rho d(x_i) \langle u(x_i, t)v(x_i, t) \rangle \quad (6.1)$$

with  $u$  and  $v$  being the cross-shore and alongshore velocities associated with the shear instabilities,  $\langle \rangle$  denotes time averaging,  $d$  the local water depth and  $\rho$  the water density. The resulting flux depends on the spatial structure, mentioned in the previous paragraph, and the phase coupling between the velocity components.

First we have a closer look at the frequency distribution of the momentum flux associated with the shear instabilities using cross-spectral analysis. To that end the velocity time series are written in Fourier series:

$$u(x_i, t) = \sum_n A_n e^{if_n t} + * \quad (6.2)$$

$$v(x_i, t) = \sum_n B_n e^{if_n t} + * \quad (6.3)$$

The momentum flux as function of frequency can then be obtained from the co-spectral values:

$$R'(x_i, f_n) = d(x_i)(A_n B_n^* + A_n^* B_n) \delta f \quad (6.4)$$

The results for the frequency dependent momentum flux at 27.25 m from the inflow opening is shown in the left panel of Figure 6.4. The intermediate values have been obtained from linear interpolation in frequency and space. The flux is spatially concentrated at both sides of the bar crest ( $x \simeq 3.75$  m), with maximum contributions around the peak shear instability frequency. At the shoreward side of the bar crest ( $x < 3.75$  m) the momentum flux seems to be bimodal in frequency space. The frequency where the maximum flux is located decreases with increasing  $x$ -values, i.e. going further offshore, indicating that the higher frequencies, having smaller spatial scales, contribute less. Integrating the momentum flux over frequency gives the total contribution to the cross-shore momentum flux shown in the right panel of Figure 6.4.

## 6.4 Importance in longshore current modelling

For alongshore uniform steady state conditions the wave averaged longshore momentum equation is given by:

$$\frac{dS_{xy}}{dx} = \tau_{y,b} \quad (6.5)$$

with the following contributions to the term on the left-hand side due to waves:

$$\frac{d}{dx} \rho \int_d \overline{u'v'} dz \quad (6.6)$$

turbulence:

$$\frac{d}{dx} \rho \int_d \overline{u'v'} dz = \rho \frac{d}{dx} \left( d\nu_t \frac{dV}{dx} \right) \quad (6.7)$$

and shear instabilities:

$$\frac{d}{dx} \rho \int_d \overline{uv} dz \tag{6.8}$$

which are balanced by the alongshore directed wave-averaged bottom shear stress given by the term on the right hand side. In the following the shear instability contribution is compared to the other components in the longshore momentum equation.

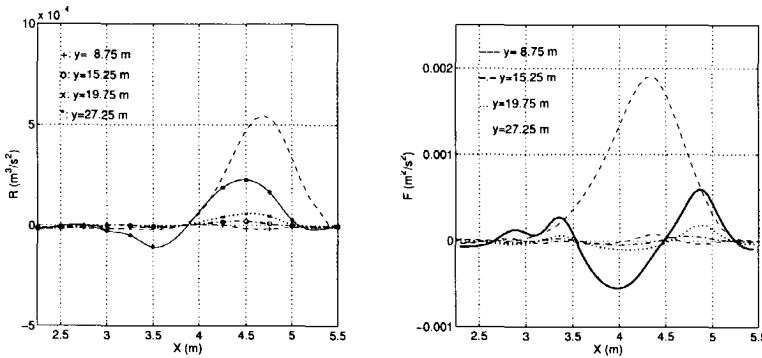


**Figure 6.5:** Alongshore development of integrated momentum transfer induced by shear instabilities (left panel) and corresponding forcing (right panel). Distance to the inflow opening given by  $y$ . Measurements (markers) connected by a spline. Estimated lateral mixing (left panel) and wave forcing (right panel) given as a reference (dashed line).

The total momentum flux due to the shear instabilities is shown in the left panel of Figure 6.5. It shows the measured flux, indicated by the markers, through which a spline has been fitted, in comparison to the horizontal mixing induced by wave breaking turbulence which is estimated from the measurements in the following way:

$$R_{\nu_t}(x) = d(x)\nu_t(x) \frac{dV}{dx} \tag{6.9}$$

using the measured longshore current velocity,  $V$  and the measured wave height,  $H$ , as input. The turbulent eddy viscosity,  $\nu_t$ , is obtained from eq. 4.22 where in this case the estimated wave dissipation is obtained from the measured wave

transformation. A significant contribution of the shear instabilities to the momentum flux is present at 27.25 m from the inflow opening (see left panel Figure 6.5), though almost everywhere smaller than the estimated horizontal mixing due to turbulence. The cross-shore profile of the momentum flux induced by the shear instabilities is not unlike results obtained from linear stability results (Church et al., 1992), though in this case the contribution in the trough seems to be considerably less.

Given the fact that the shear instability intensity increases in the downstream direction, the corresponding flux also evolves in this direction, which is apparent from the sequence of cross-sections shown in Figure 6.5. At the upstream end of the basin little evidence of additional mixing is available. It takes until EMF07, located 19.75 m from the inflow opening, for the cross-shore momentum flux by shear instabilities to become evident. After that a strong build-up is apparent, though never reaching values as indicated by the wave-breaking induced horizontal mixing. Note that the contribution in the trough stays small all along the beach.

Next we have a look at the cross-shore gradient of the mixing, based on the measured cross-shore momentum transfer, which contributes to the longshore momentum equation in forcing the longshore current velocity profile:

$$F = \frac{dR}{dx} \quad (6.10)$$

The alongshore directed wave forcing, estimated from the measurements, is used as a reference:

$$F_w = \frac{dE_w \sin(\theta) \cos(\theta)}{dx} \quad (6.11)$$

where  $E_w$  represents the wave energy (obtained from the measured wave transformation) and  $\theta$  the angle of incidence (using Snell's law). The results at 27.25 m from the inflow opening, see right panel of Figure 6.5, indicate a significant contribution to the longshore momentum balance at this location. Based on this, it is expected that the maximum current velocity will decrease, given the opposite signs of the contribution by the shear instabilities and wave forcing at the bar crest. Furthermore, the shear instability contribution at the seaward side of the bar indicates a broadening of the longshore current velocity.

The alongshore development of the shear instability contribution to the longshore momentum (see also right panel of Figure 6.5) is in line with the results previously shown for the momentum flux. In all cases the contribution is considerably smaller than the alongshore directed wave forcing. It is worth to note that

the development of the shear instability contribution to the longshore momentum balance stays small in the trough.

Remembering the alongshore development of the longshore current velocity (see e.g. left panel of Figure 5.7) we have seen no clear evidence of the effects of the shear instability induced cross-shore mixing on the alongshore development of the mean longshore current velocity profile, neither in the measurements nor in the computations. At this point the experimental results give no further information. However, in the previous Chapter the measurements have been used to calibrate and verify a numerical model to compute the alongshore development of the shear instabilities. It is possible to extend the numerical model domain to examine any changes in the mean longshore current which may have occurred beyond the outflow opening of the laboratory model.

## 6.5 Equilibrium conditions

In the following the calibrated numerical model is applied in a domain extended to approximately four times its original length to examine the alongshore development of the modelled shear instabilities and corresponding mean longshore current toward equilibrium conditions.

Prior to that we have a closer look at the modelled cross-shore momentum transfer in comparison to the measurements. A sequence of 50 snapshots of the computed velocity field with a time interval of 18 s has been used to compute the cross-shore momentum transfer associated with the shear instabilities analogous to eq. 6.1. A synoptic view of the cross-shore mixing is shown in upper panel of Figure 6.6. Similar to the measurements there are some small adjustments near the inflow opening. After that the contribution to the cross-shore momentum transfer is negligible up to approximately 20 m downstream of the inflow opening. At that point there is significant increase of the momentum transfer visible. Closer to the outflow, after approximately 30 m, a shoreward shift of the maximum transfer can be observed. The computed cross-shore distribution of the momentum transfer at various cross-sections is shown in the lower panels of Figure 6.6 where the measured results have been shown again for easy reference.

There is good qualitative agreement between the measured and computed results. Both show a slow alongshore development for the first 20 m of the basin. After that a strong increase of the cross-shore mixing can be observed reaching similar quantitative levels further downstream. Differences do occur, the computed momentum transfer being shifted approximately 0.5 m closer to the shore compared to the measurements, which is in correspondence with the earlier observed difference in the computed and measured position of the maximum backshear (see Figure 5.7). Still in the region of interest, i.e. up to the

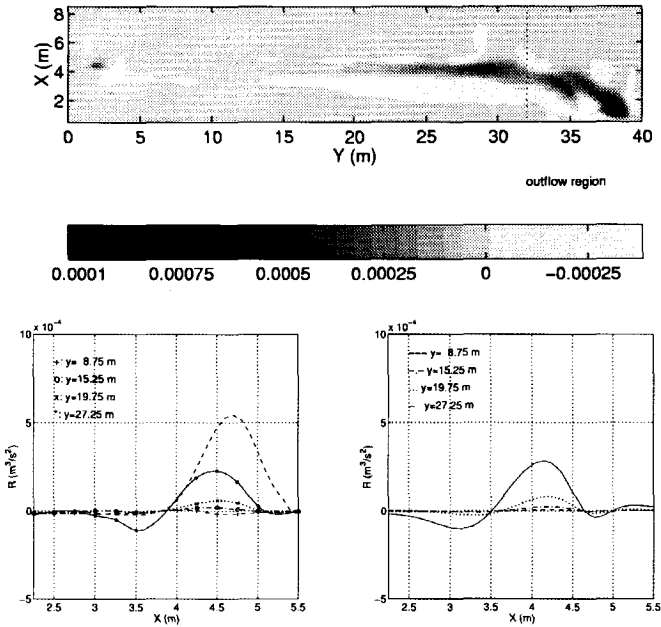


**Figure 6.6:** Upper panel: Synoptic view of computed shear instability cross-shore momentum transfer expressed in  $(m^3/s^2)$  for  $k_N = 0.0035$  m. Lower panels: Comparison of measured (left) and computed (right) momentum transfer at various cross-sections. Measurements (markers) connected by a spline. Estimated lateral mixing (left panel, dashed line) added as a reference.

fourth transect located at 27.25 m from the inflow, the results are in reasonable correspondence. Based on these and previously obtained results (see Chapter 5) we conclude that the numerical model is an accurate representation of the physical model and expect the results obtained from the extended numerical model to be representative for the flow conditions which would have occurred had the physical model been longer.

The alongshore development of the integrated spectral density of  $u$  and  $v$  for the extended basin is shown in Figure 6.7. This shows that an equilibrium for the alongshore shear instability velocity is indeed reached at approximately 27 metres from the inflow opening. This is not the case for the cross-shore component, which reaches an equilibrium at approximately 35 m. The expected asymptotic behaviour near the equilibrium is not present for the alongshore velocity compo-

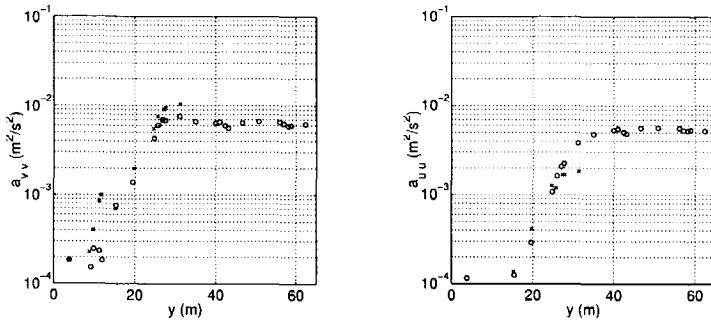


**Figure 6.7:** Alongshore development of integrated spectral density based on the alongshore (left panel) and cross-shore (right panel) shear instability velocities for the extended basin. Computed results, obtained with  $k_N = 0.0035$  m, indicated by circles vs. measurements indicated by crosses.

ment, showing a sudden levelling off at 27 m.

A synoptic view of the computed vorticity in the upstream part of the extended basin after approximately 40 minutes is shown in Figure 6.8. No significant changes occurred further downstream.

The overall view shows an oscillation increasing in intensity up to approximately  $y = 35$  m which is comparable to the length of the basin during the laboratory experiments, after which the oscillations are stable resulting in a more or less constant meandering of the longshore current.

The alongshore development of the computed mean longshore current for the present case, shown in the lower panel of Figure 6.8, shows a rapid adjustment of the mean velocity profile between the transects located at 26.95 m and 35 m from the inflow opening. After 35 metres only minor changes occur and equilibrium is established, analogous to the observed behaviour for the cross-shore velocity component of the shear instabilities. Given the limited length of the basin during the laboratory experiment, this could not be observed at the time. It is therefore expected that if the basin had been longer, the anticipated smoothing of the longshore current velocity profile would have occurred.

## 6.6 Conclusions

A detailed analysis of the cross-shore momentum flux due to the presence of finite amplitude shear instabilities in a wave-driven longshore current was made based on the measurements obtained during a laboratory experiment. It showed an

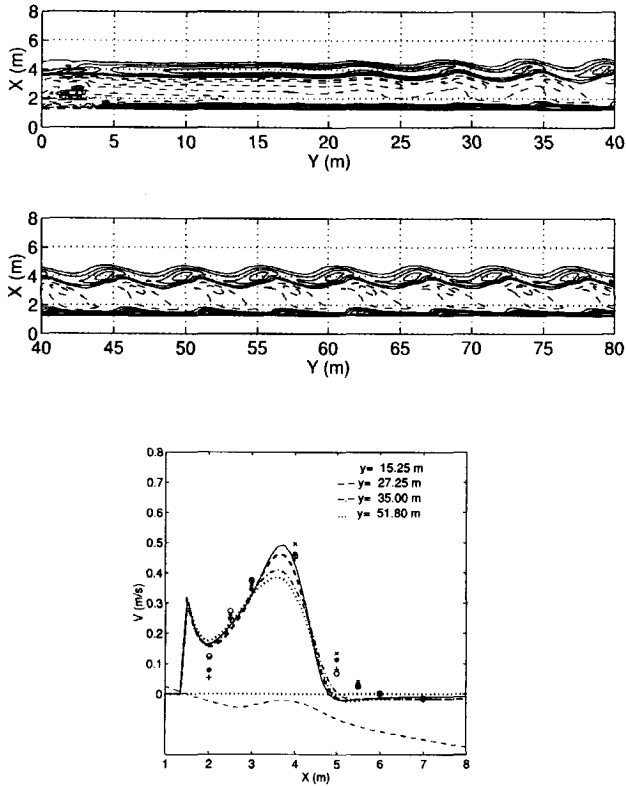


**Figure 6.8:** Snapshot of potential vorticity contours between  $y = 0$  m and  $y = 40$  m (upper panel) and between  $y = 40$  m and  $y = 80$  m (middle panel) for the extended basin. Lower panel: Mean longshore current velocity profiles obtained for  $k_N = 0.0035$  m at transects located at 15.05 m (solid), 27.25 m (dashed), 35.00 m (dash-dotted) and 51.80 m (dotted) from the inflow. Bottom profile (lower dashed line, not to scale) and measurements (markers) shown as a reference.



alongshore increasing cross-shore flux, at the downstream end of the basin becoming of comparable order as the mixing associated with breaking wave induced turbulence. However, no significant downstream changes in the mean longshore current velocity profile were detected. This can be explained by the fact that the shear instabilities take only effect near the downstream end, showing a strong increase over a short distance making inertia effects important, whereas the wave forcing is present all along the beach.

Computations with the extended numerical basin indicate that equilibrium for the shear instabilities was not yet reached during the experiment. The cross-shore component of the shear instability velocity reaches an equilibrium at approximately 35 m from the inflow opening (whereas the available length of the basin including outflow effects was 32 m), as does the mean longshore current profile. The latter exhibits the anticipated smoothing of the velocity profile.



# Chapter 7

## Discussion

### 7.1 Introduction

In the following a number of aspects are discussed related to the results presented in the previous Chapters. Starting with the measurements. Questions to be considered are: Why did the longshore current on a plane beach not show any indication of the presence of shear instabilities? In the case of a barred beach, shear instabilities did occur, but their behaviour was very coherent, i.e. not breaking up into separate eddies shedding offshore. Why is that? What is the effect of the recirculation on the alongshore development of the mean longshore current profile? What is the importance of shear instabilities in longshore current modelling and how can it be incorporated into the 1D-longshore current models? A number of these questions will be discussed, based on the results presented in the previous sections, and incorporated in the concluding remarks at the end of this Chapter.

### 7.2 Planar beach conditions

Application of the described spectral analysis procedure to the velocities obtained in the case of a non-barred beach (low water level) gave no indications of instabilities. This does not necessarily imply that shear instabilities do not occur in the case of every non-barred beach. The observed longshore current profile on a non-barred beach was very narrow and had a strong back shear, with the maximum velocity occurring at a water depth too small for the EMF to be deployed. The importance of the distance of the maximum of the longshore current velocity to the water line,  $X_b$ , was mentioned in Chapter 1. A non-dimensional parameter controlling the stability of a longshore current is (Falqués et al., 1994):

$$\frac{\nu_{t,max}}{f_s X_b^2} \quad (7.1)$$

in which  $f_s$  is the maximum backshear of the longshore current. This shows that an increase of  $X_b$  results in a decrease of the stability parameter. The maximum eddy viscosity,  $\nu_{t,max}$  and back shear,  $f_s$ , can be expected to be of the same order in case of barred and nonbarred beaches. However,  $X_b$  is typically smaller in case of a nonbarred beach rendering the longshore current more stable. An additional stability analysis of test SC219, using the measured longshore current velocity profile and non-barred bottom profile as input, showed that the longshore current is indeed expected to be stable. So it could be that the range of wave heights was not adequate to generate an unstable longshore current in the case of a non-barred beach.

### 7.3 Vortex shedding

Neither in the measurements (verified from the disperion of dye) nor in the nonlinear model computations the observed shear instabilities break up into separate eddies. This is in contrast with most of the results obtained from extensive numerical modelling by Allen et al., [1996], Özkan and Kirby, [1995], Özkan-Haller and Kirby, [1996] and [1997], Slinn et al., [1998], where strong non-linearities were observed in the shear instabilities leading to vortices shooting offshore thereby transporting mass and momentum out of the surf zone. The shear instability evolution is strongly dependent on the damping present in the system, either due to bottom friction or eddy viscosity; the behaviour of the shear instabilities becoming less energetic for increased damping.

In the field or laboratory, the balance between friction and forcing is not arbitrary. In fact, the mean flow characteristics without the presence of shear instabilities require a specific bed roughness. The same bed roughness operates on the shear instabilities. This is unlike the computations performed by Allen et al, 1996, who adjusted the wave forcing to keep the mean longshore current profile constant for all friction factors used, whereas in reality the increased wave forcing will lead to a change in the longshore current velocity profile.

The balance between wave forcing and bottom friction is less evident during field conditions. This is due to the fact that the observed longshore current velocity profile may already be affected by the presence of shear instabilities. It is therefore not possible to balance the forcing and friction prior to the computations of the shear instabilities.

In the laboratory experiment, there is a clear case of spatial growth. Shear instabilities are infinitesimally small near the inflow opening and can therefore

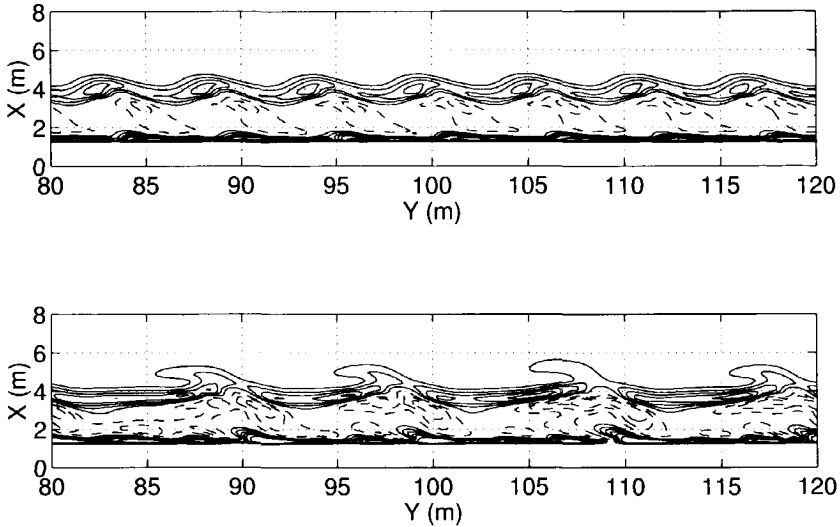


**Figure 7.1:** Contours of negative (dashed) and positive (solid) potential vorticity in the extended basin for  $k_N = 0.0035$  m (upper) and  $k_N = 0.0005$  m (lower panel)

not affect the longshore current velocity profile. Adjustments of the flow due to a mismatch between the redistribution of the pumped discharge and the wave-driven longshore current occurred over a short length scale, typically in the order of a 10 meters, which was assessed by measuring the longshore current velocity profiles during the minimisation of the recirculation in the basin. This means that the longshore current velocity profile approximately 10 m from the inflow opening, for a minimal recirculation, is governed by wave forcing, lateral mixing associated with wave breaking induced turbulence and bottom friction.

That renders the possibility to establish the balance between bottom friction, wave breaking induced lateral mixing and wave forcing, by calibrating the flow model with the measured longshore current velocity profiles 10 m downstream from the inflow opening. Given the limited length of the laboratory basin, the observed changes in the mean longshore current velocity profile were negligible, and therefore any of the measured longshore current profiles could be used. In that case the computed instabilities proved to be robust in shape, not breaking

up into separate eddies. This was the case for all bottom roughnesses used, which ranged from  $0.002 \text{ m} < k_N < 0.005 \text{ m}$ .

As a matter of interest we have computed the velocity field for reduced bottom roughness,  $k_N = 0.0005 \text{ m}$ , to examine the behaviour of the numerical model. A synoptic view of the potential vorticity approximately halfway down the extended basin is shown in Figure 7.1. It is expected, based on earlier computations of Allen et al., [1996], that the behaviour of the shear instabilities will be more energetic. This is confirmed by the comparison with the results obtained earlier, see upper panel of Figure 7.1. Also the change in wave length, which is now in the order of 10 m instead of the earlier observed 6 m is in correspondence with their results for lower damping conditions. The separation or shedding of vortices from the surfzone was still not observed for the bottom roughness used. It is believed that this behaviour will occur as a result of a further reduction of  $k_N$  in the computations. This is not pursued any further here.

The mean longshore current velocity profiles at various transects for both cases are shown in Figure 7.2. For the reduced bottom roughness there is an increased circulation in the basin, resulting in higher flow velocities outside the surfzone, due to the mismatch between the pumped discharge at the inflow and the mean flow in the interior. A comparison between the longshore current profiles computed at  $y = 15.25 \text{ m}$  and  $y = 27.25 \text{ m}$  for both roughness values shows that in the case of a lower roughness the changes in the velocity profile are significantly larger, with a decrease in the maximum flow velocity and a broadening of the longshore flow. For the higher roughness the observed changes are small. In both cases additional mixing occurs further downstream. For the lower roughness case this results in a even smoother longshore current profile with changes in the flow velocity occurring predominantly at the backshear. For the higher roughness we can now observe a decrease in the maximum flow velocity accompanied by only small changes in the back shear.

## 7.4 Shear instabilities and longshore current modelling

The potential for cross-shore mixing of momentum induced by the shear instabilities has been demonstrated in the previous section: in that particular case the longshore current maximum is reduced in amplitude and the longshore current profile becomes smoother. The changes in the longshore current are significant and therefore important to any related quantities such as the sediment transport.

However, to obtain the correct longshore current velocity profile an extensive computation is required using a non-linear numerical model. More general, the

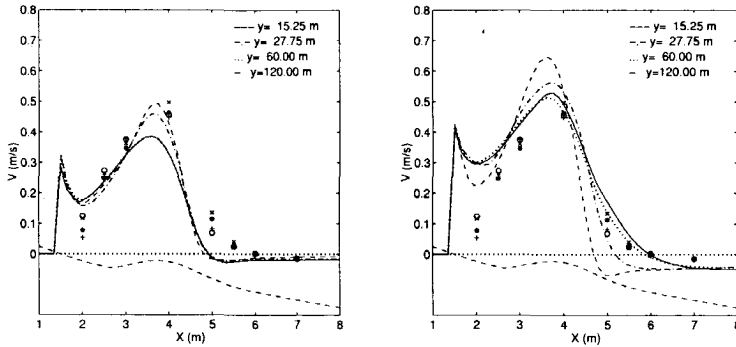


**Figure 7.2:** Alongshore development of computed mean longshore current velocity profiles in the extended basin for  $k_N = 0.0035$  m (left) and  $k_N = 0.0005$  m (right panel). Measurements indicated by the markers given as a reference.

changes in the longshore current profile are a function of the cross-shore structure of the shear instabilities and the corresponding phase coupling between the  $u$  and  $v$  components. It is therefore also possible to compute the structure and phase coupling of the shear instability components with a linear stability model to examine the effect on the longshore current velocity profile, a method introduced by Church et al. [1992]. Such a computation is less extensive and given the good correspondence between linear predictions and measurements it is expected that the cross-shore momentum transfer thus obtained will be representative of the finite amplitude conditions. One of the remaining problems is the amplitude of the individual components, which cannot be obtained from the linear stability analysis (i.e. only the initial growth rate is known). Church et al. [1992] used the measured shear instability intensity to calibrate the shear instability velocity components and thereby the associated mixing. Their cross-shore structure was also based on the measured longshore current profile.

Here we adopt their suggestion to apply an iterative procedure to obtain the required magnitude of the shear instability cross-shore momentum transfer without prior knowledge of the measurements. The procedure is demonstrated with a simplified testcase. Starting with the wave-averaged alongshore momentum balance for an alongshore uniform coast, the longshore current profile is computed with a linear bottom friction formulation and the appropriate boundary conditions corresponding to test SA243. This profile together with the total water depth and friction is used as input for a linear stability model using damping due to bottom friction only. In the case the longshore current is unstable an

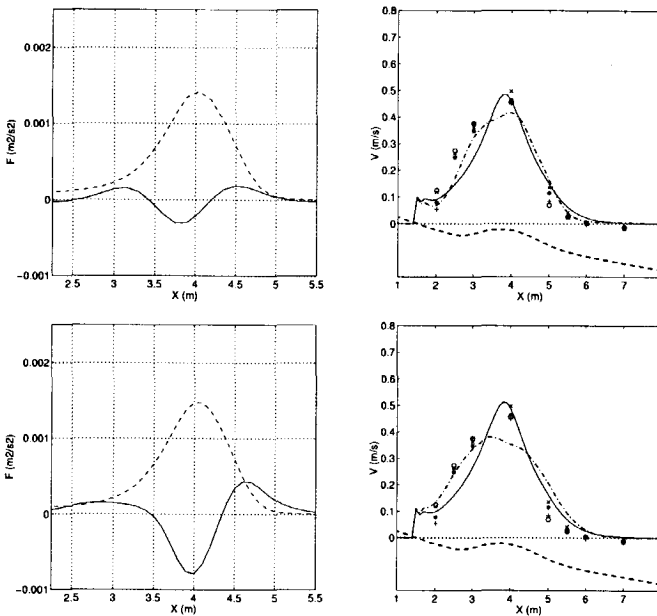


**Figure 7.3:** Upper left panel: Forcing of shear instabilities estimated from linear stability analysis (solid line) and wave forcing (dashed line). Upper right panel Corresponding longshore current profile with (dashed) and without (solid) shear instability momentum transfer. Lower panels: Similar results obtained for the case without damping. Measurements indicated by the markers given as a reference.

instability curve is obtained.

Next the cross-shore momentum transfer based on the  $uv$ -covariance of the FGM corresponding to this instability curve is computed. Multiplying the cross-shore momentum transfer by a small factor the initial mixing is obtained and added to the alongshore momentum balance. The newly obtained longshore current is again used as input for the linear stability analysis. If the maximum growth rate is reduced, the initial mixing is increased. Otherwise the newly obtained mixing, based on the adjusted longshore current profile, is added to the initial mixing. This procedure is followed until the resulting longshore current velocity profile is stable or a minimum positive growth rate is obtained.

It is clear that the resulting profile is a function of the initial maximum growth rate and thereby the damping used in the linear stability analysis. Using



this approach a correct prediction of the initial growth rate is important. This is shown in Figure 7.3, where two cases are considered: either using a friction factor in the linear stability analysis to obtain a growth rate similar to the measurements obtained for test SA243 or performing a stability analysis without taking into account any frictional effects. The results for the first case are shown in the upper panels of Figure 7.3, with a forcing which is in good qualitative and quantitative agreement with both measurements and non-linear computational results (see Figure 6.6 Chapter 6). The resulting velocity profile shows a similar behaviour as the earlier observed longshore current profile under equilibrium conditions ((see Figure 6.8 Chapter 6). Small differences do occur given the differences in modelling of lateral mixing and bottom friction. Neglecting damping effects in the linear stability analysis results in significantly higher growth rates (see also Chapter 5) and therefore an increased contribution of the shear instability momentum transfer (see lower left panel of Figure 7.3) leading to a smoother longshore current velocity profile (see lower right panel of Figure 7.3) more in line with the non-linear modelling with a low friction factor (see right panel of Figure 7.1).

Based on this it seems that the procedure is viable. Its validity should be established using a more extensive set of conditions under which shear instabilities occur given the fact that the approach is based on linear modelling whereas the shear instabilities can be highly non-linear in behaviour.

## Acknowledgements

The final writing. Going by my own experience I guess that the acknowledgements are the best-read part of any thesis, so I tried to give it proper consideration. I am sure I left people out, so in advance I thank you all who contributed to this thesis. When I started out in 1994 I had a dual development in mind for myself. I intended to improve my musical abilities on the guitar (my vocal qualities are beyond saving) along with the development of my thesis work. I must admit that I failed miserably in the musical department, but alas such is life. As for the thesis you can be the judge.

When I joined WL|Delft Hydraulics in 1992 I expressed my wish to be able to do a thesis as part of my work. It took until 1994, with thanks to Uday Putrevu, that I got the opportunity to work as a post-doc at the Burgers Foundation to investigate shear instabilities under laboratory conditions. The laboratory experiments themselves were to be performed in the Vinje-basin in de Voorst. I could not have done those experiments without the staff of WL|Delft Hydraulics. I would like to express special thanks to Pieter Pasterkamp and Piet Rorije who know how to perform an experiment and are fun to work with at the same time. Paul Visser saved me from going in circles trying to minimise the circulation in the basin by given valuable comments on the experimental set-up. Albert Falques helped in sorting out which conditions would be most promising in showing the anticipated shear instability behaviour. The measurements to monitor the generation and growth of shear instabilities benefitted from input by David Huntley who helped me with the instrument deployment. The next step was to prove that what we were measuring was actually the same thing as we were supposed to be examining, i.e. shear instabilities. To that end an analysis method based on Maximum Entropy was developed. I can still recall the moment the method actually worked after many a day of endless frustration. Without the help of Cees de Valk on the MEM I would probably have gone mad. In relating the spatial growth rate to the temporal growth rate Nick Dodd provided us with research results prior to publication on Gaster's relations. An essential add-on to our paper on longshore current instabilities.

After the first year Marcel Stive introduced me to Ed Thornton and Tom Lippmann during the last day of the Coastal Dynamics conference in Barcelona. Knowing Marcel now, I could have anticipated the conversation that followed, but at that time I was baffled by their question when I planned to come for an extended visit and what arrangements had to be made for my visum. We, Stella joined me after two months, enjoyed the seven month visit thoroughly. In that respect I would like to thank Marcel, Ed and Jurjen for making it possible, thank my colleagues at the NPS and more specifically the triple Tom's (Smottloch, Herbers and Lippmann), Rob Wyland, Antonio Faria and Mary Bristow for their

support at work and hospitality during our visit. The presence of Diane Foster, when visiting Tom, always lead to a significant increase in activity both at work and elsewhere, she even got Stella to work out on steps, all of which was great fun. Paul Frederickson took me along late at night trying to discover the night-life in Monterey. During a visit to Oregon State University, to present our work on the effect of alongshore pressure gradients on the longshore current, Nathaniel Plant provided me with video-observations of the beach during the DELILAH experiment from Rob Holman's data base for which I thank them. In addition to that I have been depriving Nathaniel, Sheila and Katherine (and now also young Carl) of the cold beer in their fridge, the BBQ'ed salmon and their living room space whenever possible. As for Mike Lippmann, we expect to see you in the y2k!

After my return to the Netherlands I turned my attention to the modelling of shear instabilities. I would like to thank Albert Falqués again for providing me with the results obtained with the linear stability analysis. The dedicated non-linear model has been developed primarily by Henri Petit and Willie ter Horst with input from Dano Roelvink and myself. I think we spent most of our time tracing some truly evasive errors which reminds me now of Heizenbergs uncertainty principle. Willie fixed it anyway. The use of this and various models of WL|Delft Hydraulics during my research is very much appreciated.

During all this time I had constant support from Jurjen Battjes who guided me during the laboratory experiments, allowed me to venture out to the USA and urged me to finish this thesis in time (which I failed to do). I would like to thank Dano Roelvink whom I have been working with for the past seven years and who has taught me a lot. The same goes for David Hurdle (that would be five years working together) whos friendship is unique. I thank my alter ego and friend Ap van Dongeren who has been my room mate at the University during the writing of my thesis. We are able to generate considerable confusion where ever we go. Let's keep it like that! My colleagues at the university and WL are acknowledged with specific support obtained from our pc-guru Andre Brouwer. My other room mate and friend at WL, Judith Bosboom, is probably wondering what I look like these days. We'll meet again Judith.

I thank my friends and family who kept me company during this period of my life. I am truly grateful for all of them being around. Special gratitude to Stella who has joined me where ever I go, making life more fun. With the birth of Femke this has only increased (though our night rest suffered a considerable blow).

## References

- Allen, J.S., P.A. Newberger and R.A. Holman, 1996: Nonlinear shear instabilities of alongshore currents on plane beaches. *J.Fluid Mech.*, vol 310, pp. 181-213.
- Allender, J.H. and J.D. Ditmars, 1981: Field measurements of longshore currents on a barred beach. *Coastal Eng.*, 5, pp 295-309.
- Battjes, J.A., 1974: Surf similarity. *Proc. of the 14th Int. Conf. Coastal Eng.*, pp. 466-479.
- Battjes, J.A., 1975: Modelling of turbulence in the surfzone. *Proc. Symp. Model. Techniques*, San Francisco. pp. 1050-1061.
- Battjes, J.A. and J.P.F.M. Janssen, 1978: Energy loss and set-up due to breaking in random waves. *Proc. 16th Coastal Eng. Conf.*, Hamburg. pp. 569-587.
- Battjes, J.A. and M.J.F. Stive, 1985: Calibration and verification of a dissipation model for random breaking waves. *J. Geophys. Res.*, 90, pp. 9159-9167.
- Birkemeier, W.A., 1991: DELILAH nearshore processes experiment: Data summary, miscellaneous reports, Coastal Eng. Res. Cent., Field Res. Facil., U. S. Army Eng. Waterw. Exp. Sta., Vicksburg, Miss..
- Bijker, E.W., 1967: Some considerations about scales for coastal models with movable bed. Dissertation, Delft University of Technology, Delft, The Netherlands.
- Bosboom, J., S.G.J. Aarninkhof, A.J.H.M. Reniers, J.A. Roelvink and D.J.R. Walstra, 1997: UNIBEST-TC 2.0: Overview of model formulations. WL—Delft Hydraulics report H2305.42.
- Bowen, A.J., 1969: The generation of longshore currents on a plane beach. *Journal of Marine Res.*, 27, pp. 206-215.
- Bowen A.J. and R.A. Holman, 1989: Shear instabilities of the mean longshore current, 1.Theory. *J. Geophys. Res.*, 94, pp. 18023-18030.
- Brøker I., 1995: Coastal facility, *Proc. of Coastal Dynamics '95*, ASCE, Barcelona.
- Burg J.P., 1967. Maximum-entropy spectral analysis. 37th Annual International SEG meeting, October 31, Oklahoma City.
- Burg J.P., 1968. A new analysis technique for time series data. NATO advanced study institute on signal processing with emphasis on underwater acoustics, Enschede, The Netherlands.
- Church C.C., E.B. Thornton and J. Oltman-Shay, 1992: Mixing by shear instabilities of the longshore current. *Proc. 23rd Int. Conf. Coastal Eng.*, Venice, pp 2,999:3,011.
- Church C.C. and E.B. Thornton, 1993: Effects of breaking wave induced turbulence within a longshore current model. *Coastal Eng.*, 20, pp 1-28.
- Deigaard, R. and J. Fredsoe, 1989: Shear stress distribution in dissipative water waves. *Coastal Eng.*, 13. pp. 357-387.

- Deigaard, R., 1993: A note on the three dimensional shear stress distribution in a surf zone. *Coastal Eng.*, 20, pp. 157-171.
- Deigaard, R., E.D. Christensen, J.S. Damgaard and J. Fredsoe, 1994: Numerical simulation of finite amplitude shear waves and sediment transport. *Proc. 24th Int. Conf. Coastal Eng.*, Kobe, pp. 1919-1933.
- Dennis J.E. and R.B. Schnabel, 1983. *Numerical methods for unconstrained optimization and nonlinear equations*. Prentice-Hall, New Jersey.
- Dodd, N. and E.B. Thornton, 1990: Growth and energetics of shear waves in the nearshore. *J.Geophys.Res.*, 95, C9, pp 16,075:16,083.
- Dodd, N., J.Oltman-Shay and E.B.Thornton, 1992. Shear instabilities in the longshore current: a comparison of observations and theory. *J. Phys. Oceanog.* 22, 1, 62-82.
- Dodd, N. and E.B. Thornton, 1992. Longshore current instabilities: growth to finite amplitude. *Proc. 23rd Int. Conf. Coastal Eng.*, Venice, 2655-2668.
- Dodd, N. and A. Falqués, 1996: A note on spatial modes in longshore current shear instabilities. Submitted to *J.Geophys.Res.*
- Duncan, J.H., 1981: An experimental investigation of breaking waves produced by a towed hydrofoil. *Proc. Roy. Soc. Lond.*, A 377, pp. 331-348.
- Dyhr-Nielsen, M. and T. Sørensen, 1970: Some sand transport phenomena on coasts with bars. *Proc. 12th Int. Conf. Coastal Eng.*, Washington, pp 855-865.
- Falqués A. and I. Iranzo, 1994. Numerical simulation of vorticity waves in the near-shore, *J.Geophys.Res.*, 99, C1, 825-841.
- Falqués A. I. Iranzo and M. Caballería, 1994. Shear instability of longshore currents: effect of dissipation and non-linearity. *Proc. 24th Int. Conf. Coastal Eng.*, Kobe, ch. 143, 1983-1997.
- Galvin, C.J. and P.S. Eagleson, 1965: Experimental study of longshore currents on a plane beach. *US Army Coastal Eng. Res. Cent.*, Tech. Mem. 10, 80 pp.
- Gaster, M., 1962: A note on the relation between temporally-increasing and spatially-increasing disturbances in hydrodynamic stability. *J. Fluid Mech.*, 14, 222-224.
- Huntley, D.A., R.T. Guza and E.B. Thornton, 1984: Field observations of surf beat. 1. Progressive edge waves. *J. Geophys. Res.*, 86, C7, pp. 6451-6466.
- Lippmann, T.C., A.H. Brookins and E.B. Thornton, 1994. Wave height transformation using wave roller theory, submitted to *Coastal Eng.*
- Lippmann, T.C. and E.B. Thornton, 1996: The spatial distribution of wave rollers and turbulent kinetic energy on a barred beach. Submitted to *J. Geophys. Res.*
- Lippmann, T.C., E.B. Thornton and A.J.H.M. Reniers, 1995: Wave stress and longshore current on a barred profile. *Proc. of Coastal Dynamics '95*, ASCE, pp. 401-412.

- Longuet-Higgins, M.S., 1970: Longshore currents generated by obliquely incident sea waves. *J. Geophys. Res.*, 75, pp. 6778-6801.
- Longuet-Higgins, M.S., 1973: The mechanics of the surf zone. *Proc. Int. Conf. Theor. Appl. Mech.*, 13th, Moscow, pp. 212-228.
- Longuet-Higgins, M.S. and R.W. Stewart, 1964: Radiation stresses in water waves: a physical discussion, with applications. *Deep-sea Res.* 11, pp. 529-562.
- Mizuguchi, M. and K. Horikawa, 1978: Experimental study on longshore current velocity distribution. *Bull. Fac. Sci. Eng., Chuo Univ., Tokyo, Japan*, 21: 123-150.
- Nadaoka, K. and H. Yagi, 1993: A turbulent-flow modeling to simulate horizontal large eddies in shallow water. *Advances in Hydro-Science and Eng.*, 1[B], pp. 356-365.
- Nairn, R.B., J.A. Roelvink and H.N. Southgate, 1990: Transition zone width and implications for modelling surfzone hydrodynamics. *Proc. 22nd Int. Conf. Coastal Eng.*, New York, pp. 68-81.
- Oltman-Shay J., P.A. Howd and W.A. Birkemeier, 1989. Shear instabilities of the mean longshore current, 2. Field observations, *J. Geophys. Res.*, 94, C12, 18031-18042.
- Özkan and J.T. Kirby, 1995: Finite amplitude shear wave instabilities. *Proc. Coastal Dynamics '95*, ASCE, Gdansk, pp. 465-476.
- Özkan-Haller, H.T. and J.T. Kirby, 1996: Numerical study of low frequency surf zone motions. *Proc. 25th Int. Conf. Coastal Eng.*, Orlando, pp. 1361-1374.
- Özkan-Haller, H.T. and J.T. Kirby, 1997: Shear Instabilities of longshore currents: Flow characteristics and momentum mixing during Superduck. *Proc. Coastal Dynamics '97*, ASCE, Plymouth, pp. 466-475.
- Petit, H., 1997: Wave-averaged energy transport, transformation to roller energy and generation of wave forces. *Delft Hydraulics report in preparation*, M3007.30.
- Putrevu, U and I.A. Svendsen, 1992: Shear instability of longshore currents: A numerical study, *J. Geophys. Res.*, 97, C5, 7283-7303
- Putrevu, U., J. Oltman-Shay and I.A. Svendsen, 1995: Effect of alongshore nonuniformities on longshore current predictions, *J. Geophys. Res.*, 100, C8, 16119-16130.
- Reniers A.J.H.M., J.A. Battjes, A. Falqués and D.A. Huntley, 1994: Shear-wave laboratory experiment. *Proc. Int. Symp.: waves- physical and numerical modelling*, Vol. 1, 356-365.
- Reniers A.J.H.M., E.B. Thornton and T.C. Lippmann, 1995: Longshore currents over barred beaches. *Proc. of the Coastal Dynamics '95*, ASCE, Gdansk, pp. 413-424.
- Reniers, A.J.H.M. and J.A. Battjes, 1996: Cross-shore momentum flux due to shear instabilities. *Proc. 25th Int. Conf. Coastal Eng.*, Orlando, pp. 175-185.
- Reniers, A.J.H.M., J.A. Battjes, 1997: A laboratory study of longshore currents over barred and non-barred beaches. *J. of Coastal Eng.*, vol 30, pp. 1-22.

- Reniers, A.J.H.M, J.A. Battjes, 1997: Non-linear modelling of shear instabilities. CD'97 Proceedings, Plymouth, pp. 436-445..
- Reniers, A.J.H.M, J.A. Battjes, A. Falques and D.A. Huntley, 1997: A laboratory study on the shear instability of longshore currents. *J. Geophys. Res.*, 102, C4, pp. 8597-8609.
- Roelvink, J.A., 1993: Dissipation in random wave groups incident on a beach. *J. of Coastal Eng.*, vol 19, pp. 127-150.
- Roelvink, J.A. and M.J.F. Stive, 1989: Bar generating cross-shore flow mechanisms on a beach. *J.Geophys. Res.*, 94, C4, 4485-4800.
- Slinn D.N., J.S. Allen, P.A. Newberger and R.A. Holman, 1998: Nonlinear shear instabilities of alongshore currents over barred beaches. *J.Geophys. Res.*, 103, C9, pp. 18,357-18,379.
- Smith, J.M., M. Larson and N.C. Kraus, 1993: Longshore current on a barred beach: Field measurements and calculation. *J.Geophys. Res.*, 98, C12, pp. 22,717-22,731.
- Soulsby, R.L., A.G Davies, J. Fredsoe, D.A. Huntley, I.G. Jonsson, D. Myrhaug, R.R. Simons, A. Temperville and T. Zitman: 1993: bed shear stresses due to combined waves and currents. G8M (Mast), abstracts in depth, Grenoble, 2.1.
- Stive M.J.F., 1980: Velocity and pressure field of spilling breakers. *Proc. 17th Int. Conf. Coastal Eng.*, Sydney, pp. 547-566.
- Stive M.J.F. and H.G. Wind, 1982: A study of radiation stress and set-up in the nearshore region. *Coastal. Eng.*, 6, pp. 1-25.
- Stive M.J.F. and H.J. de Vriend, 1994: Shear stresses and mean flow in shoaling and breaking waves. *Proc. 24th Int. Conf. Coastal Eng.*, Kobe, pp. 594-608.
- Stoker, J.J, 1957: *Water waves*, Interscience Publishers, New York.
- Svendsen, I.A., 1984: Wave heights and set-up in a surfzone. *Coastal Eng.*, 8, pp. 303-329.
- Svendsen, I.A. and U. Putrevu, 1994: Nearshore mixing and dispersion. *Proc. R. Soc. Lond. A* 445, pp 561-576.
- Thornton, E.B., 1970: Variation of longshore currents across the surf zone. *Proc. 12th Int. Conf. Coastal Eng.*, Washington, pp. 291-308.
- Thornton, E.B., 1983: Transformation of wave height distribution. *J. Geophysical Res.*, 88, pp. 5925-5938.
- Thornton, E.B. and R.T. Guza, 1986: Surfzone longshore currents and random waves: Field data and models. *J. Phys. Oceanogr.*, 16, pp. 1165-1178.
- Thornton, E.B., R.T. Humiston and W. Birkemeier, 1996: Bar/trough generation on a natural beach, *J. Geophysical Res.*, 101, C5, pp. 12,093-12,110.
- Visser, P.J.,1980:Longshore current flows in wave basin. *Proc. 17th Int. Conf. Coastal Eng.*, Sydney, pp. 462-479.
- Visser, P.J.,1984:Uniform longshore current measurements and calculations. *Proc. 19th Int. Conf. Coastal Eng.*, Houston, pp. 2192-2207.

Visser, P.J., 1991: Laboratory measurements of uniform longshore currents. *Coastal Eng.*, 15, pp. 563-593.

Whitford, D.J., 1988: Wind and wave forcing of longshore currents across a barred beach, Ph.D. Thesis, Naval Postgraduate School, Monterey, CA, pp. 205.

Whitford D.J. and E.B. Thornton, 1994: Longshore currents over a barred beach during SUPERDUCK. Submitted to *Coastal Eng.*



# Appendix A

In the following we demonstrate that for the tests under consideration, the temporal stability analysis can be used to obtain a reliable prediction of the dispersion relation and corresponding growth rates. For a complete analysis we refer to Dodd and Falqués [1996]. The maximum errors made in the predictions which arise in using temporal instead of spatial stability analysis are assessed using the relations as defined by Gaster [1962]. Provided that the wave number,  $k$ , is an analytic function of the frequency,  $\omega$ , (given by the dispersion relation) both assumed to be complex, the following relations hold (keeping  $\omega_r$  constant):

$$\omega_r(T) = \omega_r(S) \quad (7.2)$$

$$k_r(T) = k_r(S) + O(\omega_i(T)k_i(S)) \quad (7.3)$$

$$\frac{\partial \omega_r}{\partial k_r}(T) = -\frac{\omega_i(T)}{k_i(S)} + O(\omega_i(T)k_i(S)) \quad (7.4)$$

where  $T$  and  $S$  stand for temporal, respectively spatial growth only, and the subscripts  $r$  and  $i$  denote the real and the imaginary parts of the wave number,  $k$ , and frequency,  $\omega$ . Provided the growth rates are small one can neglect the higher order term,  $O(\omega_i(T)k_i(S))$ , and simple relations remain to relate the temporal and spatial analyses. Next we assess the relative importance of this term for the present set of experiments. For that matter the equations are non-dimensionalised using the observed time and spatial scales for test SA243,  $T_p = O(25)$  s and  $L_p = O(7.5)$  m respectively:

$$\omega' = \frac{\omega T_p}{2\pi} \quad (7.5)$$

$$k' = \frac{k L_p}{2\pi} \quad (7.6)$$

The spatial growth rate,  $-k_i(S)$ , can be obtained from the measurements:

$$a(y) = a_0 \exp(-2k_i(S)y) \quad (7.7)$$

where  $a$  represents the variance present between 0 Hz and 0.1 Hz and  $y$  the distance with respect to the inflow opening; the subscript 0 denotes the initial value at  $y = y_0 = 3.75m$ . The estimated spatial growth rate is then of  $O(0.1)$  rad/m. A conservative assumption is that the temporal growth rate,  $\omega_i$ , is of  $O(k_i)$ . This gives a non-dimensional error of where eqs. 7.5 and 7.6 have been used:

$$O(\omega'_i k'_i(S)) = 0.05 \quad (7.8)$$

whereas the leading term in eq. 7.2,  $k'_r(S)$  (see also Figure 3.6), is of  $O(1)$ . This means that the expected error in the predicted dispersion relation is  $O(5\%)$ . Using similar arguments for eq. 7.4 results in an error of  $O(5\%)$  in the predicted growth rate. Given the other uncertainties in the bottom friction and eddy viscosity, the approximation suggested by Gaster is considered a valid one. Therefore temporal stability analysis will be used to predict the range of unstable wave numbers:

$$k_r(T) = k_r(S) \quad (7.9)$$

The corresponding growth rate will be compared to the measurements using the group velocity:

$$\omega_i(T) = -\frac{\partial \omega_r}{\partial k_r}(T) k_i(S) \quad (7.10)$$

In the case the instabilities are non-dispersive the phase velocity can be used instead of the group velocity.

## Curriculum Vitae

Ad Reniers werd geboren op 9 mei 1964 te Schijf, een gehucht binnen de gemeente Rucphen (NB). De middelbare school werd 'doorlopen' aan de katholieke scholengemeenschap te Etten-Leur waar na zes jaar het afsluitende VWO-diploma werd behaald. Dat was in 1982. Vervolgens een opleiding tot weg-en waterbouwkundige gevolgd aan de HTS te Tilburg, met als specialisatie konstrukties, afgerond in 1986. Na een ruim jaar 'bezinning' als tankcommandant tijdens militaire dienst, 1987-1988, begonnen aan de studie civiele techniek aan de Technische Universiteit Delft in 1988. Afstudeeronderzoek naar generatie van lange golven onder korte golven groepen onder begeleiding van Prof. J.A. Battjes uitgevoerd bij het Waterloopkundig Laboratorium. Dit afstudeerwerk werd onderscheiden door het Universiteitsfonds. In 1992 deze studie met lof afgerond. Daarna werkzaam als project-ingenieur bij het Waterloopkundig Laboratorium en als toegevoegd onderzoeker aan de Technische Universiteit Delft.